Università degli Studi di Padova

Department of Information Engineering

Ph.D. Course in Information Engineering

Information and Communication Science and Technologies Curriculum

XXXVI series

Heterogeneous Rank Beamforming for Industrial Communication and Sensing

Ph.D. Supervisor
Prof. Andrea Zanella

Ph.D. Candidate
Andrea Bedin

Ph.D. Coordinator
Prof. Fabio Vandin

Year 2022-2023

Abstract

Wireless communication has become an integral part of modern industrial environments, enabling real-time data exchange between pieces of industrial equipment, as well as remote control and maintenance by connecting the machines to the operators. The use of wireless communication in industrial environments has several advantages, such as reduced costs, improved productivity, and increased flexibility. However, it also poses several challenges due to the presence of obstacles, interference, and other environmental factors that can degrade the quality of wireless communication.

With the increasing demand for higher data rates and reliable communication in such challenging environments, wireless communication technology has evolved significantly over the years. Recently, due to the diffusion of Line of Sight (LoS) oriented analog beamforming strategies, which are well suited for a certain subset of environments, the reliability of wireless systems in industrial environments has degraded, and their ability to exploit the rich multipath propagation of such environments has been severely limited. This fact is particualrly relevant for industrial environment which, as highlighted by the measurement campaign presented in this work, presents very rich multipath. On the other hand, due to the large number of antennas needed to overcome the path loss of millimeter wave (mmWave), the choice of moving towards analog beamforming is motivated by the complexity and power consumption of the devices might seem inevitable.

To overcome this issue, in this thesis we propose a novel hardware architecture that allows the trade-off between bandwidth and rank of the channel. Such architecture is slightly more complex than a classical hybrid beamforming architecture but still significantly simpler, cheaper, and low power compared to fully digital beamforming. This aims to overcome the limitations of analog beamforming in at least part of the bandwidth with a limited increase in costs. We analyze the performance of Proportional Fairness resource allocation for multiple users equipped with such an architecture, showing that in a multi-user environment, a large part of the communication can be performed exploiting digital beamforming, despite the users not operating with digital beamforming on the full band. We study the performance of Maximal Ratio Combining as a robust analog beamforming beam based on digital beamforming information. Such method is particularly useful in combination with the resource allocation scheme mentioned above, as it can reliably fill in any gap that is not allocated with digital beamforming. Moreover, it can also reliably detect and decode control signaling to avoid unwanted disconnections from the network. Finally, we propose a method to perform multipath decomposition and time and angle of arrival estimation on the received signal that can jointly exploit the high rank and high bandwidth provided by the proposed architecture. The proposed method also has significantly lower complexity compared to existing methods,

as it decomposes the 2D parameter estimation in a sequence of 1D estimations.

Contents

Abstract v

List of figures xi

List of tables xiii

List of acronyms xv

1 Introduction 1

2 Industrial communications: challenges and requirements 5
- 2.1 Communications requirements . . . 5
- 2.2 Sensing requirements . . . 8
- 2.3 Challenges . . . 9
  - 2.3.1 Beam tracking . . . 9
  - 2.3.2 Lack of diversity . . . 9
  - 2.3.3 Sensing complexity . . . 10

3 Propagation environment 11
- 3.1 Commercial port case study . . . 11
  - 3.1.1 Measurement setup . . . 11
  - 3.1.2 Angular spread . . . 15
  - 3.1.3 Spatial correlation . . . 17
  - 3.1.4 Effect of the presence of a vehicle . . . 19
  - 3.1.5 Path loss . . . 21
  - 3.1.6 Propagation model . . . 25
  - 3.1.7 Elevation spectrum . . . 30
- 3.2 Channel characteristics . . . 32

4 Beamforming architectures 35
- 4.1 Classical beamforming architectures . . . 35
- 4.2 Proposed heterogeneous rank architecture . . . 39
- 4.3 Complexity, power consumption and cost analysis . . . 41

5 System Model 45

6 Communication 53
6.1 Multi-user resource allocation for heterogeneous rank systems 54
6.1.1 Proportional Fairness Resource Allocation 54
6.1.2 Empty buffer approximation 60
6.1.3 Equal buffering probability approximation 61
6.1.4 Results 63
6.2 Robust analog beamforming 69
6.2.1 Beam Geometry 71
6.2.2 Wideband behaviour 76
6.2.3 Performance evaluation 80
6.2.4 Interference 85
6.3 Joint analog and digital beamforming operation 88

7 Sensing 91
7.1 Definitions 92
7.2 Sensing method 94
7.2.1 Time domain decomposition 94
7.2.2 Component amplification 97
7.2.3 Angle of arrival extraction 99
7.3 Results 100
7.4 Leakage issue 103

8 3GPP signaling for heterogeneous rank beamforming 105
8.1 Capabilities reporting 106
8.2 UE configuration 107
8.3 Resource allocation 108

9 Conclusion 109

A 3GPP messages structure 111

References 119

Publications 127

Acknowledgments 127

Listing of figures

3.1 Measurement environment. 12
3.2 Coordinate and angle reference. 13
3.3 Coarse measurements map. 13
3.4 Dense measurements map. 14
3.5 Angular spectrum with uniform stacking. 16
3.6 Angular spectrum with nonuniform stacking. 16
3.7 Ineffectiveness of beamforming in a port environment. 17
3.8 Spatial correlation. 18
3.9 Statistics of the vehicle effect with uniform stacking and TX1 at 63m. 19
3.10 Angle independent statistics of the vehicle effect with uniform stacking and TX1 at 63m. 20
3.11 Statistics of the vehicle effect with nonuniform stacking and TX2. 20
3.12 Angle independent statistics of the vehicle effect with nonuniform stacking and TX2. 21
3.13 Measured and simulated channel gain. 23
3.14 simulated channel gain with omnidirectional antennas. 24
3.15 Container canyon propagation model (side view). 25
3.16 Container canyon propagation model (top view). 28
3.17 propagation inside the canyon. 28
3.18 Channel gain model fit. 30
3.19 Elevation spectrum for the nonuniform configuration. 31

4.1 Classical fully connected hybrid beamforming hardware architecture. . . . 36
4.2 Classical fully digital beamforming hardware architecture. 37
4.3 Example resource grid. 38
4.4 Heterogeneous rank hardware architecture. The wideband analog beamforming and the narrowband fully-digital beamforming blocks are highlighted in yellow and blue, respectively. 39

5.1 System overview. 46
5.2 Array model. 46
5.3 Example of signal from the digital beamforming part. 50

6.1 Example resource grid in *heterogeneous mode*. 54

6.2 Example resource grid in *heterogeneous mode*, where the data does not fit entirely within the MIMO bandwidth. 55
6.3 Maximum achievable SE as a function of the number of users. 57
6.4 Allocation process. 59
6.5 P_a as a function of P_b for $|\mathcal{U}_r| = 4$ and $U = 100$. 63
6.6 Rate achieved by the user and system for $\Lambda = 500$. 64
6.7 Rate achieved by the user and system for $\Lambda = 100$. 65
6.8 Rate achieved by the user and system for $\Lambda = 50$. 65
6.9 Fraction of RBs allocated to analog beamforming and reason of the allocation for $\Lambda = 50$. 66
6.10 Fraction of unused RBs for $\Lambda = 50$. 67
6.11 Rate bounds for different values of P_b^{max}. 68
6.12 Example MRC radiation pattern. 72
6.13 Change in radiation pattern induced by an effective and an ineffective component. 74
6.14 Ineffectiveness probability and number of components utilized obtained by MRC for different ULAs (FoV $180°$). The lines represent the theoretical values, whereas the marks are given by numerical evaluation. 81
6.15 SNR obtained by MRC and the single-direction beam for different ULAs, for a FoV of $180°$ and $\sigma_{n_0} = 1$, and for different values of the number N of antennas. 82
6.16 SNR distribution for an 8 element ULA with a FoV of $180°$, $K = 20$ and $\sigma_{n_0} = 1$. 83
6.17 Channel estimate SNR impact on the beamforming gain. 84
6.18 SIR for an 8 element ULA with a FoV of $180°$, $\sigma_I = 0.1$ and $I = 5$. 86
6.19 SIR distribution for an 8 element ULA with a FoV of $120°$, $\sigma_I = 0.1$, $I = 5$ and $K = 20$. 87
6.20 Example of 5G downlink spectrogram. 88

7.1 Block diagram of the proposed method 94
7.2 Beamformed farfield pattern [dBi] without the additional lobe (blue) and with an additional lobe in different directions (black) 97
7.3 Resolution probability comparison. 101
7.4 Resolution probability of the proposed method with a fully digital MIMO architecture. 102
7.5 Accuracy of the proposed method compared to 2D-MUSIC. 103
7.6 Example of leakage. 104

Listing of tables

2.1 Requirements for selected applications 6
2.2 Telepresence requirements 7
2.3 Requirements for localization and sensing 8

3.1 height of the canyon in the nonuniform case. 12
3.2 Channel gain difference Gaussian approximation parameters for the uniform stacking and TX1 at 63m. 20
3.3 Channel gain difference Gaussian approximation parameters for the nonuniform stacking and TX2. 21
3.4 Main simulation parameters. 22
3.5 Line fit parameters (95% confidence interval). 23
3.6 Line fit parameters for omnidirectional antenna (95% confidence interval). . 24
3.7 Model fit parameters (95% confidence interval). 30

4.1 Components required by each type of architecture. 42
4.2 Comparison of the power consumption of each architecture. 42
4.3 Comparison of the cost of each architecture. 43

6.1 Example channel parameters 72
6.2 *Array parameters* for some ULAs 80
6.3 *Array parameters* for some ULAs 81

8.1 Additional parameters to DCI format1_1 108

A.1 DCI format1_1 118

Acronyms

2D-MUSIC 2D MUltiple SIgnal Classification. xii, 91, 101, 102, 103

3GPP 3rd Generation Partnership Project. 3, 105, 106, 109, 111

6G Sixth Generation. 2, 6

ADC Analog to Digital Converter. 1, 39, 40, 41, 42, 43, 48, 49, 55, 93, 109

AF Array Factor. 69

AoA Angle of Arrival. 91, 94, 97, 98

ASN.1 Abstract Syntax Notation One. 106

BS Base Station. 24, 32, 45, 54, 64, 86, 88, 89, 105

BWP BandWidth Part. 107, 108

CapEx Capital Expenditure. 7, 8, 32, 43

CDF Cumulative Distribution Function. 19, 60, 64, 79

CFR Channel Frequency Response. 47, 76, 84, 85

CIR Channel Impulse Response. 47, 48, 92

CSI Channel State Information. 2, 8, 10, 36, 37, 40, 94

DCI Downlink Control Information. 89, 108, 109

DTFT Discrete Time Fourier Transform. 48, 49

FMCW frequency modulated continuous wave. 2

FoV Field of View. xii, 80, 81, 82, 83, 86, 87

FSPL Free Space Path Loss. 23, 26, 32

HARQ Hybrid Automatic Retransmission reQuest. 9

HPBW Half Power Beam Width. 11, 21

IC Integrated Circuit. 42

IE Information Element. 106, 107, 108

JCAS Joint Communication and Sensing. 2, 10, 91

KPI Key Performance Indicator. 2, 10

LFM linear frequency modulated. 2

LNA Low Noise Amplifier. 39, 41, 42, 43, 48

LO Local Oscillator. 40, 41, 54

LoS Line of Sight. vii, 15, 32, 35, 36

LPF Low Pass Filter. 40, 50

MAC Medium Access Control. 54

MCS Modulation and Coding Scheme. 88, 89, 108

MIB Master Information Block. 88

MIMO Multiple Input Multiple Output. xii, 39, 55, 58, 88, 89, 93, 101, 102, 103, 106

mMIMO massive Multiple Input Multiple Output. 8

mmWave millimeter wave. vii, 1, 2, 32, 33, 46

MRC Maximum Ratio Combining. xii, 3, 69, 70, 72, 76, 78, 79, 81, 82, 83, 84, 85, 86, 89, 91, 96, 109

MUSIC MUltiple SIgnal Classification. 91, 94, 95

NLoS Non-Line-of-Sight. 11, 15, 23, 25, 32, 33

OFDM Orthogonal Frequency Division Multiplexing. 2, 92

OFDMA Orthogonal Frequency Division Multiplexing Access. 58

OpEx Operational Expenditure. 7, 8

PDCCH Physical Downlink Control Channel. 88

PDF Probability Density Function. 60, 79

PF Proportional Fairness. 3, 58, 59, 64, 67, 109

PMCW phase modulated continuous wave. 2

PPM pulse position modulated. 2

r.v. Random Variable. 74, 75, 77

RB Resource Block. xii, 38, 54, 55, 58, 59, 60, 61, 63, 64, 66, 67

RF Radio Frequency. 36, 39, 40, 41, 49, 54, 55, 56, 58, 70, 88, 106, 107, 108, 109

RMSE Root Mean Square Error. 29, 102, 103

RRC Radio Resource Control. 106, 107, 109

RX Receiver. 11, 12, 13, 14, 15, 16, 19, 22, 23, 24, 25, 28, 32

SE Spectral Efficiency. xii, 56, 57, 58, 63

SIB System Information Block. 88

SIMO Single Input Multiple Output. 45

SIR Signal to Interference Ratio. xii, 69, 85, 86, 87

SNR Singal-to-Noise Ratio. xii, 24, 69, 76, 78, 79, 82, 83, 84, 88, 89, 91, 95, 96, 100, 102, 103

SSB Synchronization Signal Block. 88

SVD Singular Value Decomposition. 10

ToA Time of Arrival. 91, 94, 97, 98

TX Transmitter. 11, 12, 14, 15, 16, 17, 19, 20, 22, 23, 26, 27, 30, 31

TX1 Transmitter 1. xi, xiii, 12, 13, 14, 15, 16, 19, 20, 23, 30, 31

TX2 Transmitter 2. xi, xiii, 12, 13, 14, 15, 16, 20, 21

UE User Equipment. x, 3, 12, 25, 37, 42, 45, 53, 54, 55, 56, 58, 59, 64, 65, 66, 67, 92, 105, 106, 107, 108

ULA Uniform Linear antenna Array. xii, xiii, 47, 80, 81, 82, 83, 86, 87, 92

URA Uniform Rectangular antenna Array. 72

VR Virtual Reality. 7

1 Introduction

In the era of Industry 4.0, wireless communication systems have emerged as a fundamental enabler for transforming traditional industrial environments into smart and interconnected ecosystems. The integration of wireless technologies holds the potential to revolutionize the way industrial processes are managed, monitored, and optimized. Enabling real-time data exchange between pieces of industrial equipment, as well as remote control and maintenance of the machines by the operators, the use of wireless communication in industrial environments provides several advantages, such as reduced costs, improved productivity, and increased flexibility. In an effort to meet the increasing demand for higher data rates and reliable communication in such challenging environments, wireless communication technology has evolved significantly over the years. Many studies have been carried out on different communication aspects [1, 2, 3]. Of particular interest for this work is the beamforming techniques [4, 5, 6, 7]. In recent years, there has been a focus on hybrid and analog beamforming strategies, which are oriented to sparse channels like those observed in indoor environments [8]. The channel observed in industrial environments is though different, with very complex and rich multipath [9, 10, 11]. Therefore the reliability of wireless systems in such environments is degraded, and their ability to exploit the rich multipath propagation is severely limited. On the other hand, due to the large number of antennas needed to overcome the path loss of millimeter wave (mmWave), the choice of moving towards analog or hybrid beamforming, motivated by the complexity and power consumption of the Analog to Digital Converters (ADCs) required to build digital beamforming devices, might seem inevitable. We therefore observe a

clear need for an alternative solution that is capable of effectively exploiting the highly rich multipath channel, as well as maintaining manageable costs and complexity. Furthermore, the integration of localization and sensing technologies in communication systems, commonly known as Joint Communication and Sensing (JCAS), has revolutionized industrial environments, enabling real-time monitoring, control, and optimization of processes. This synergy between communication and sensing systems has the potential to greatly enhance efficiency, safety, and productivity in industrial operations. It is also, however, limited by the hybrid and analog beamforming strategies, as those strategies make it more difficult and resource intensive to extract the full Channel State Information (CSI) for each antenna. JCAS is a widely studied topic, using both sensing specific waveforms such as frequency modulated continuous wave (FMCW) [12], phase modulated continuous wave (PMCW) [13, 14, 15], linear frequency modulated (LFM) wave [16], and pulse position modulated (PPM) wave [17], communication waveforms such as Orthogonal Frequency Division Multiplexing (OFDM) [18, 19, 20, 21, 22, 23, 24] and JCAS specific waveforms [25, 26]. These methods, though, still rely on classical hybrid, analog, and digital beamforming architectures. Together with a new architecture design that is suited to the industrial setting, we therefore need to develop a JCAS method that can exploit it for localization and sensing tasks.

Addressing these ambitious objectives, in this thesis, we propose the following:

- An overview of the foreseen requirements for Sixth Generation (6G) communications in industrial environments, including delay, reliability, and sensing Key Performance Indicators (KPIs).

- A case study of propagation in an industrial environment, specifically in a commercial port [27]. The study reveals that inside a container canyon the channel has an extremely rich multipath with a large angular spread, as well as a low spatial correlation of the angular pattern. These characteristics are all contradicting the classical sparse model used in mmWave settings, which typically uses 5 multipath components [8], in favor to a model with a large number of components.

- A novel hardware architecture that supports the trade-off between bandwidth and rank of the channel [28, 29]. Such architecture is slightly more complex than a classical hybrid beamforming architecture, but still significantly simpler, cheaper, and low power compared to fully digital beamforming. This aims to overcome the limitations of analog beamforming in at least part of the bandwidth with a limited increase in costs.

- An analysis of the performance of Proportional Fairness (PF) resource allocation for multiple users equipped with the proposed architecture [29], which shows that in a multi-user environment a large part of the communication can be performed exploiting digital beamforming, even if the users do not operate with digital beamforming on the *full* band [30].

- An analysis of Maximum Ratio Combining (MRC) as a robust analog beamforming scheme based on the digital beamforming information [31]. Such a method is particularly useful in combination with the resource allocation results mentioned above, as it can reliably fill in any gap that is not allocated with digital beamforming. Moreover, it can also reliably detect and decode control signaling to avoid unwanted disconnections from the network.

- A method to perform multipath decomposition and time and angle of arrival estimation on the received signal that can jointly exploit the high rank and high bandwidth the proposed architecture provides [32]. The proposed method also has significantly lower complexity compared to existing methods, as it decomposes the 2D or 3D parameter estimation in a sequence of 1D estimations.

- A variation of the 3rd Generation Partnership Project (3GPP) signaling that enables the support of this technology, with a small number of additional parameters in the User Equipment (UE) configuration and resource allocation messages.

2

Industrial communications: challenges and requirements

This chapter introduces the foreseen future of wireless networks that come as a motivation for the work presented in this thesis. In particular, we focus on industrial networks, which differ significantly from regular cellular networks in requirements, application, and challenges.

2.1 Communications requirements

In modern factories, reliable communication between the machinery takes an essential role in different aspects. First and foremost, safety. Being able to quickly and effectively communicate unplanned events and accidents to other parts of the factory can limit their impact and avoid injuries, deaths, and damage to other machinery. The second outcome of efficient and effective communication is productivity: if the actors working in a factory can have more up-to-date, complete, and reliable information, they are likely to perform their tasks more effectively and better coordinate operations, ultimately resulting in higher production volumes and income. Some examples of enabling technologies for enhanced safety and productivity are the following:

- Digital Twins: A virtual replica of the production plant that keeps track of the position and state of all actors in the factory. This replica can be used to plan future

actions in order to efficiently orchestrate the operations and avoid creating unsafe situations or to keep track of the usage of consumable materials to perform predictive maintenance and avoid interruption of operations.

- Cooperative robots: This technology allows synchronized and choreographed actions by multiple robots, ensuring that each robot can complete its task efficiently and effectively without interfering with the other robots' work.

- Telepresence: This technology allows human operators to interact with the factory and other operators remotely, maintaining the ability to perform most of the tasks they would do in person. It can, for example, allow specialized technicians to perform troubleshooting and maintenance in case of failures without travelling plant. This solution can drastically reduce the downtime of production lines with significant economic benefits. Moreover, it would protect the operator from exposure to the factory environment, therefore reducing risks.

	Latency	Reliability	Data Rate
Cooperative Robots	1-50 ms	10^{-9}	kbps
Digital Twins	0.1 - 100 ms	10^{-2} - 10^{-6}	1-10 Gbps

Table 2.1: Requirements for selected applications

Tab. 2.1 lists the requirements for Digital twins and cooperative robots applications. This list reports the values defined by the European 6G flagship project Hexa-X [33]. The latency requirements for these applications can reach as low as sub-millisecond values, which is highly challenging to achieve in traditional wireless networks. This tight requirement is motivated by the fact that digital twins and cooperative robots require real-time interaction and decision-making capabilities. Any communication delay can lead to safety hazards and performance degradation. In addition, the reliability requirements for these applications are also very stringent, with an error rate as low as 10^{-9}. This level of reliability is necessary to ensure that the robots operate accurately and safely without causing any harm to the environment or humans. While these requirements might seem extreme for today's factories, where robots typically move at limited speeds, they are crucial for enabling much faster operations while maintaining safety and control in future manufacturing plans. Adopting digital twins and cooperative robots can revolutionize manufacturing processes by providing accurate, real-time monitoring of machines and processes, enhancing efficiency.

Use case	Traffic type	Latency	Reliability	Data Rate
Teleoperation	Haptic UL	5 ms	10^{-1}	1-4 kbps
	Haptic DL	1-50 ms	10^{-1}	1-4 kbps
	Audio UL	10 ms	10^{-1}	5-512 kbps
	Video UL	10 ms	10^{-3}	1-100 Mbps
Immersive VR	Haptic UL	1-10 ms	10^{-3}	1-4 kbps
	Haptic DL	1-10 ms	10^{-3}	1-4 kbps
	Audio UL	20 ms	10^{-1}	5-512 kbps
	Video UL	10-20 ms	10^{-3}	1-100 Mbps

Table 2.2: Telepresence requirements

Tab. 2.2 reports a more detailed list of the requirements for telepresence and Virtual Reality (VR), as for the Hexa-X project [33]. Here we can observe the heterogeneity of the requirements for different traffic categories within the same service. For example, we can observe that the haptic interactions, which require delays as low as 1ms but are not highly demanding in terms of bitrate, must coexist with video streaming, which is, instead, very bandwidth-intensive. While this coexistence could be handled by deploying multiple networks with different capabilities, this would entail much higher Capital Expenditure (CapEx) and Operational Expenditure (OpEx) for the network operator. Therefore, it is crucial from an economic standpoint to meet all of these requirements in a single network.

Application	Position	Orientation	Update interval	Availability	Scalability
Augmented Reality	1mm	$0.5°$	$< 10ms$	99.99%	N/A
Digital Twins	1cm	$< 1°$	$0.1ms$	99.99%	N/A
Robots interaction	1cm	$1°$	$0.1ms$	99.99%	N/A
Robots localization	$<$ 1cm	$< 1°$	$0.1ms$	99.99%	$5/\text{m}^2$
Smart Cities	$<$ 1m	N/A	1s	99.99%	$10 - 100/\text{m}^3$

Table 2.3: Requirements for localization and sensing

2.2 Sensing requirements

Sensing is foreseen to be a fundamental part of future networks. Such networks are expected to become aware of the surrounding environment and the user's positions through observation of the CSI. In this context, being able to effectively, accurately, and efficiently determine the users' location is an essential capability. Similarly to what happens for communication, the requirements for localization and sensing are very application dependent. These requirements have been thoroughly studied in [34], and some of the requirements for selected applications are reported in Tab. 2.3.

Clearly, the requirements listed in the table are very challenging. We can summarize the requirements and impacts on the network with the following points:

- Accuracy, with some applications requiring sub-millimeter localization and sub-degree orientation error. While the current technology is coming closer to these requirements thanks to the exploitation of the massive bandwidth available at mmWave frequencies and the huge arrays provided by massive Multiple Input Multiple Output (mMIMO), such stringent requirements are still not practically achievable.

- Fast update rate, that with current systems would cause large overheads and computational complexity, severely harming the communication capabilities of the network and involving large CapEx and OpEx to purchase and maintain the computational infrastructure.

- Density, which also impacts the amount of computation needed to keep track of all assets, as well as requiring the capability of discerning multiple close objects.

2.3 Challenges

2.3.1 Beam tracking

As discussed in Sec. 2.1, modern industrial communications have stringent delay and reliability requirements. These make relying on retransmission processes such as Hybrid Automatic Retransmission reQuest (HARQ) not a viable solution, as the feedback and retransmission process might last a significant portion of the delay budget, thus making the packet unlikely to be delivered in time. For this reason, a successful first attempt at delivering the packet is critical. When using an analog beamforming system with classical directional beams, a possible cause of failure for the first transmission attempt is the misalignment of the beam itself. Such beams, in fact, typically provide a very good gain but also a high spatial selectivity, meaning they collect energy very efficiently from a single multipath component but have a large attenuation on all other components. For this reason, if some problem arises with such component (e.g., a blockage), the system can fail to timely deliver the required information. This problem can be mitigated by performing beam training and refinement more often, which, however, comes with large overhead and delay cost. To illustrate this issue, let us consider a simple example: assume the system is required to transmit a time-constrained packet that must be delivered within 1ms with an acceptable failure probability of 10^{-5}. The packet can be transmitted in 0.2ms using analog beamforming with a beam that was determined some time ago. Given the aging of the beamforming information, here is a failure probability of, say, 10^{-4}. In this case, the system is faced with two options

- Transmit the packet directly. In this case, the transmission attempt will happen timely, but the fhigher ailure probability is lower than the target
- Perform a beam training, which could take, e.g., 1ms, and then transmit the packet. In this case, the delivery will happen after the deadline, but with much higher reliability

In both cases the requirements will not be satisfied. This exemplifies how the classical beamforming and training techniques pose a fundamental limit to the delay-reliability tradeoff.

2.3.2 Lack of diversity

When using a directional beam, the system limits the scope of the received signal to a single multipath component. This approach can help reduce interference and improve signal quality, but it also has some drawbacks. One of the drawbacks is that the frequency diversity is

reduced, so as the robustness to shadow-fading. If the channel gain is constant through the whole system bandwidth, nothing can be done to recover if that gain is insufficient for a succesfull transmission. With a large frequency diversity instead, the system relies on multiple realizations of the channel gain , namely one for each coherence interval within the system bandwidth. It is, therefore, improbable that all of the coherence bandwidths will have a low gain, making the system more robust.

2.3.3 Sensing complexity

JCAS algorithms are known to be computationally complex, as most of them involve performing a Singular Value Decomposition (SVD) of the CSI matrix and exploring a search space of possible ranges and angles. The high complexity of JCAS algorithms poses significant challenges for their implementation, as they require considerable computational resources, memory, and power consumption. For this reason, the complexity of these algorithms makes it difficult to achieve some of the required KPIs listed in Sec. 2.2, namely latency and reliability, especially in resource-constrained environments. This problem is exacerbated by the tight accuracy requirements, which makes it necessary to acquire and process huge amounts of data and to explore a very finely quantized search space of possible ranges and angles. Therefore, there is a need for efficient and scalable JCAS algorithms that can handle large amounts of data and optimize communication parameters to meet specific performance requirements while reducing complexity and resource requirements.

3

Propagation environment

This chapter discusses the unique propagation observed in industrial environments. In particular, to exemplify such characteristics, in Sec. 3.1 we analyze in detail the results of a measurement campaign carried out in a commercial port environment. We analyze many channel characteristics for such measurements, including angular spread, spatial correlation, and path loss. The results, which show a surprisingly low path loss in Non-Line-of-Sight (NLoS) and a very rich multipath with a large angular spread, are then summarized in Sec. 3.2, where we also discuss their impact on communication systems.

3.1 Commercial port case study

3.1.1 Measurement setup

This section describes a measurement campaign carried out in a commercial port environment, specifically inside a container canyon. The measurements were conducted with the equipment described in [35]. In particular, we used a narrowband Transmitter (TX) operating at 28GHz with an output power of 22dBm and an omnidirectional antenna, whereas the Receiver (RX) is equipped with a 10° Half Power Beam Width (HPBW) horn antenna. The RX antenna is rotated in the azimuthal plane at a speed of 120rpm, and at each measurement point, we collected 10s of power measurements, corresponding to 20 full rotations of the antenna. The measurement environment, depicted in Fig. 3.1, was purposely built to resemble a commercial port and consists of a container canyon that is 36m long and has an internal

Section	1	2	3	4	5	6
Row 1	10m	7.5m	5m	5m	7.5m	5m
Row 2	5m	5m	5m	7.5m	7.5m	7.5m

Table 3.1: height of the canyon in the nonuniform case.

width of 8m. The height of the container canyon has been changed during the campaign between two different configurations. In the first configuration (Fig. 3.1a), hereafter referred to as the *uniform configuration*, the height of the canyon was of 3 containers (roughly 7.5m) for almost all the length of the canyon, except for the last 6m where there were only 2 containers (5m). The second configuration (Fig. 3.1b), referred to as the *nonuniform configuration*, has a varying height. The height of each section of the canyon is listed in Tab. 3.1. In order to define the positions of the TXs and RXs, we define as a reference point one of the corners of the canyon (depicted in blue in Fig. 3.1). We denote the direction parallel to the canyon as the "X" direction and the one orthogonal to the canyon as the "Y" direction, as depicted in Fig. 3.2. All the distances are measured from the reference corner when not otherwise specified. We used two different TX positions: Transmitter 1 (TX1) position, depicted in green, was placed at 18.8m from the reference corner in the X direction, and was mounted on a rail crane that could move from 63m to 113m in the Y direction. The height of TX1 from the ground was 23m. Transmitter 2 (TX2) was placed on a pole that is at 18.85m in the X direction and 60.5m in the Y direction. The height of TX2 was 22m from the ground.

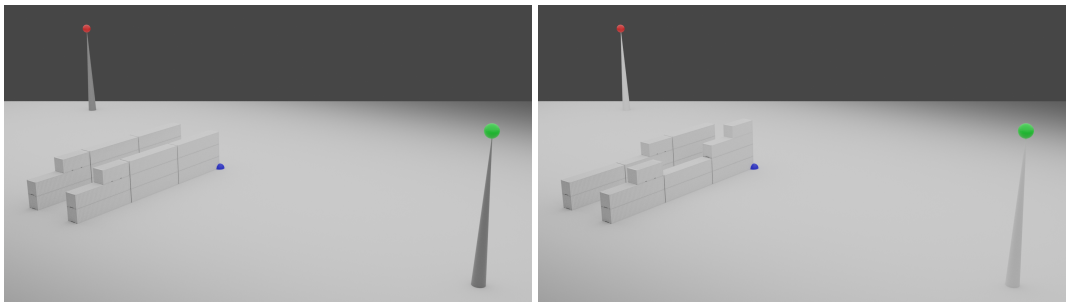

(a) Uniform stacking.

(b) Nonuniform stacking.

Figure 3.1: Measurement environment.

The RX, representing the UE, was placed in several positions based on predefined maps. Throughout the whole campaign, the reference direction corresponding to the 0° angle has been the one depicted in Fig. 3.2, where the big arrow represents the 0° direction and the

small arrow represents the positive angle direction.

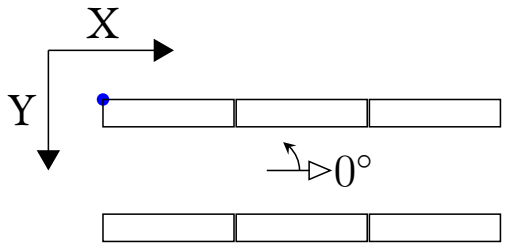

Figure 3.2: Coordinate and angle reference.

The first set of measurements is a coarse spatial sampling, and the measurement points for this experiment are depicted in Fig. 3.3 as black circles. In both the uniform and nonuniform stacking case, the measurements are on 4 lines at a distance of 3.5, 5.5, 7, 5, and 9.5 meters from the reference point in the Y direction and start at 1m in the X direction. In the uniform case, the spacing between the measurements in the X direction is 4 meters, whereas in the nonuniform case, it is 2 meters.
For the uniform case, the measurement has been repeated for different positions of TX1, ranging from 63.5m to 113.5m in steps of 10m, and from TX2(which has a fixed position). For the nonuniform case, the crane was moved in steps of 20m due to the higher number of RX points.

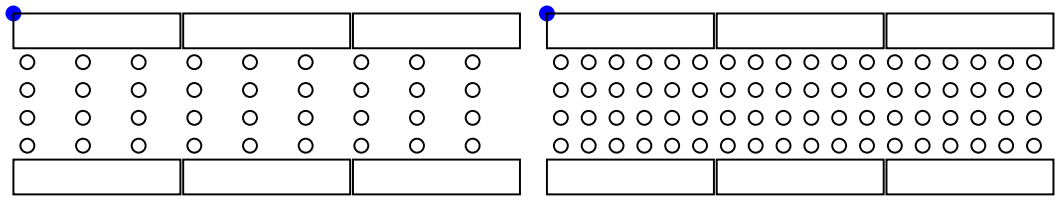

(a) Uniform stacking. **(b)** Nonuniform stacking.

Figure 3.3: Coarse measurements map.

A second set of measurements was conducted on a denser grid, depicted in Fig. 3.4. This measurement has two goals:

1. Studying the spatial correlation of the channel gain.

2. Determining the effect of the presence of a vehicle in the canyon.

The measurement points are on the same lines as the coarse measurement in the Y direction, whereas in the X direction, the measurement points start at 12.5m and end at 15.3m with a spacing of 20cm. Moreover, when the vehicle is absent, from 13.5m to 14.9m the spacing is decreased to 10cm to obtain a finer sampling of the spatial correlation. These measurements have been performed for TX2 with nonuniform stacking and for TX1 at 63m for uniform stacking. Other TX positions were planned for this measurement, but due to weather and time constraints, executing them was impossible. Overall, we collected a total of over 1200 measurements.

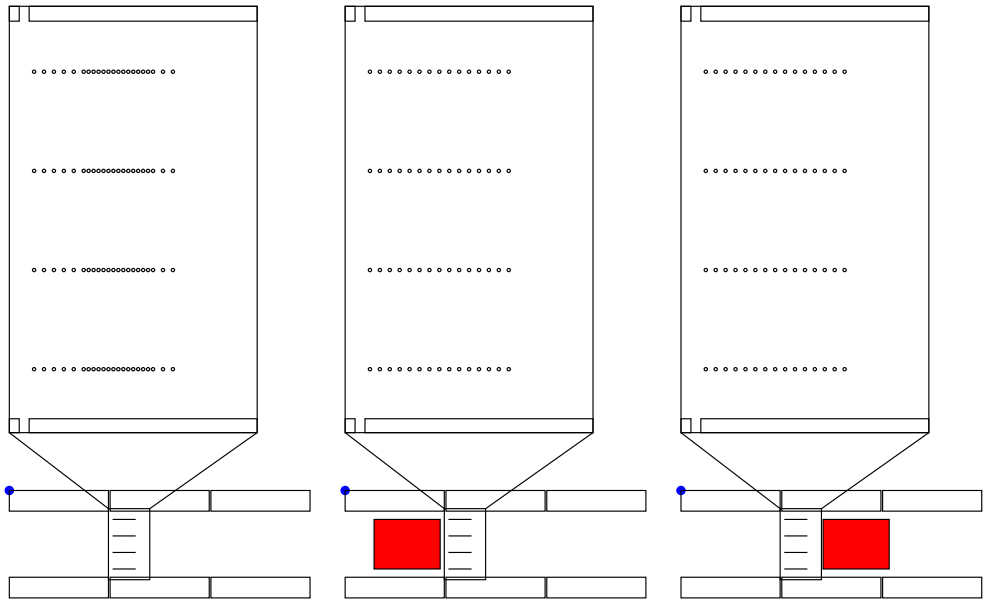

(a) Without vehicle. **(b)** Vehicle on side 1. **(c)** Vehicle on side 2.

Figure 3.4: Dense measurements map.

For each RX position (x, y) we obtain a received power measurement from TX position tx when the RX antenna is oriented in direction ϕ, which we call $R(tx, x, y, \phi)$. In this notation, the TX locations are denoted as $tx \in \{TX1_d, d \in \{63, 73, ..., 113\}; TX2\}$ where d represents the Y component of the distance of the crane from the reference point. We also define the received power in dB as

$$R^{dB}(tx, x, y, \phi) = 10 \log_{10} \left(R(tx, x, y, \phi) \right). \tag{3.1}$$

and the normalized angular spectrum as

$$\hat{R}^{dB}(tx, x, y, \phi) = R^{dB}(tx, x, y, \phi) - 10\log_{10}\left(\frac{1}{2\pi}\int_0^{2\pi} R(tx, x, y, \phi)d\phi\right). \quad (3.2)$$

3.1.2 Angular spread

This section discusses how the received energy is distributed among the azimuthal directions. In particular, in Figs. 3.5 and 3.6, we can observe the histogram and average value of $\hat{R}^{dB}(tx, x, y, \phi)$ over a set of TX and RX positions. More in detail

- In Fig. 3.5a, we can see the statistics of the angular spectrum when the TX is placed at TX1, positioned at a distance of $Y \in \{63, 73, ..., 113\}$m, and the RX is in all the positions depicted in Fig. 3.3a.
- In Fig. 3.5b, we can see the statistics of the angular spectrum when the TX is placed at TX2 and the RX is in all the positions depicted in Fig. 3.3a.
- In Fig. 3.6a, we can see the statistics of the angular spectrum when the TX is placed at TX1, positioned at a distance of $Y \in \{63, 73, 103\}$m, and the RX is in all the positions depicted in Fig. 3.3b.
- In Fig. 3.6b, we can see the statistics of the angular spectrum when the TX is placed at TX2 and the RX is in all the positions depicted in Fig. 3.3b.

In the figures, we can observe that in the vast majority of cases, the channel gain measurements are within 10dB from the average gain for all angles. This suggests that the energy is reaching the RX rather uniformly from all directions. We can also notice that the channel gain is slightly lower for the $0°$ and $180°$ directions in Figs. 3.5a and 3.6a. These two directions correspond to the horn antenna pointed parallel to the canyon. This result can be explained by the NLoS nature of the link. In fact, we expect that the energy is scattered or reflected by some object before reaching the RX. Indeed, in the $0°$ and $180°$ directions, no object can cause scattering or reflections.
In Figs. 3.5b and 3.6b, where the TX is in position TX2, we can instead observe how the gain reduction happens mainly at $0°$. The $180°$ direction, which is facing toward the TX, shows a lower reduction in gain. Despite still not having Line of Sight (LoS) to the TX, the lower reduction in such direction can be explained by the guiding effect of the canyon.

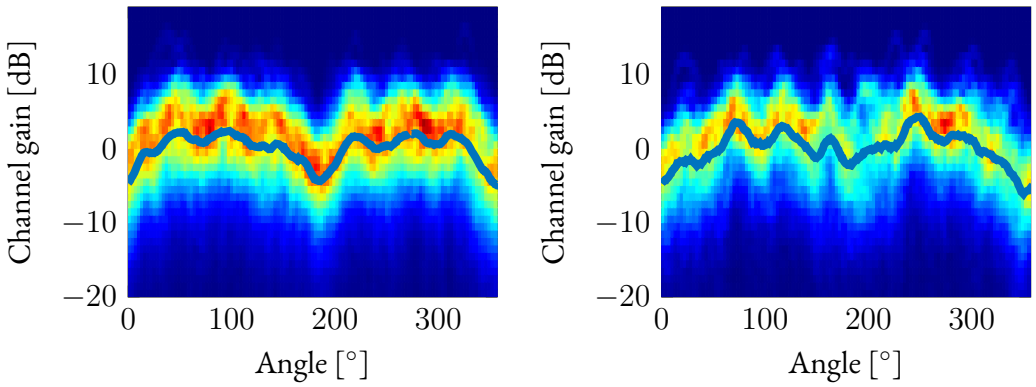

(a) TX1. **(b)** TX2.

Figure 3.5: Angular spectrum with uniform stacking.

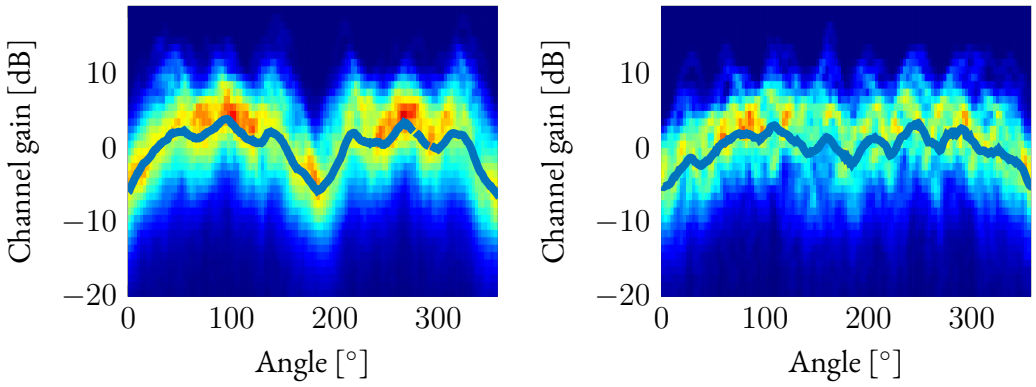

(a) TX1. **(b)** TX2.

Figure 3.6: Angular spectrum with nonuniform stacking.

Fig. 3.7a depicts the distribution of $\hat{R}^{dB}(tx, x, y, \phi)$ computed over all directions $\phi \in [0, 2\pi)$ in comparison to the distribution of $\hat{R}^{dB}(tx, x, y, \phi_{tx}(tx, x, y))$ where, denoting by (x_{tx}, y_{tx}) the location of the TX, we have

$$\phi_{tx}(tx, x, y) = \text{atan2}(y - y_{tx}, x_{tx} - x), \tag{3.3}$$

which is the direction tx of the TX when the RX is placed in position (x, y). As can be observed in the plot, the two distributions are very close, with a difference of at most 2.8dB. This shows that having a narrow beam directly pointing toward the TX will not provide any significant benefit in the real world. Furthermore, Fig. 3.7b shows the distribution of the azimuth gain $\max_{\phi}(\hat{R}^{dB}(tx, x, y, \phi))$ over all TX and RX positions, compared to the

simulated distribution for a fully spread channel, i.e. a channel where the energy is uniformly spread across all angles. Here we can also see a gap of around 2dB between the median gains, further confirming that azimuthal beamforming is not effective.

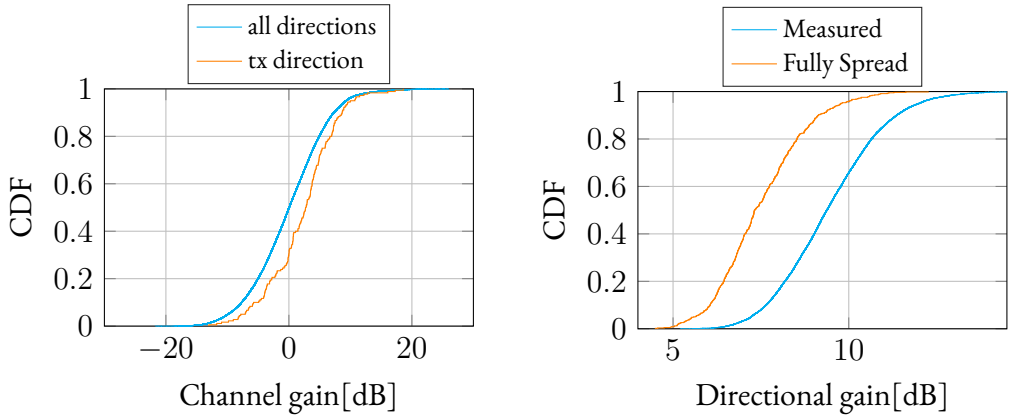

(a) Distribution of the normalized channel gain over all directions and for the TX direction.

(b) Azimuth directional gain.

Figure 3.7: Ineffectiveness of beamforming in a port environment.

3.1.3 Spatial correlation

In this section, we analyze the spatial correlation of $R^{dB}(tx, x_k, y, \phi)$ for a fixed value of ϕ. This is the channel correlation that a user with a fixed beam would observe and, therefore, it provides information on how often the beam should be updated. We use the dense measurement map represented in Fig. 3.4a to perform this analysis. In particular, we use the data collected during the dense sampling, collected with a spatial period of 10cm.
We first define the set $\mathbf{x}$ of X positions corresponding to the 10cm sampling as such that $\{x_1 = 13.5, x_2 = 13.6, ..., x_{15} = 14.9\}$. We also define the average received power for a specific Y position y and angle ϕ as

$$m(tx, y, \phi) = \frac{1}{15} \sum_{k=1}^{15} R^{dB}(tx, x_k, y, \phi), \tag{3.4}$$

and the relative zero mean power as

$$R_0^{dB}(tx, x, y, \phi) = R^{dB}(tx, x, y, \phi) - m(tx, y, \phi). \tag{3.5}$$

With these definitions, we can compute the spatial autocorrelation of the power in the x direction as

$$r(tx, x_k, y, \phi) = \sum_{j=1}^{15-k} R_0^{dB}(tx, x_k, y, \phi) R_0^{dB}(tx, x_{(k+j)}, y, \phi). \tag{3.6}$$

Taking the average over all the angles and Y positions we obtain:

$$r(tx, x_k) = \frac{1}{4} \sum_{y \in \mathcal{Y}} \frac{1}{2\pi} \int_0^{2\pi} r(tx, x_k, y, \phi) d\phi. \tag{3.7}$$

In Fig. 3.8, we plot $r(tx, x_k)$ for the three measured cases. In the plot, we can clearly see that already after 10cm the channel gain is completely uncorrelated. This, in turn, means that the best "direction" remains such for a very short time. This short spatial correlation is consistent with the hypotheses that the energy is received uniformly from all directions and that the best beamforming direction is purely an artifact of fading. It should be noted that, in this case, the best direction would also be frequency selective, further degrading the beamforming gain.

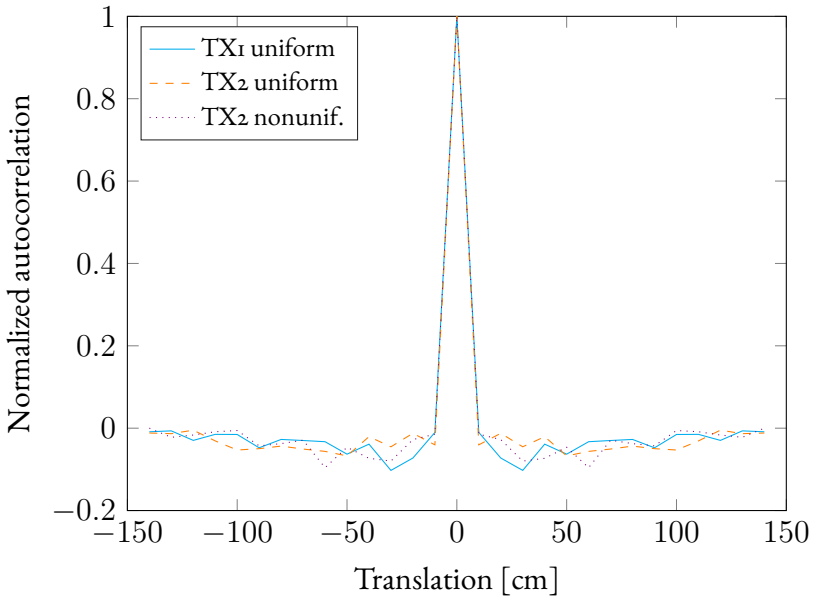

Figure 3.8: Spatial correlation.

3.1.4 Effect of the presence of a vehicle

In this section, we investigate how the presence of a large vehicle inside the canyon, at a few meters from the measurement points, impacts the channel gain. In particular, we define as $R_{v1}^{dB}(tx, x, y, \phi)$ the measured power with the vehicle on side 1 (see Fig. 3.4) and as $R_{v2}^{dB}(tx, x, y, \phi)$ the measured power with the vehicle on side 2. With this definition, we can compute the received power difference with the vehicle in the two positions as

$$\Delta_1(tx, x, y, \phi) = R^{dB}(tx, x, y, \phi) - R_{v1}^{dB}(tx, x, y, \phi), \tag{3.8}$$

$$\Delta_2(tx, x, y, \phi) = R^{dB}(tx, x, y, \phi) - R_{v2}^{dB}(tx, x, y, \phi). \tag{3.9}$$

In Fig. 3.9, we can observe the statistics of $\Delta_1(tx, x, y, \phi)$ and $\Delta_2(tx, x, y, \phi)$ as a function of the angle over all RX positions. The TX is in position TX1 at $63m$ in the Y direction, and the container stacking is uniform. Here the color represents the histogram of the channel gain difference, and the black line represents its mean. We can observe that the difference is independent of the angle and has a mean around zero. This suggests that the vehicle's presence is only impacting the channel gain's local value, but not the overall statistics.

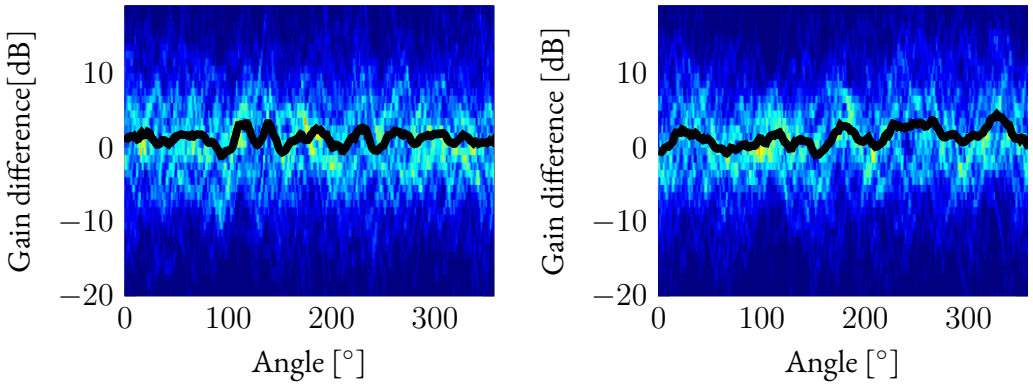

(a) Vehicle position 1.

(b) Vehicle position 2.

Figure 3.9: Statistics of the vehicle effect with uniform stacking and TX1 at 63m.

The angle-independent Cumulative Distribution Function (CDF) of the channel gain difference, computed by aggregating the data over all angles, is depicted in Fig. 3.10, along with a fitted Gaussian distribution. Here we can observe that the CDF matches almost exactly the Gaussian, and the mean is very close to zero, confirming that the vehicle's impact on the channel's statistics is negligible on average. Observing Fig. 3.7a we can also see that the stan-

dard deviation is similar. In particular, the parameters for the fitted Gaussian distributions are listed in Tab. 3.2.

	μ	σ
Vehicle position 1	1.13	6.91
Vehicle position 2	1.37	6.77

Table 3.2: Channel gain difference Gaussian approximation parameters for the uniform stacking and TX1 at 63m.

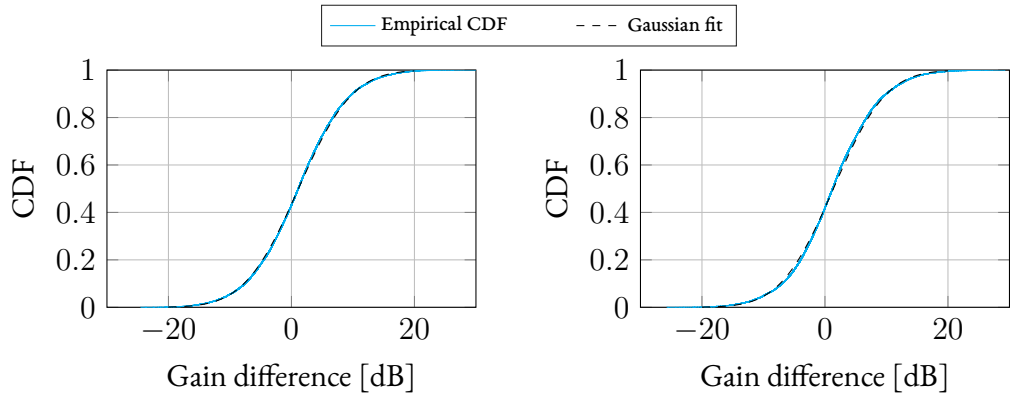

(a) Vehicle position 1.

(b) Vehicle position 2.

Figure 3.10: Angle independent statistics of the vehicle effect with uniform stacking and TX1 at 63m.

In Figs. 3.11 and 3.12, we can observe the same plots for the nonuniform stacking and the TX in positions TX2. Indeed, in this case, the effect on the average channel gain is also limited, and the difference is approximately Gaussian with the parameters listed in Tab. 3.3.

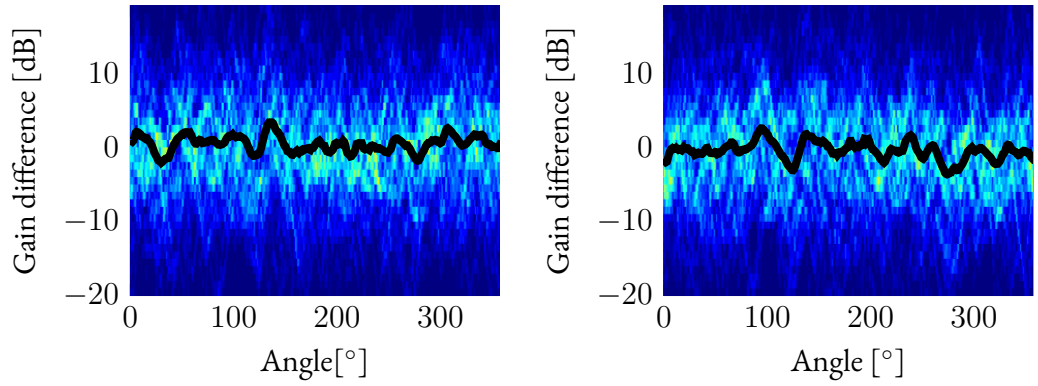

(a) Vehicle position 2.

(b) Vehicle position 2.

Figure 3.11: Statistics of the vehicle effect with nonuniform stacking and TX2.

	μ	σ
Veichle position 1	0.40	7.09
Veichle position 2	−0.54	7.07

Table 3.3: Channel gain difference Gaussian approximation parameters for the nonuniform stacking and TX2.

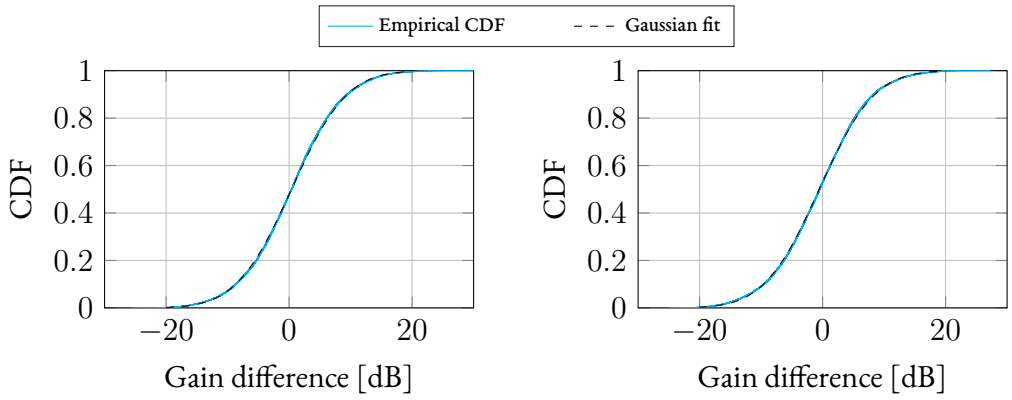

(a) Vehicle position 2.

(b) Vehicle position 2.

Figure 3.12: Angle independent statistics of the vehicle effect with nonuniform stacking and TX2.

3.1.5 Path loss

This section discusses the path loss of the measured links and its impact on the communication system. Using a narrow HPBW horn antenna rotated only in azimuth for this measurement poses a challenge in estimating the performance of a communication system with different antenna patterns in this scenario. It, in fact, does not provide any information on the elevation angle at which the energy is received. In this scenario, where the energy is propagating from the top of a tall structure down to the user, this issue is particularly relevant, as it is very likely that the energy will reach the user from above. In order to obtain reliable channel information for different antenna patterns, we used the data to validate a simulation setup. We recreated the environments and devices in CST microwave studio*, an electromagnetic simulation tool that include both full wave and asymptotic solvers. We performed the simulation with the asymptotic physical optics solver. The main parameters used are listed in Tab. 3.4.

*version 2022, https://www.3ds.com/products-services/simulia/products/cst-studio-suite/

Parameter	Value
number of intersections	5
Ray spacing	5 λ
Adaptive ray sampling	yes
Maximum ray distance	10 λ
Minimum ray distance	0.2 λ

Table 3.4: Main simulation parameters.

From both the measured and simulated data, we evaluated the channel gain averaged over angle in dB, which is

$$R_{avg}^{dB}(tx, x, y) = 10 \log_{10} \left(\frac{1}{2\pi} \int_0^{2\pi} R(tx, x, y, \phi) d\phi \right), \tag{3.10}$$

and compared the values obtained from the measurement with those given by simulations. Note that, in this setting, we define the channel gain as the ratio between the power at the RX antenna port and the power at the TX antenna port. It, therefore, is also a function of the antenna pattern, which has also been replicated in CST based on anechoic chamber measurement. This definition is necessary as we cannot compensate for the antenna gain without knowing the elevation pattern of the received signal. In Fig. 3.13, we can observe the simulated and measured values of $R_{avg}^{dB}(tx, x, y)$ as a function of the Euclidean distance $\bar{D}$ between the TX and RX. As discussed in the previous sections, the multipath is extremely rich, which makes the channel gain dependent on fading. As fading changes at the wavelength scale, which in this case is a few millimeters, and the RX's positioning was not accurate to this scale, we do not expect a match between the measured and simulated power. Therefore we also include a log-linear fit of the data with the equation

$$R_{fit}^{dB}(\bar{D}) = 10n \log_{10}(\bar{D}) + R_0. \tag{3.11}$$

The parameters of the fitting lines can be found in Tab. 3.5. Here we can see that the prediction matches the measurements within a tollerance of 3dB in intercept and 10% in slope, and they are coherent within the confidence interval. Based on this result, we consider the simulated channel gain to be a good approximation of reality and use it for further studies.

Configuration	n	R_0 [dB]	RMSE[dB]
Measured Uniform	-1.99 ± 0.29	-63 ± 5.67	1.6
Measured Nonuniform	-1.543 ± 0.33	-67.8 ± 6.5	1.9
Measured Aggregated	-2.18 ± 0.34	-57.4 ± 6.7	2.71
Simulated Uniform	-1.88 ± 0.37	-64 ± 7.3	1.9
Simulated Nonuniform	-1.78 ± 0.43	-66.4 ± 8.7	2.3
Simulated Aggregated	-1.82 ± 0.29	-65.3 ± 5.7	2.1

Table 3.5: Line fit parameters (95% confidence interval).

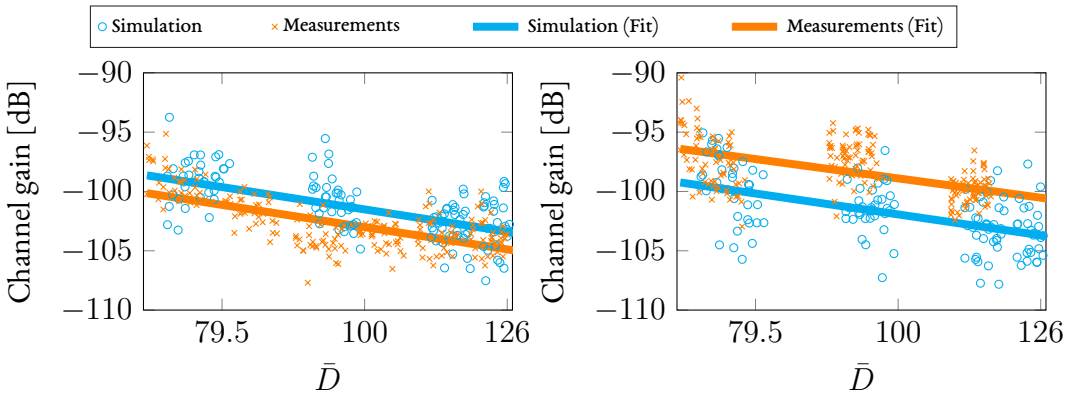

(a) TX1, uniform stacking.

(b) TX1, nonuniform stacking.

Figure 3.13: Measured and simulated channel gain.

Fig. 3.14 shows the simulated channel gain when the RX horn antenna is replaced with an omnidirectional antenna. Comparing the simulated channel gain with the Free Space Path Loss (FSPL) associated with the geometric distance between the TX and RX, we observe that the difference in channel gain is lower than 10dB for all measured positions. This clearly shows that the highly reflective environment can overcome the limitations of NLoS communication for mmWave, and also further suggests that the channel will show rich multipath. The slopes in Tab. 3.6 are significantly higher than free space. Comparing the results with the horn antenna measurements, which have a slope smaller than 2 we can conclude that the further the TX is from the canyon, the more the energy concentrates in the horizontal plane. This is also in line with the system's geometry, as the angle of incidence of the wavefront with the top of the canyon gets shallower at larger distances.

	Simulated		
Stacking	n	R_0 [dB]	RMSE[dB]
Uniform	-4.53 ± 0.29	-16.2 ± 5.8	2.27
Nonuniform	-3.67 ± 0.28	-30.3 ± 5.5	2.2
Aggregate	-4.09 ± 0.25	-23.4 ± 4.9	2.73

Table 3.6: Line fit parameters for omnidirectional antenna (95% confidence interval).

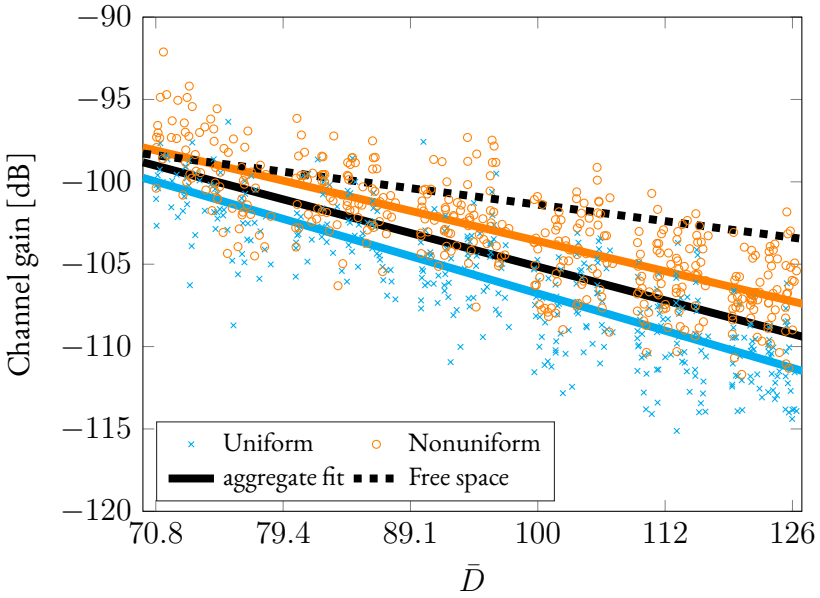

Figure 3.14: simulated channel gain with omnidirectional antennas.

Based on this data, we can estimate the coverage of a typical 5G Base Station (BS) in such an environment. To do so, we use the following assumption:

1. A BS with a transmitting power of 28dBm per polarization per panel, and an antenna gain of 23dBi, for a total Equivalent Isotropic Radiated Power (EIRP) of 51dBm.
2. A shadow-fading margin of 10dB.
3. A bandwidth of 400MHz with at a temperature of 300K and a RX noise figure of 10dB, resulting in a noise floor of -77.8dBm.
4. A minimum spectral efficiency of 2 bit/s/Hz (4 bit/s/Hz with dual polarization, resulting in 1.6Gbps with the 400MHz bandwidth), for which we require a Singal-to-Noise Ratio (SNR) of 8dB [36].

5. A UE with an omnidirectional antenna.

With these assumptions, the maximum path loss is EIRP + Noise floor − Minimum SNR − Shadow-fading margin $= 51 + 77.8 - 8 - 10 = 110.8$dB. We consider the aggregated fit from Tab. 3.6, which has a slope of 4.09 and an intercept of -23.4. These values result in a channel gain of -110.8dB around 137m. Clearly, despite the common idea that higher frequencies are not suitable for NLoS communication, in this scenario, such communication is feasible. We also note that the spectral efficiency requirement we used for this calculation is quite stringent, and practical transceivers will have different antennas, which are likely to perform better than the omnidirectional. Therefore, we can expect good performance even beyond this distance.

3.1.6 Propagation model

The observations on the angular spectrum suggest that the energy propagates in a very chaotic and complex manner in the horizontal plane after entering the canyon. Therefore we would expect that the amount of energy received by the UE only depends on the amount of energy entering the canyon and the vertical propagation inside it. To test this hypothesis, we compute the power the UE would receive under this assumption.

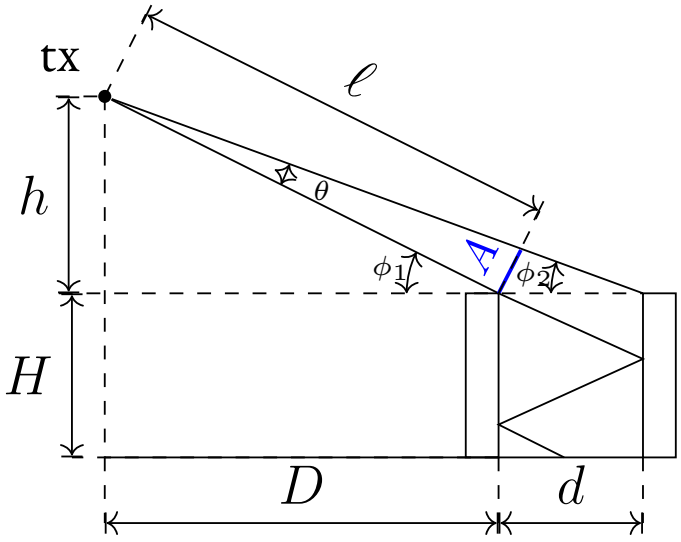

Figure 3.15: Container canyon propagation model (side view).

We call ν the fraction of the energy entering the canyon that actually reaches the RX. Approximating the signal impinging on the top of the canyon as a plane wave with Poynting

vector S, the power entering the canyon is proportional to the area of the top opening of the canyon projected on a plane orthogonal to the wave vector of the plane wave. In particular, if we consider the energy entering a section of the canyon of length L and we call the projected canyon aperture A, as depicted in Fig. 3.15, the received power would be

$$P_{RX} = \nu L A |S|. \tag{3.12}$$

Since there are typically no objects above the canyon level, $|S|$ can be computed as the FSPL between the TX and the canyon, which in this case is proportional to

$$|S| \propto \ell^{-2} = \left(\sqrt{h^2 + D^2}\right)^{-2}. \tag{3.13}$$

Assuming θ is small, the aperture A can be approximated as

$$A \approx \ell \sin(\theta) = \left(\sqrt{h^2 + D^2}\right) \sin(\theta). \tag{3.14}$$

We note that

$$\theta = \phi_2 - \phi_1; \tag{3.15}$$

$$\phi_1 = \tan^{-1}\left(\frac{h}{D}\right); \tag{3.16}$$

$$\phi_2 = \tan^{-1}\left(\frac{h}{D+d}\right). \tag{3.17}$$

Therefore, we can write

$$\theta = \tan^{-1}\left(\frac{h}{D+d}\right) - \tan^{-1}\left(\frac{h}{D}\right) \tag{3.18}$$

and

$$A \approx \ell \sin(\theta) = \left(\sqrt{h^2 + D^2}\right) \sin\left(\tan^{-1}\left(\frac{h}{D+d}\right) - \tan^{-1}\left(\frac{h}{D}\right)\right). \tag{3.19}$$

We can now rewrite the received power as

$$P_{RX} = \nu L A |S| \tag{3.20}$$

$$\approx \nu L \left(\sqrt{h^2 + D^2}\right) \sin\left(\tan^{-1}\left(\frac{h}{D+d}\right) - \tan^{-1}\left(\frac{h}{D}\right)\right) \left(\sqrt{h^2 + D^2}\right)^{-2} \tag{3.21}$$

$$= \nu L \left(\sqrt{h^2 + D^2}\right)^{-1} \sin\left(\tan^{-1}\left(\frac{h}{D+d}\right) - \tan^{-1}\left(\frac{h}{D}\right)\right). \tag{3.22}$$

We can now perform some small angle approximations to simplify the expression further. We assume $D \gg h$, i.e., we consider the case where the TX is far from the canyon, which is the most relevant and challenging case as it represents the cell edge case. Thanks to this assumption, we can say that also ϕ_1 and ϕ_2 are small, and use a first-order approximation of the arctangent in (3.16) and (3.17). Therefore, we write

$$\phi_1 \approx \frac{h}{D} \quad \text{and} \quad \phi_2 \approx \frac{h}{D+d}. \tag{3.23}$$

This simplifies the received power to

$$P_{RX} \approx \nu L \left(\sqrt{h^2 + D^2}\right)^{-1} \sin\left(\frac{h}{D+d} - \frac{h}{D}\right) = \nu L \left(\sqrt{h^2 + D^2}\right)^{-1} \sin\left(\frac{hd}{D^2 + dD}\right). \tag{3.24}$$

Furthermore, we have that $h^2 + D^2 \approx D^2$, further simplifying the expression to:

$$P_{RX} \approx \frac{\nu L}{D} \sin\left(\frac{hd}{D^2 + dD}\right). \tag{3.25}$$

Under the assumption of far TX, it also holds that $D \gg d$, hence we can approximate $D^2 + dD$ with D^2, obtaining

$$P_{RX} \approx \frac{\nu L}{D} \sin\left(\frac{hd}{D^2}\right). \tag{3.26}$$

Finally, by the assumptions above, we note that $D^2 \gg hd$, and therefore $\frac{hd}{D^2}$ is small, so we can use the first order approximation of the sine to obtain the final expression

$$P_{RX} \approx \frac{\nu L}{D} \frac{hd}{D^2} = \frac{\nu L h d}{D^3}. \tag{3.27}$$

The value of L can be computed assuming that the energy reaches the RX only if it enters the canyon at a shallow azimuth angle. Fig. 3.16 illustrates the geometry of the system.

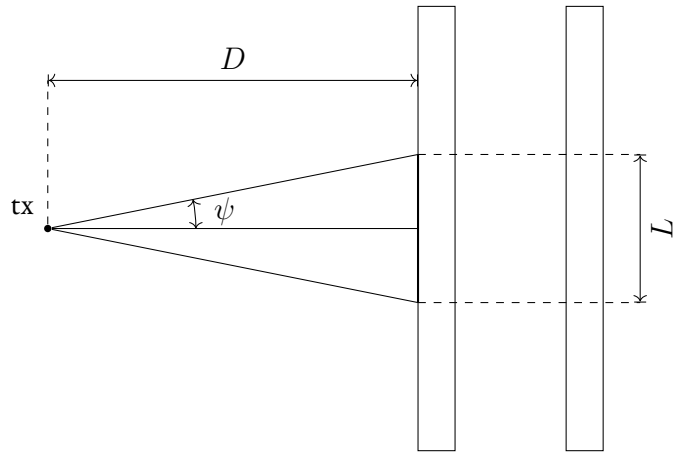

Figure 3.16: Container canyon propagation model (top view).

In this figure, we can easily see that, calling the maximum azimuthal angle ψ, the length of the canyon section accepting energy can be expressed as

$$L = D\sin(\psi) \approx D\psi. \tag{3.28}$$

Let us now consider the value of ν. The length of the path followed by the signal inside the canyon corresponds to the length of ℓ' in Fig. 3.17.

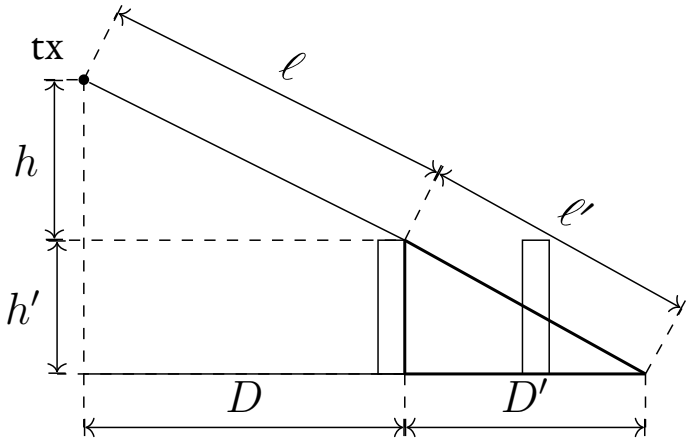

Figure 3.17: propagation inside the canyon.

By triangles similarity, we can write

$$\frac{h}{D} = \frac{h'}{D'} \Rightarrow D' = \frac{h'D}{h}. \tag{3.29}$$

We can then write

$$\ell' = \sqrt{(h')^2 + (D')^2} = \sqrt{(h')^2 + \left(\frac{h'D}{h}\right)^2}. \tag{3.30}$$

By the assumption that D is large, we can approximate it with

$$\ell' \approx \sqrt{(D')^2} = \sqrt{\left(\frac{h'D}{h}\right)^2} = \frac{h'D}{h} \tag{3.31}$$

and write

$$\nu \propto \frac{1}{(\ell')^2} = \left(\frac{h}{h'D}\right)^2 \propto \frac{1}{D^2}. \tag{3.32}$$

Replacing (3.28) and (3.32) in (3.27), we can write the final expression for the received power as

$$P_{RX} \propto \frac{\nu L h d}{D^3} = \underbrace{D\psi}_{L} \underbrace{\frac{1}{D^2}}_{\nu} \frac{hd}{D^3} = \frac{\psi h d}{D^4}. \tag{3.33}$$

Notably, the numerator ψhd is constant. This predicts that the received power decreases with the fourth power of the distance, compared to the free space model, which decreases with the second power. This model already matches quite well the observation of Fig. 3.14 and Tab. 3.6. However, to further verify its correctness, we fit the data with a slope of $n = 4$, as predicted by (3.33). Fig. 3.18 shows such model fit. It is clear that the fit shown is very similar to the one depicted in Fig. 3.14. Moreover, Tab. 3.7 shows the fit parameters and the Root Mean Square Error (RMSE) obtained with $n = 4$. Clearly, the RMSE obtained has a negligible difference from the one shown in Tab. 3.6, showing that assuming $n = 4$ does not degrade the fit significantly.

	Simulated	
Stacking	R_0 [dB]	RMSE[dB]
Uniform	-26.7 ± 0.22	2.3
Nonuniform	-23.63 ± 0.21	2.22
Aggregate	-25.13 ± 0.19	2.73

Table 3.7: Model fit parameters (95% confidence interval).

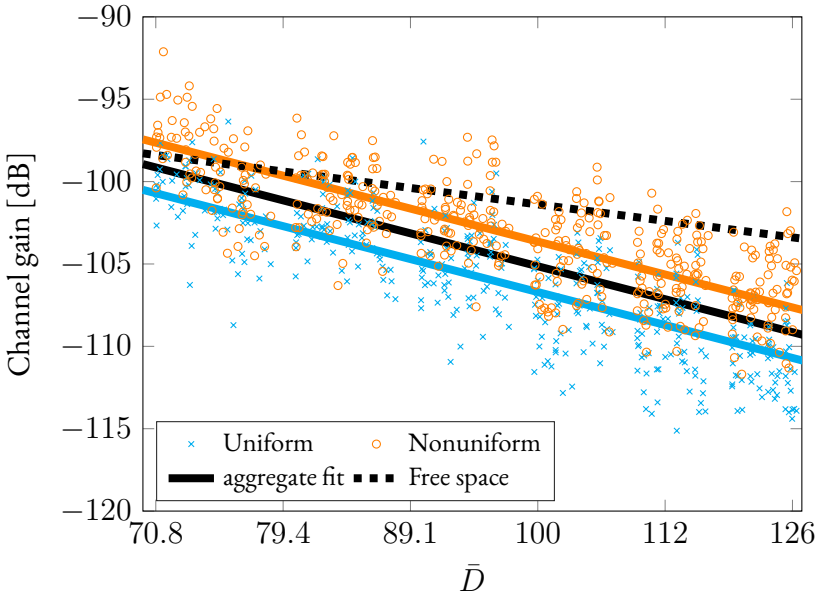

Figure 3.18: Channel gain model fit.

We note that the relevance of this model is not mainly in the ability to predict the slope but in the insight it gives into the propagation mechanisms. In particular, it is consistent with the hypothesis that the received power only depends on vertical propagation, reinforcing such a claim with further evidence.

3.1.7 Elevation spectrum

Fig. 3.19 shows the relation between the channel gain and the elevation angle of the incident wave direction. It was realized by simulating the channel with the horn antenna kept at a fixed azimuthal angle of $\phi = 90°$, i.e., pointed towards the side of the canyon where the TX is located, rotating it to different elevation angles. The simulation is repeated for two positions of TX1, the first at 63m and the second at 113m, with the nonuniform container stacking.

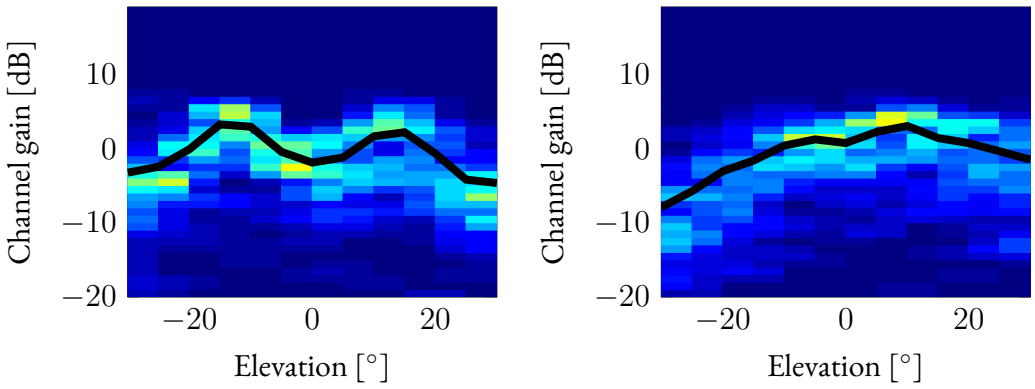

(a) TX1 at 63m.

(b) TX1 at 113m.

Figure 3.19: Elevation spectrum for the nonuniform configuration.

Here we can clearly see a dependence of the elevation angle of arrival of the distance between the TX and the canyon. In particular, in Fig. 3.19a, we see that the energy is concentrated around a relatively sharp angle of roughly $15°$. In contrast, Fig. 3.19b shows that most of the energy is concentrated near the horizontal direction, slightly below $10°$. If we consider the system's geometry, we have $h = \text{TX height} - \text{Canyon height} = 23 - 5 = 18\text{m}$ for most of the canyon for such stacking. using this value, we can compute $\phi_1 = \tan^{-1}\left(\frac{h}{D}\right)$ for the two cases, with $D = 65.5\text{m}$ for the first case and $D = 115.5\text{m}$ for the second. Doing so, we obtain the corresponding elevation angles of $15.4°$ and $8.8°$, consistent with what can be seen in the figures. This fact also explains the difference in slope observed between the measurements and simulations with the horn antenna (Tab. 3.5) and the simulations with the omni antenna (Tab. 3.6). In the former case, the slope results are lower because the further we move, the shallower the elevation angle, which means that the gain of the antenna is better exploited at larger distances.

As we have observed in Sec. 3.1, the usual model of a sparse channel with few distinct multipath components that is often assumed in, e.g., indoor environments for mmWave [8], is not a good assumption in the presence of large metallic objects. The main channel characteristics observed in an industrial environment, where such objects are present in large numbers, can instead be summarized as follows:

- Despite the NLoS nature of the link, the path gain is remarkably high. For example, in the presented case, the fit of the path gain is within 10dB from the FSPL for all considered cases, and a commercial mmWave BS can provide service in at a distance exceeding 100m.
- The received power does not concentrate in a single direction as it happens in LoS in a non-metallic environment. Instead, in the presented case, the angular pattern is nearly uniform, i.e., the energy is received from all directions in equal amounts.
- The received power for a fixed direction decorrelates quickly as the RX moves through space. In the presented case, within less than 10cm. This shows that the variations in power for a fixed direction mostly depend on fast fading.
- Changes in the environment, such as the presence of large vehicles in the canyon, might not significantly impact the channel characteristics.

These channel characteristics have also been observed in different industrial plants [9, 10, 11, 27] and have proven to be a common feature of all those environments with a high presence of large metallic structures. Their impact on the communication system design is also listed in the following

- The channel gain observed in NLoS is sufficient to communicate effectively. Therefore, the network can be built without the requirement of having LoS in all locations. This allows for the use of fewer BSs, thus reducing the CapEx.
- As many of the modern mmWave devices are designed with the assumption of LoS communication and therefore use beamforming that is well suited for a simple channel where all the energy is concentrated in a single plane wave, such devices might perform poorly in NLoS scenarios.

- For similar reasons, modern mmWave devices are not designed to operate with a rich multipath channel and therefore cannot exploit the spatial diversity that such a channel provides.

These considerations suggest that, for the industrial use case, we should revise the design of our mmWave devices to be more effective in NLoS rich multipath environments.

4

Beamforming architectures

This chapter discusses the hardware beamforming architectures and whether they are suited to the channel characteristics observed in Chap. 3. In particular, in Sec. 4.1, we note that the classical analog and hybrid beamforming architectures are designed with LoS or sparse channels in mind, whereas the channel observed in industrial environments shows a rich multipath. In Sec. 4.2, we propose a novel architecture capable of trading bandwidth for rank, which is better suited for such channels. Moreover, in Sec. 4.3, we provide a comparison of the classical and proposed architecture in terms of complexity, cost, and power consumption, showing that such architecture is slightly more complex and expensive than a hybrid beamforming architecture, but still far simpler and cheaper than fully digital beamforming.

4.1 Classical beamforming architectures

The classical fully connected hybrid beamforming architecture, depicted in Fig. 4.1, is widely used in the industry for mmWave communications. However, this architecture has some limitations that can impact its effectiveness in industrial wireless communication systems. One of the main limitations is the need for lengthy and complex beam training and refinement procedures to establish and maintain a connection. Before transmitting a signal, the system needs to determine the optimal beam direction and shape, which involves sweeping through different beam directions and measuring the channel response. This process can take a long time, and needs to be performed for each user within the system, so it can be-

come a significant overhead, especially when the number of users is large. In classical LoS communications, this might not be an issue, as the LoS directions vary smoothly and slowly. In industrial environments though, as discussed in Sec. 3.1.3, the optimal beam direction is very dynamic, exacerbating the overhead issue. Additionally, this beam training and refinement procedures can cause an excess delay in time-sensitive packets, as communication is not possible while the system is training the beam. Secondly, due to the limitations in CSI acquisition capability (i.e., the inability of the system to acquire the full channel matrix, but rather only to measure the power for a specific beam), modern wireless communication systems often make use of a small codebook of pencil beams to limit the number of channel measurements [37]. These beams concentrate the array gain in a single spatial direction and are effective in maximizing throughput for a LoS scenario with limited reflections, where the signal can travel directly from the transmitter to the receiver without obstructions and with little multipath. However, when operating in an environment with rich multipath, using directional beams comes at a cost. By focusing on a single multipath component, directional beams sacrifice spatial diversity. Hence, when the selected component is blocked by an obstacle, this strategy is likely to experience a complete signal loss and, thus becoming unable to communicate until a time-consuming beam training is performed.

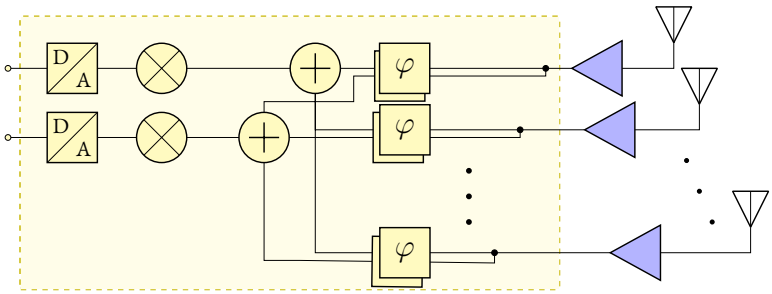

Figure 4.1: Classical fully connected hybrid beamforming hardware architecture.

The naïve solution to this issue is to use a fully digital beamforming architecture. The Radio Frequency (RF) frontend of such an architecture is depicted in Fig. 4.2. Note that, for shortness, in the following we will refer to an RF frontend that enables the implementation of digital beamforming as a *digital beamforming architecture*. This architecture allows the receiver to collect the full signal for all antennas and perform combining in the digital domain.

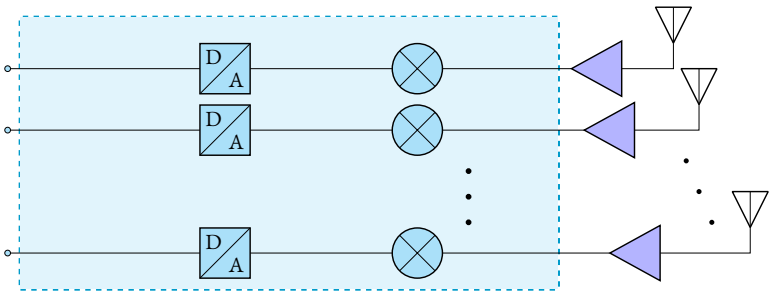

Figure 4.2: Classical fully digital beamforming hardware architecture.

This provides several advantages, including

- The ability to combine signals from different antennas with different coefficients at different frequencies. This allows for the coherent combining of the multipath components and, therefore, a much higher beamforming gain.

- The possibility to acquire full CSI from just the demodulation reference signals without long and costly beam training operations. This enables overhead-free beamforming, as well as the ability to design better and more complex beams. It also makes it possible to efficiently perform localization and sensing tasks by observing the channel estimates, without impacting the communication.

- The ability to perform spatial multiplexing, i.e., to send individual data streams to different receivers at the same time and frequency, separating the data streams by appropriately combining the signal from each antenna.

Unfortunately, this architecture may not be feasible, especially on the UE side, due to cost and power consumption constraints. Finally, although in a multi-user environment each users' resource allocation might be localized in frequency, a UE implementing this architecture is typically receiving on the whole bandwidth at all times with the same capabilities. For example, let us consider the resource grid depicted in Fig. 4.3.

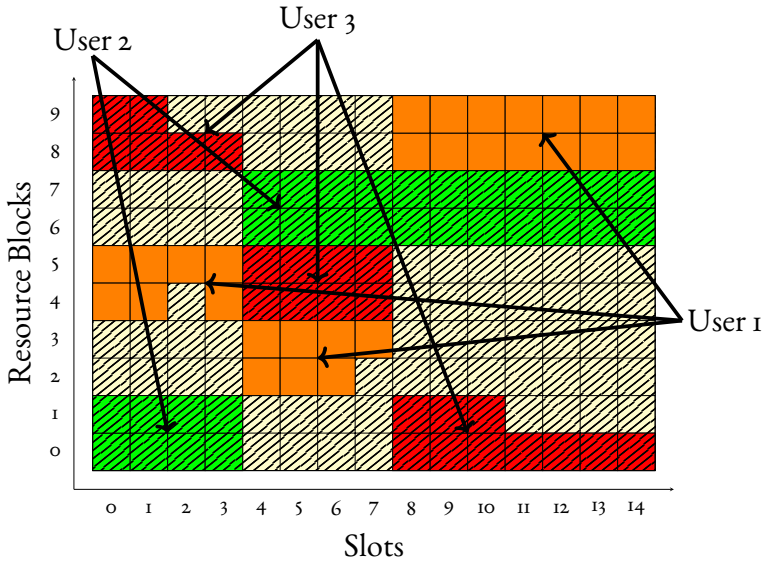

Figure 4.3: Example resource grid.

Here the horizontal axis represents time, the vertical axis frequency, and the squares the Resource Blocks (RBs) that can be assigned to users. The RBs are colored according to the user they are allocated to. Let us now consider the user 1 (orange). We can note that, out of the 150 available RBs, it exploits only 28 RBs, corresponding to roughly 18.7% of the nominal capacity. With a classical beamforming system, the user would receive and process the signal over all the resource elements, thus wasting 81.3% of the data acquired, represented in the picture by the black stripes. Note that, despite being more expensive and complex, even the fully digital beamforming architecture suffers from this inefficiency.

To overcome the limitations listed in Sec. 4.1, we require a system that is both wideband, to support high data rates when necessary and acquire control signaling that might be allocated throughout the band, and high rank at least in a fraction of the frequencies, to exploit the benefits of digital beamforming. This should also obviously be achieved while maintaining practical costs and power consumption. While a fully digital Multiple Input Multiple Output (MIMO) architecture would satisfy the former constraints, it fails on the last: its implementation is inherently costly and power-hungry due to the need for multiple high-speed ADCs. Therefore, this thesis proposes the architecture depicted in Fig. 4.4.

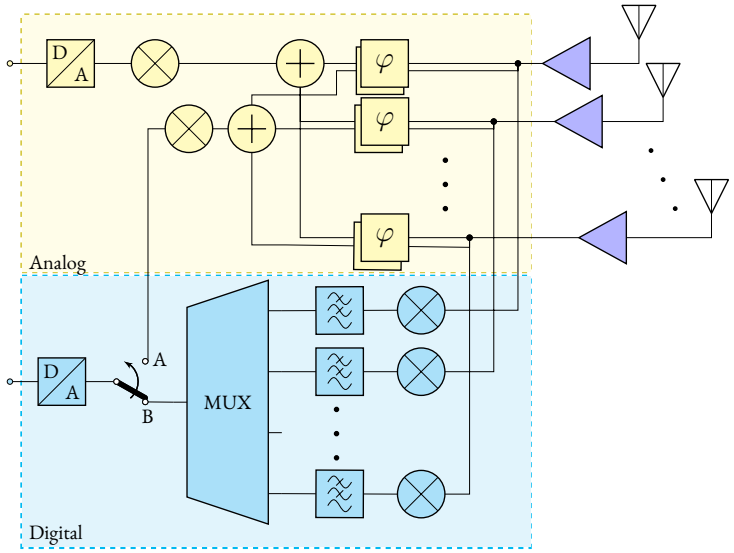

Figure 4.4: Heterogeneous rank hardware architecture. The wideband analog beamforming and the narrowband fully-digital beamforming blocks are highlighted in yellow and blue, respectively.

This architecture comprises N antennas connected to a certain number of classic analog beamforming chains (marked in yellow in the figure), which operate on the full bandwidth B_A of the system. In particular, the signal from each antenna is amplified by a Low Noise Amplifier (LNA), phase shifted and added together in the analog domain. Subsequently, the combined signal is downconverted and digitalized by a single high-speed ADC.

Besides the classical system, that is enabled when the switch is in position B, we implement an additional dedicated RF chain (marked in light blue) with a narrower bandwidth for each antenna. In particular, when the switch is in position A, the signal from each antenna can be extracted after the fronted LNAs, individually downconverted to baseband, and filtered by

a Low Pass Filter (LPF). We now re-purpose one or more ADCs formerly used for one of the analog beamforming chains to digitalize these signals by multiplexing all the low-bandwidth individual antenna signals into that ADC to obtain a low-bandwidth digital beamforming chain.

We note that, with this method, we can allocate the samples of the ADC to acquire a smaller part of the bandwidth with a higher rank, thus reducing the wasted samples used by classical architectures to digitalize the full bandwidth even when the data is localized in frequency. Moreover, this ease of acquisition can enable better and more complete CSI estimation, thus allowing for more sophisticated beam design strategies than the classic directional beam, that can exploit the diversity of the rich multipath environment observed in factories. For the sake of simplicity, in this thesis we will focus on the case with 2 RF chains, one of which is equipped with the additional hardware to perform narrowband digital beamforming. Finally, we note that the mixers belonging to the digital beamforming chain do not necessarily need to be fed with the same Local Oscillator (LO) frequency of the analog beamforming. Therefore we can assume the center frequency of the digital beamforming part is anywhere within or outside the one of the analog beamforming. Note that, the proposed architecture can entail any number of RF chains, of which any subset can be converted to digital beamforming, clearly with higher cost, complexity, and power consumption.

To summarize, in this thesis we assume that the following architecture can operate in two modes

- *Hybrid mode*, where the switch is in position A, and both ADCs are connected to an analog beamforming chain, and operate on the full bandwidth B_A.
- *Heterogeneous mode*, where the switch is in position B. Here the first ADC is still connected to the analog bemaforming chain, and operates on the full bandwidth B_A, whereas the second ADC is multiplexed between all the antennas, and therefore operates in digital beamforming on a reduced bandwidth $\frac{B_A}{N}$.

4.3 Complexity, power consumption and cost analysis

This section discusses the proposed architecture's power consumption and complexity compared to the classical hybrid and fully digital beamforming architectures. We consider a system with a 28GHz carrier and 400MHz bandwidth, and select off-the-shelf components for the comparison. These were chosen through a thorough web search, filtering for the characteristics required to meet the system specifications. The search result is then sorted by price and the cheapest component is chosen. It should be noted that the selected components are just examples to illustrate the main design trade-offs, and they might not entirely reflect the final cost and power consumption of an integrated device. This exercise however can give important insights into the costs and complexity associated with the hardware aspects of the proposed architecture.

The components selected for the comparison, as well as their main characteristics, are listed in the following:*

- The mixer is the Mini-Circuits MDB-54H+ [38]. It operates in the 20-50GHz frequency range and requires an LO power of 15dBm (roughly 32mW). Its price is 30.66€.
- The ADC is the Texas Instruments ADS5403 [39]. It is capable of sampling at a rate of up to 500Msps with a 12bit resolution, which is sufficient to handle the required maximum bandwidth of 400MHz. It has a total power dissipation of 1W and costs 152.61€.
- The LNA is the Mini-Circuits PMA3-313GLN+ [40]. It operates between 26.5 and 31GHz with a gain of 18dB. It is designed for a 4V power supply with a biasing current of 78mA, for a total power consumption of 312mW. Its price is 33.43€.

Since modern communication systems typically use IQ sampling, each RF chain requires 2 mixers and 2 ADCs. All other components (multiplexer, phase shifters, and filters) are cheap and have low power consumption. They are therefore excluded from this analysis.
Let us now consider a system with 32 antennas. The required amount of components to build such a system is listed in Tab. 4.1.

Assuming the LO generation has an efficiency of 50%, the power needed to generate the reference signal for each mixer is $2 \times 32\text{mW} = 64\text{mW}$. Using this number, we can compute the power consumption of each system, listed in Tab. 4.2

*All prices refer to those listed in the DigiKey website on September 2023, for a quantity of 25 pieces.

Architecture	# of mixers	# of ADCs	# of LNAs
Hybrid	4	4	
Proposed	64	4	32
Fully digital	64	64	

Table 4.1: Components required by each type of architecture.

Architecture	mixers	ADCs	LNAs	total
Hybrid	256mW	4W		14.26W
Proposed	4.1W	4W	10W	18.1W
Fully digital	4.1W	64W		78.1W

Table 4.2: Comparison of the power consumption of each architecture.

As we can clearly see, the ADCs contribution is way more significant than that of the mixers. As a consequence, the power consumption of fully digital architecture, which requires as many ADC as the number of antennas, is more than 5 times larger than that of the hybrid beamforming architecture. Instead, the proposed architecture, which can reuse the same ADC for multiple antennas, has only slightly larger power consumption (+30%) with respect to the hybrid architecture It should be noted that, in industrial applications, UEs that need high-performance communications typically do not suffer from a lack of power. They are, in fact, usually mounted on robots that consume hundreds or thousands of Watts, making the transceiver power consumption negligible. The limiting factor, instead, is the thermal output of the device, as this needs to be kept within operating temperatures. In the example above, the hybrid and proposed architectures can probably be cooled with a passive heatsink of limited size. In contrast, the fully digital architecture will likely require a large heatsink, which might be problematic in terms of space constraints, and an active cooling component such as a fan or a water pump, that can be an issue as they suffer from wear, especially in the harsh conditions of manufacturing plants, and therefore require active maintenance and are prone to cause disruptions when they get damaged. Another factor to consider is the cost of the components. The costs listed before are for low quantities and are not the final production costs. Moreover, such a system would most likely be integrated into a few chips instead of being composed of individual monolithic parts for each component. However, for the sake of this evaluation, we will assume that the cost ratios between the components are similar to those of the final implementation. This is a reasonable assumption for a rough estimate, assuming the dimensional factors of the macro-components are somehow maintained in their integrated version, and considering that the cost of the Integrated Circuits

(ICs) depends on their footprint in silicon.From the number of components indicated in Tab. 4.1 we can hence estimate an indicative cost of each architecture, as shown in Tab. 4.3.

Architecture	mixers	ADCs	LNAs	total
Hybrid	122.64€	610.44€		1802.84€
Proposed	1962.24€	610.44€	1069.76€	3642.44€
Fully digital	1962.24€	9767.04€		12799.00€

Table 4.3: Comparison of the cost of each architecture.

We can observe that the cost of the proposed architecture about twice that of the classical hybrid beamforming, whereas the fully digital architecture is more than 7 times more expensive. In future factories, where we expect a massive number of connected devices, such difference might have a very significant CapEx impact.

Finally, we consider the complexity associated with the various architectures. To roughly quantify the processing complexity required to use such architectures, we consider the data rate of the samples generated by the systems. In particular, the hybrid beamforming architecture has 4 ADCs generating 500 million 12-bit samples per second, for a total of 24Gbps of data. The proposed architecture, having the same amount of ADCs, will generate the same amount of data to be processed by the baseband. In contrast, the fully digital beamforming architecture uses 64 ADCs for a total data rate of 384Gbps. If we assume that the processing time scales linearly with the number of bits generated by the ADCs, the digital beamforming architecture would therefore require 16 times more processing power than the proposed and hybrid architectures, therefore also consuming 16 times the power in the digital domain. In addition, we observe that not all of the signal processing algorithms employed in a modern receiver have linear complexity, therefore the gap in the required processing capabilities and power consumption will likely be even larger. In summary, the proposed architecture is clearly an interesting middle ground between the classical hybrid beamforming and the highly complex fully digital beamforming architectures in terms of cost, complexity, and power consumption.

5

System Model

In this thesis, we consider a system as depicted in Fig. 5.1, where a BS transmits data to a UE in a multipath environment. As we are considering an industrial setting, and based on the findings of Chap. 3, we note that this channel will show a very rich multipath. The UE receives the signal transmitted by the BS with an arbitrary antenna array composed of N antennas. Despite in practice BSs being multi-antenna systems too, to present the content of this thesis, it is sufficient to consider a single beamformed stream as an equivalent single antenna transmitter. Therefore, for the sake of a lighter notation, the presented model will consider an equivalent Single Input Multiple Output (SIMO) channel.

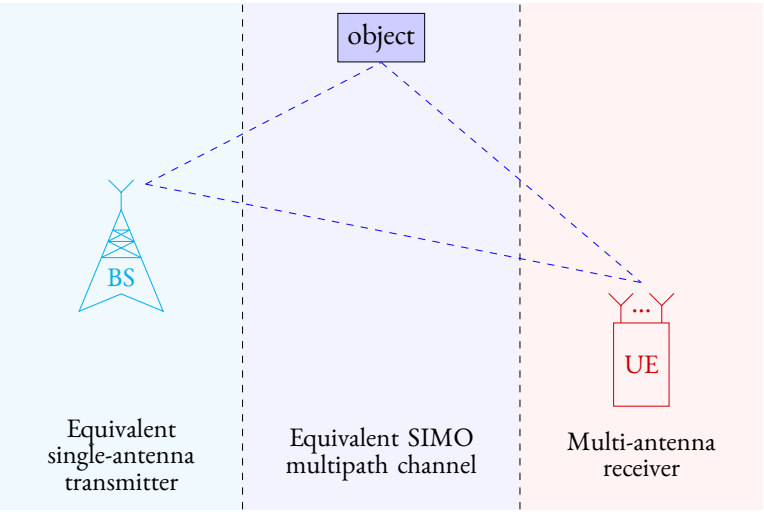

Figure 5.1: System overview.

We assume that the received signal can be decomposed in a sum of K plane waves, each of which has an associated complex amplitude α_k, delay τ_k, and direction $\vec{r}_k$. The number of plane waves should be significantly higher than the 5 typically assumed for mmWave channels [8]. The generic antenna array receiving the signal is depicted in Fig. 5.2.

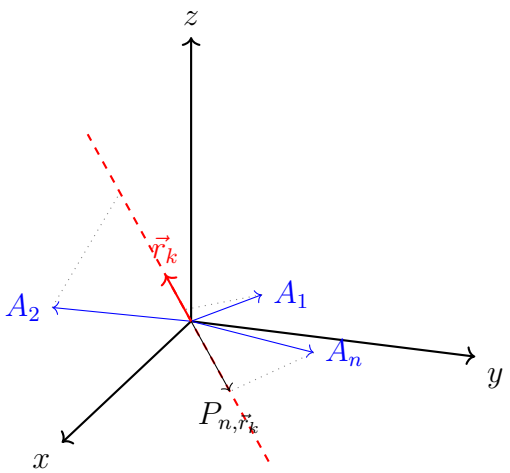

Figure 5.2: Array model.

The antennas are positioned at points A_1 to A_N with respect to the chosen origin of the coordinate system. When a plane wave is impinging on the array in direction $\vec{r}_k$, the projec-

tion of A_n on *span* $\{\vec{r}_k\}$ is denoted by $P_{n,\vec{r}_k}$, and is given by

$$P_{n,\vec{r}_k} = \frac{A_n^T \vec{r}_k}{\vec{r}_k^T \vec{r}_k} \vec{r}_k. \tag{5.1}$$

In Fig. 5.2 we can see that the distance between the projection point and the origin equals the distance traveled by the wavefront before reaching antenna n from the origin. Assuming phase 0 at the origin, and calling λ the wavelength of the signal, this means that the phase observed by antenna n is

$$\phi_{n,\vec{r}_k} = \frac{|P_{n,\vec{r}_k}|}{\lambda} = \frac{A_n^T \vec{r}_k}{(\vec{r}_k^T \vec{r}_k)\lambda} |\vec{r}_k| = \frac{A_n^T \vec{r}_k}{|\vec{r}_k|\lambda}. \tag{5.2}$$

Therefore, neglecting the frequency dependence of $\phi_{n,\vec{r}_k}$, the Channel Impulse Response (CIR) at antenna n is

$$h_n(t) = \sum_{k=1}^{K} \alpha_k e^{j\phi_{n,\vec{r}_k}} \delta(t - \tau_k), \tag{5.3}$$

and the Channel Frequency Response (CFR) is its Fourier transform

$$H_n(f) = \sum_{k=1}^{K} \alpha_k e^{j\phi_{n,\vec{r}_k}} e^{-j2\pi f \tau_k}. \tag{5.4}$$

In some instances, we will assume a Uniform Linear antenna Array (ULA) with N antennas spaced $\frac{\lambda}{2}$, i.e. $A_n = (\frac{n\lambda}{2}, 0, 0)$, and therefore only consider the azimuth incidence angle θ_k. With this assumption, we can write:

$$\phi_{n,\vec{r}_k} = n\pi \cos(\theta_k). \tag{5.5}$$

Therefore, the CIR for antenna n can be written as

$$h_n(t) = \sum_{k=1}^{K} \alpha_k e^{jn\pi \cos(\theta_k)} \delta(t - \tau_k). \tag{5.6}$$

This definition leads to a CFR of

$$H_n(f) = \sum_{k=1}^{K} \alpha_k e^{jn\pi \cos(\theta_k)} e^{-j2\pi f \tau_k}. \tag{5.7}$$

We assume that the system operates with a bandwidth B_A, therefore we have $f \in (-\frac{B_A}{2}, \frac{B_A}{2})$, and that the signal received signal at the antenna is affected by white Gaussian noise with a standard deviation σ_{n_0}. Note that we are ignoring the radiation pattern of the antenna elements, thus making the assumption that they have an omnidirectional radiation pattern. In practice, this is typically not the case. However, if we assume that all the antenna elements are equal and coupling is small, the antenna pattern is going to affect only the value of α_k, thus we can assume that its impact is accounted for in such value. More in detail, if the antenna element has a radiation pattern $P(\vec{r})$, and the k-th received multipath component has a complex amplitude α'_k with an omnidirectional antenna, the observed CIR will be

$$h_n(t) = \sum_{k=1}^{K} P(\vec{r}_k)\alpha'_k e^{j\phi_{n,\vec{r}_k}} \delta(t - \tau_k). \tag{5.8}$$

By redefining the complex amplitude

$$\alpha_k = P(\vec{r}_k)\alpha'_k, \tag{5.9}$$

we have the original definition of the CIR. Based on the findings presented in Chap. 3 we can assume the following properties for the channel parameters:

- The number of components K will have a large value, e.g. in the order of several tens, as compared to the typical value of 5 used in indoor settings [8].
- The directions $\vec{r}_k$ are uniformly distributed in the unit sphere. Due to the consideration stated before about the antenna radiation pattern however, can have that in some directions the received signal is suppressed (i.e. $P(\vec{r}_k) \approx 0$), so we will consider $\vec{r}_k$ to be uniformly distributed within the aperture of the antenna radiation pattern.

For the analog beamforming chain, calling the sampling period of the ADC $T \leq \frac{1}{B_A}$, the transmitted and received signal $x(t)$ and $y_A(t)$ respectively and β_n a complex beamforming coefficient with the amplitude determined by the LNA gain and the phase determined by the phase shifter, the output of the ADC would therefore be of the form

$$y_A(sT) = \sum_{n=1}^{N} \beta_n (h_n * x)(sT), \ s \in \mathbb{Z}, \tag{5.10}$$

and its Discrete Time Fourier Transform (DTFT), assuming that the signal is band-limited

with bandwidth B_A, is

$$Y_A(f) = \sum_{n=1}^{N} \beta_n H_n(f) X(f). \tag{5.11}$$

We further define the beamformed channel

$$H(f) = \sum_{n=1}^{N} \beta_n H_n(f). \tag{5.12}$$

as the channel observed by the signal received by the analog beamforming chain

For the digital beamforming chain, let us define the set of antennas $\mathcal{M} = \{m_1, ..., m_M\}, M \leq N$ for which we are enabling the individual RF chain. At the s-th sample of the ADC, we connect the multiplexer to the RF chain of antenna $m_{(s \bmod M)+1}$. With this assumption, and defining the filter impulse response as $h_{filt}(t)$ and its transfer function as $H_{filt}(f)$, the signal y_D at the ADC output can be expressed as

$$y_D(kT) = (h_{m_{(s \bmod M)+1}} * h_{filt} * x)(sT),\ s \in \mathbb{Z}. \tag{5.13}$$

From this signal, we can extract the individual antenna signals

$$\begin{aligned} y_j(MsT) &= y_D((Ms + j)T) && (5.14)\\ &= (h_{m_{((Ms+j) \bmod M)+1}} * h_{filt} * x)((Ms + j)T) && (5.15)\\ &= (h_{m_{j+1}} * h_{filt} * x)(MsT + jT),\ s \in \mathbb{Z},\ j \in \{0, ..., M-1\} && (5.16) \end{aligned}$$

Notably, the signal $y_j(MsT)$ include all and only the contribution of antenna m_{j+1}, which is sampled regularly with a sampling interval MT. The signal is also delayed by jT, however, we ignore such delay as it can be easily compensated for in the digital domain. By the Nyquist–Shannon sampling theorem we can infer that, to operate correctly, each of the signals should have a bandwidth of $B_D \leq \frac{B_A}{M}$. If the response of the filter is such that

$$(h_{m_{j+1}} * h_{filt} * x)(sT) \tag{5.17}$$

has a bandwidth that satisfies the sampling constraint, we can write the DTFT of the received signal as

$$Y_j(f) = H_{m_{j+1}}(f) H_{filt}(f) X(f) \tag{5.18}$$

For the sake of this work, we also consider only the case of $\mathcal{M} = \{1, ..., N\}$, in other words, the digital beamforming chain will always utilized the maximum rank. While this might seem restrictive, and a variable set $\mathcal{M}$ could provide a benefit in terms of performance, having a fixed $\mathcal{M}$ set, or at least a fixed value of M, is a desirable property from an implementation standpoint. In fact, it allows to implement a single fixed LPF, instead of a tunable LPF which would be needed to change the bandwidth of the digital beamforming. Under this assumption, we can write

$$Y_j(f) = H_{j+1}(f)H_{filt}(f)X(f), \tag{5.19}$$

which is the signal received by antenna $j + 1$. In this case, we note that within the digital beamforming band, the system can individually acquire the signal from each antenna, as would happen in a digital beamforming system, though with a smaller bandwidth.

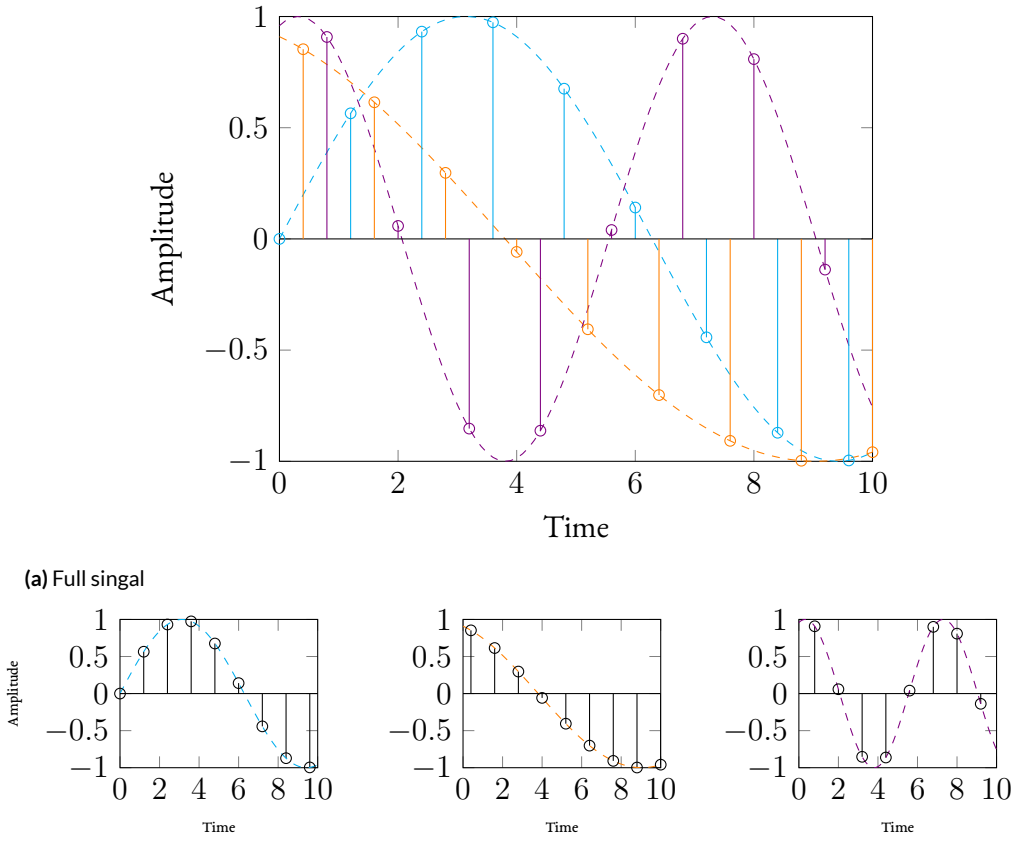

(a) Full singal

(b) Antenna 1.

(c) Antenna 2.

(d) Antenna 3.

Figure 5.3: Example of signal from the digital beamforming part.

Fig. 5.3 shows an example of this process. In particular, in Fig. 5.3a the solid lines represent the analog signal for each antenna after filtering and downconversion, whereas the stems represent the digitalized signal $y_D(kT)$. Note that the color of the stems is just for illustrative purposes, and does not represent different signals. Figs. 5.3b, 5.3c and 5.3d instead represent the downsampled signals $y_0(MsT)$, $y_1(MsT)$ and $y_2(MsT)$ respectively, i.e., the reconstructed signal for each antenna. In the following, we will discuss how this ability can be exploited to improve the communication and sensing performance of the system.

6 Communication

In this chapter, we discuss the potential of the proposed architecture in industrial communications. In particular, we identify the potential use of the architecture in two different ways, that can be used in combination to achieve the best result. The two advantages of the architecture can be summarized in:

1. The digital beamforming chain can be used to actually perform communication with a higher rank and better reliability. In this case, if many UEs are present in the system, different users can perform digital beamforming in different frequencies such that overall most of the communication is performed using this technique. This strategy is investigated in Sec. 6.1.

2. The channel estimate provided by the digital beamforming can be utilized to design the beamforming coefficients used by the analog beamforming chain[31]. This allows for the design of more robust analog beams, as described in detail in Sec. 6.2.

The combination of the two techniques creates a robust and effective system that is particularly suited for industrial communications, which requires high reliability for a large number of UEs.

6.1 Multi-user resource allocation for heterogeneous rank systems

6.1.1 Proportional Fairness Resource Allocation

This section discusses the use of the *heterogeneous mode* for communication in a multi-user setting. We assume that the BS is equipped with a fully digital (or at least high-rank) architecture capable of fully exploiting the rank of the channel. The UEs are equipped with the proposed architecture, which is also capable of exploiting the full channel rank in the digital beamforming part of the bandwidth. More in detail, we assume that there are U users with an architecture with N antennas sharing the total bandwidth B_A. Recalling the resource allocation example shown in Fig. 4.3, we can see that user 1 (in orange) would benefit from digital beamforming in the center RBs in the first four slots, RBs 2 and 3 for the following 4 slots, and in the top RBs for the rest of the time. This is however impractical, as it requires re-configuring the LO of the digital chains every few slots, and such re-configuration can take from tens of μs to some ms [41]. To avoid this issue, we propose that, at the time of connection, the BS informs the UE whether to use the second RF chain for digital beamforming and on which part of the band. Subsequently, at the time of Medium Access Control (MAC) scheduling, the BS preferentially schedules each UE on the frequency where it performs digital beamforming.

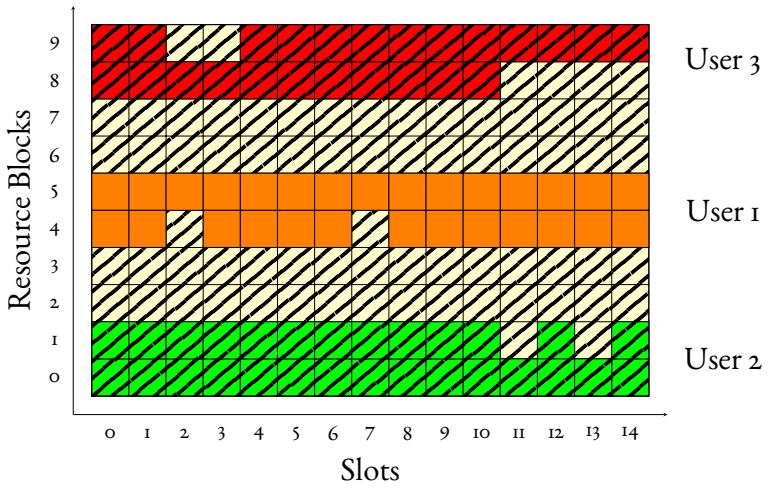

Figure 6.1: Example resource grid in *heterogeneous mode*.

In the example, the BS could instruct user 2 to perform digital beamforming in RBs 0 and 1, user 1 on RBs 4 and 5, and user 3 on RBs 8 and 9. It would then schedule the data according

to the new resource grid in Fig. 6.1. In this case, the data would fit entirely within the band where the UEs perform digital beamforming.

With this allocation, the first RF chain, which operates with analog beamforming, still spends 81.3% of its samples to acquire the area covered with the black strips, but the second RF chain, operating in digital beamforming, only acquires 30 RBs, out of which 28 are intended for that user, thus only wasting 6.7% of the ADC samples. In total, the "efficiency" of the proposed architecture, intended as the fraction of ADC samples on frequency bands carrying data, can be estimated as

$$100 - \frac{81.3 + 6.7}{2} = 56\% \tag{6.1}$$

while that of the classical fully connected hybrid beamforming architecture in the same scenario would be 18.7%, thus confirming that the proposed architecture is significantly more efficient than the classical one when UEs' data are allocated to sub portions of the whole bandwidth using digital beamforming.

Note that the analog RF chain is still necessary to decode control signals. Moreover, the analog RF chain will also be needed in case the data do not fit within the RBs used for digital beamforming, and have to be partially allocated to other RBs. This case is illustrated in Fig. 6.2. Thus, further improving the efficiency by using both RF chain in for digital beamforming is not feasible.

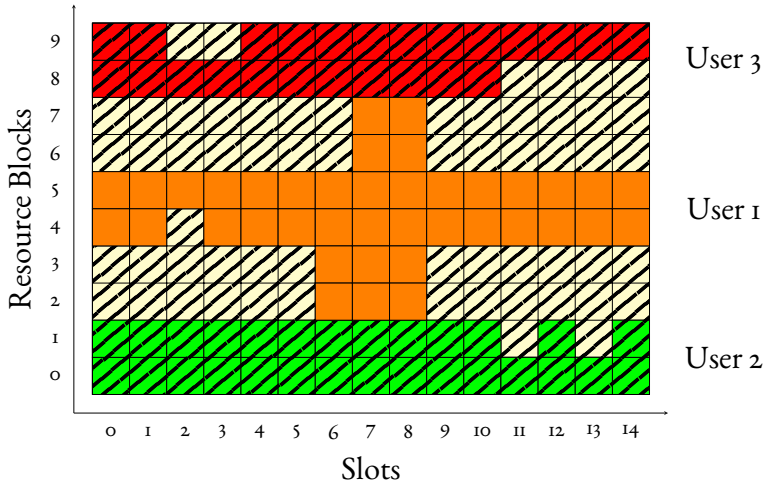

Figure 6.2: Example resource grid in *heterogeneous mode*, where the data does not fit entirely within the MIMO bandwidth.

To analyze the performance of the proposed architecture from the aspect of spectral efficiency, let us assume that all the users are equal, and experience the following:

- A Spectral Efficiency (SE) of C_A bit/s/Hz when using the analog RF chain in *heterogeneous mode*.
- A SE of C_D bit/s/Hz when using the digital RF chain in *heterogeneous mode*.
- A SE of C_H bit/s/Hz when using the *hybrid mode*.

Note that, in the typical situations, we have

$$C_A \leq C_H \leq C_D. \tag{6.2}$$

Assuming that the assignment of the digital beamforming sub-band is performed with minimum overlap, since each user can perform digital beamforming on $\frac{1}{N}B_A$, the fraction of bandwidth that has at least one user with digital beamforming on it is given by:

$$\zeta_D = \min\left(1, \frac{U}{N}\right). \tag{6.3}$$

If all UEs are configured to perform digital beamforming in a part of the band, the maximum average SE achievable in *heterogeneous mode* is therefore

$$C_{max}^{(D)} = (1-\zeta_D)C_A + \zeta_D C_D = C_A + \zeta_D(C_D - C_A). \tag{6.4}$$

Comparing this to the SE of the classical hybrid system (or the proposed system operating in *hybrid mode*), we observe that

$$C_{max}^{(D)} < C_H \iff \zeta_D(C_D - C_A) < C_H - C_A. \tag{6.5}$$

Recalling (6.2), the term $C_D - C_A$ is always positive, therefore we have

$$C_{max}^{(D)} < C_H \iff \zeta_D < \frac{C_H - C_A}{C_D - C_A}. \tag{6.6}$$

Moreover, from (6.2) we also conclude that $(C_D - C_A) \geq (C_H - C_A)$, therefore

$$0 < \frac{C_H - C_A}{C_D - C_A} \leq 1, \tag{6.7}$$

which assures the resulting value of ζ_D is meaningful. We can now replace the definition of ζ_D in the 6.6 to obtain:

$$\frac{U}{N} < \frac{C_H - C_A}{C_D - C_A} \Leftrightarrow U < \frac{N(C_H - C_A)}{C_D - C_A}. \tag{6.8}$$

Under this condition, it is always better to utilize the *hybrid mode*. This also allows us to write the overall maximum achievable average SE as a function of the number of users, which is

$$C_{max} = \begin{cases} C_H & \text{if } U < \frac{N(C_H - C_A)}{C_D - C_A}; \\ C_A + \frac{U}{N}(C_D - C_A) & \text{if } \frac{N(C_H - C_A)}{C_D - C_A} < U < N; \\ C_D & \text{otherwise.} \end{cases} \tag{6.9}$$

This function is illustrated in Fig. 6.3. The cyan line represent the maximum SE achievable when operating in *hybrid mode*, whereas the purple represent the performance of the *Heterogeneous mode*. The solid line represent the value of C_{max}, which is the maximum of the two.

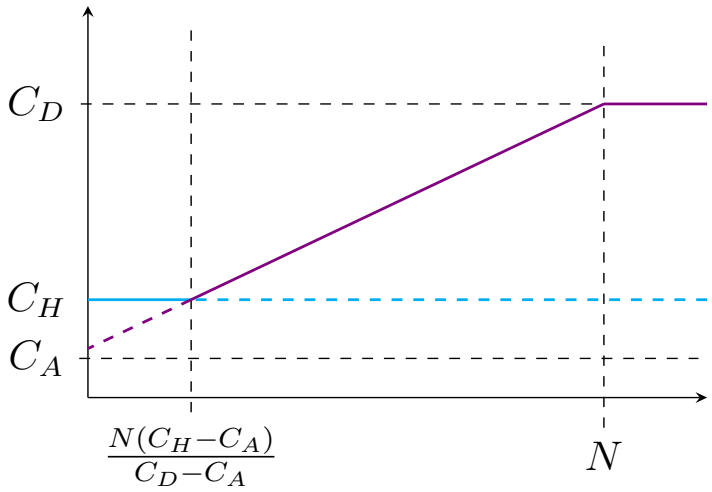

Figure 6.3: Maximum achievable SE as a function of the number of users.

From the figure, we can clearly identify the three regions corresponding to the cases in (6.9). In the first part, the SE of the *hybrid mode* dominates, because there are not enough users to have digital beamforming on a significant portion of the bandwidth when operating in *heterogeneous mode*. In the central region, the number of users is sufficient for the combination of analog and digital beamforming of the *heterogeneous mode* to achieve a bet-

ter SE than the *hybrid mode*. However, the sub-channels used for digital beamforming are not enough to cover the whole available bandwidth, so that $C_{max} < C_D$. Finally, in the third region, all portions of the band are used by at least one UE with digital beamforming, therefore potentially achieving fully digital MIMO across the whole bandwidth. These considerations refer to the maximum achievable rate. However, there is no guarantee that the actual system performance will be close to that bound. In particular, the bound is achievable only if all RBs that can be used for digital beamforming are actually allocated to the users that were given those channels to perform digital beamforming.

To verify that it is possible to exploit such capability in a more realistic scenario, we consider a system implementing Orthogonal Frequency Division Multiplexing Access (OFDMA) with R RBs, and receivers with N antennas. For the sake of simplicity, we assume that a RB lasts 1s and has a bandwidth of 1Hz, thus the capacity of a RB is equal to the spectral efficiency. When operating in *heterogeneous mode*, the second RF chain of user $u \in \{1, ..., U\}$ performs digital beamforming in $\alpha = \left\lfloor \frac{R}{N} \right\rfloor$ RBs, and the allocations to different users are either orthogonal or completely overlapping. In particular, user u performs digital beamforming on RBs $r \in \mathcal{D}_u$, where

$$\mathcal{D}_u = \left\{ \left(u\alpha \bmod R\right), \left(u\alpha + 1 \bmod R\right), ..., \left(u\alpha + \alpha - 1 \bmod R\right) \right\}.$$

We also define the set of users performing digital beamforming in RB r as

$$\mathcal{U}_r = \left\{u : r \in \mathcal{D}_u\right\}. \tag{6.10}$$

For each user, we keep an estimate of its average rate C_u. After each slot, the estimate is updated to $C_u = \gamma C_u + (1 - \gamma)\bar{C}_u$, where $\bar{C}_u$ is the total rate experienced by that user in the slot, that under the considered assumptions above the amount of data transferred in that slot, and $\gamma \in (0, 1)$. The allocation process is depicted in Fig. 6.4. We assume the arrivals, depicted in the figure as orange arrows, happen between time slots. At each slot, we iterate over the RBs in the order shown by the cyan arrows and assign each RB r to the UE u that satisfies the following constraints:

- Its buffer is not empty.
- It has the highest PF weight $W = \frac{C_r}{C_u}$.

In *hybrid mode* we consider $C_r = C_H$, whereas for the *heterogeneous mode* we consider

$$C_r = \begin{cases} C_D, & \text{if } r \in \mathcal{D}_u, \\ C_A, & \text{otherwise.} \end{cases} \tag{6.11}$$

If multiple UEs satisfy such constraint, we choose one at random. When an RB is assigned to a UE, the UE's queue is decreased by C_r.

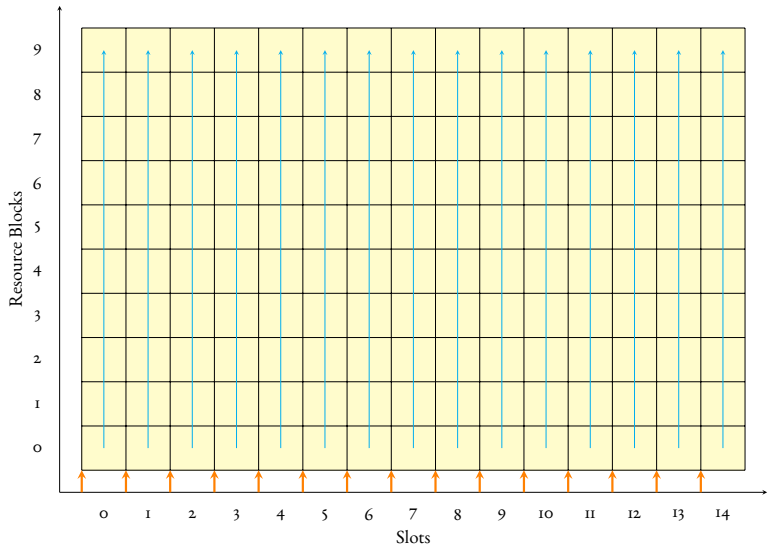

Figure 6.4: Allocation process.

With the described system, RB r can be allocated to analog beamforming if and only if one of the following conditions holds:

C1 At the time of allocation of RB r, none of the UEs which are performing digital beamforming in that RB has data in the buffer, and at least one other UE has data in its buffer.

C2 There is a UE digital beamforming in that RB with data in the buffer, but another UE which is performing analog beamforming in that RB has a higher PF weight.

If all users are equal, and experience the same channel conditions, their average rate C_u should also be similar between different users. Therefore, for a suitable value of γ, condition C2 should not verify. Let us thus approximate the probability of analog beamforming allocation by considering only case C1. In this case, we propose the two following approximations of the achieved throughput.

6.1.2 Empty buffer approximation

We assume each user u, independently of the others, generate a random number v_u of bytes at every slot. Let

$$F_v(a) = \Pr[v_u \leq a] \tag{6.12}$$

be the CDF of v_u, identical for all nodes. Now, let us focus on the set D_u of RBs assigned to certain user u. Let

$$V_u = \sum_{n \in \mathcal{U}_r} v_n \tag{6.13}$$

be the aggregate traffic generated by all the nodes that are pre-assigned at the RBs in D_u. Let $F_{V_u}(\cdot)$ be the CDF of V_u, which can be computed from $F_v(\cdot)$ with standard methods. Then, the number X_u of RBs in D_u which will be assigned to users that can perform digital beamforming is such that

$$X_u \leq \min\left(\alpha, \left\lceil \frac{V_u}{C_D} \right\rceil\right), \tag{6.14}$$

and its expectation can be computed by deriving the Probability Density Function (PDF) of V_u from the finite difference of its CDF and averaging over all possible values h of X_u up to α, to obtain

$$\begin{aligned}\mathbb{E}[X_u] = &\sum_{h=1}^{\alpha-1} h(F_{V_u}(hC_d) - F_{V_u}((h-1)C_D)) \\ &+ \alpha(1 - F_{V_u}((\alpha-1)C_D)).\end{aligned} \tag{6.15}$$

An estimate of the total system throughput can hence be obtained as

$$\tilde{C_1}(U, F_v) = \min\left(G, \sum_{u=1}^{N} \mathbb{E}[X_u]C_D + (\alpha - \mathbb{E}[X_u])C_A\right) \tag{6.16}$$

where G is the overall traffic generated by the U nodes in a slot, $u > U \Rightarrow E[X_u] = 0$, i.e. users that are not in the system do not generate traffic, and the summation is up to N because a user $u' > N$ will share the sub-band with user $u = u' \bmod N$.

6.1.3 Equal buffering probability approximation

Assuming all users, before scheduling RB r, have the same probability of empty buffer $P_b(r)$ (e.g. in case of bursty traffic, where the probability of having empty buffer mostly depends on the time elapsed since the last burst), we can write

$$P_a(r) \approx \left(\prod_{u\in\mathcal{U}_r} P_b(r)\right)\left(1-\prod_{u\notin\mathcal{U}_r} P_b(r)\right) \tag{6.17}$$

$$= P_b^{|\mathcal{U}_r|}(r)(1-P_b^{U-|\mathcal{U}_r|}(r)) \tag{6.18}$$

$$= P_b^{|\mathcal{U}_r|}(r) - P_b^{U}(r). \tag{6.19}$$

We can then estimate the throughput for each RB as

$$\tilde{C}_2(U) = \min\left(G, \sum_{r=1}^{R} P_a(r)C_A + (1-P_a(r))C_D\right) \tag{6.20}$$

Clearly, this approximation requires the knowledge of the values of $P_b(r)$ to be computed. However, this approximation is interesting as it can be bounded in the following way:

Taking the derivative of $P_a(r)$ with respect to P_b we obtain

$$\frac{\partial P_a(r)}{\partial P_b(r)} = \frac{|\mathcal{U}_r|P_b^{|\mathcal{U}_r|}(r) - UP_b^U(r)}{P_b(r)}, \tag{6.21}$$

which has a zero for

$$|\mathcal{U}_r|P_b^{|\mathcal{U}_r|}(r) = UP_b^U(r). \tag{6.22}$$

This equality holds for

$$P_b^\star = \left(\frac{|\mathcal{U}_r|}{U}\right)^{\frac{1}{U-|\mathcal{U}_r|}}. \tag{6.23}$$

Clearly, this is the worst case lower bound for $P_a(r)$. We also note that since $U \geq |\mathcal{U}_r|$ this

is a valid probability. Replacing this in (6.19) we obtain the lower bound:

$$P_a^\star(r) = \left(\frac{|\mathcal{U}_r|}{U}\right)^{\frac{|\mathcal{U}_r|}{U-|\mathcal{U}_r|}} - \left(\frac{|\mathcal{U}_r|}{U}\right)^{\frac{U}{U-|\mathcal{U}_r|}} \tag{6.24}$$

$$= \left(\frac{|\mathcal{U}_r|}{U}\right)^{\frac{|\mathcal{U}_r|}{U\left(1-\frac{|\mathcal{U}_r|}{U}\right)}} - \left(\frac{|\mathcal{U}_r|}{U}\right)^{\frac{U}{|\mathcal{U}_r|\left(\frac{U}{|\mathcal{U}_r|}-1\right)}} . \tag{6.25}$$

Defining $\mathrm{X}(r) = \frac{|\mathcal{U}_r|}{U}$ we obtain:

$$P_a^\star(r) = \mathrm{X}(r)^{\frac{\mathrm{X}(r)}{(1-\mathrm{X}(r))}} - \mathrm{X}(r)^{\frac{1}{\mathrm{X}(r)(\mathrm{X}(r)-1)}} . \tag{6.26}$$

Thus, the bound on the probability of analog beamforming only depends on the ratio of digital beamforming users to all users.

The bound on the approximated average spectral efficiency therefore is

$$\tilde{C}_2^\star(U) = \min\left(G, \sum_{r=1}^{R} P_a^\star(r)C_A + (1 - P_a^\star(r))C_D\right) . \tag{6.27}$$

Fig. 6.5 shows an example of the shape of (6.19) for $U = 100$ and $|\mathcal{U}_r| = 4$. Here we can see that the worst case probability of empty buffer is $P_b^\star = 0.967$ resulting in a probability of analog beamforming allocation of $P_a^\star(r) = 0.84$. We note though that, for a fully loaded system, having such a high probability of empty buffer is not realistic. Moreover, upper bounding the probability of empty buffer will result in a significantly tighter bound for the approximation. For example, if we could bound P_b to be below 0.6, the bound on P_a would drop to only around 0.2.

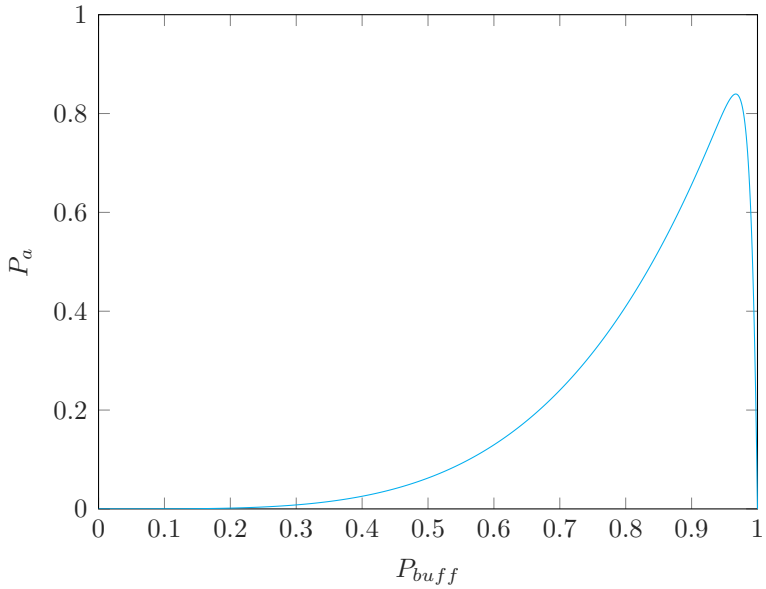

Figure 6.5: P_a as a function of P_b for $|\mathcal{U}_r| = 4$ and $U = 100$.

Based on this observation, we also consider the worst-case analog beamforming probability given $P_b \leq P_b^{max}$, which is

$$P_a^{\star}(P_b^{max}, r) = \begin{cases} P_a^{\star}(r) & \textit{if } P_b^{\star} \leq P_b^{max}(r) \\ (P_b^{max})^{|\mathcal{U}_r|} - (P_b^{max})^{U} & \textit{otherwise} \end{cases}. \tag{6.28}$$

With this we can write a tighter bound for the capacity approximation as

$$\tilde{C}_2^{\star}(U, P_b^{max}) = \min\left(G, \sum_{r=1}^{R} P_a^{\star}(P_b^{max}, r)C_A + (1 - P_a^{\star}(P_b^{max}, r))C_D\right). \tag{6.29}$$

6.1.4 Results

In the following, we present the results for the system described above with $R = 640$ RBs and $N = 32$ antennas. The digital beamforming SE is $C_D = 4$ and the analog beamforming SE is $C_A = 1$. When operating in hybrid beamforming, the SE is $C_H = 1.5$.

We simulate the allocation process for 1000 slots and measure the average rate experienced by the system and the users. We consider an application with a buffer of 1000bits, which generates a random number of bits between 0 and 2Λ at each slot, where Λ is the average

generation rate. With this assumption, $F_{V_u}(a)$ is the CDF of an Irwin-Hall distribution of parameter $n = |D_r|$ computed in $\frac{a}{2\Lambda}$. Fig. 6.6 shows the performance achieved with a data generation rate of $\Lambda = 500$, as well as $\tilde{C}_1(U, F_v)$ and $\tilde{C}_2(U)$ computed for the measured $P_b(r)$. This rate is sufficient to saturate the total capacity with a few users. In particular, Fig. 6.6a shows the aggregate rate of the BS as a function of the number of UEs. Here we can see that below 5 users the hybrid beamforming performs better than the proposed architecture. We note that in this case we have $\frac{N(C_H - C_A)}{C_D - C_A} = 5.33$, therefore the limit of 5 UEs corresponds to what is predicted by the upper bound.

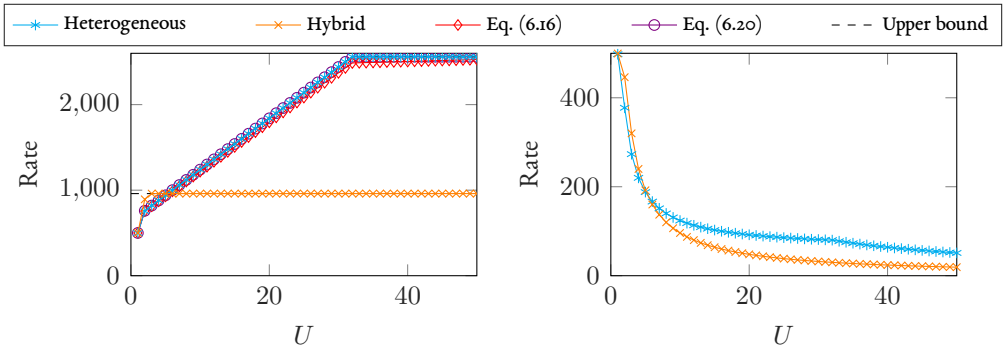

(a) Aggregate rate.

(b) Average user rate.

Figure 6.6: Rate achieved by the user and system for $\Lambda = 500$.

We can also observe that after this point, the digital beamforming curve tightly follows the bound, confirming that a PF scheduler can fully exploit the capabilities of the proposed architecture. Fig. 6.6b shows the average rate observed by each user. Here we can again observe that the hybrid beamforming scheme performs better only with less than 5 users, and the digital beamforming scheme provides a much higher rate for a large number of users. In this case, both approximated models correctly predict the performance of the system. This is expected as, for a large traffic, X_u is likely to be close to α, and therefore it is expected that most RBs are allocated to digital beamforming. Moreover, the probability of empty buffer is independent from the user, as all users are likely to have full buffer at all time due to the high generation rate.

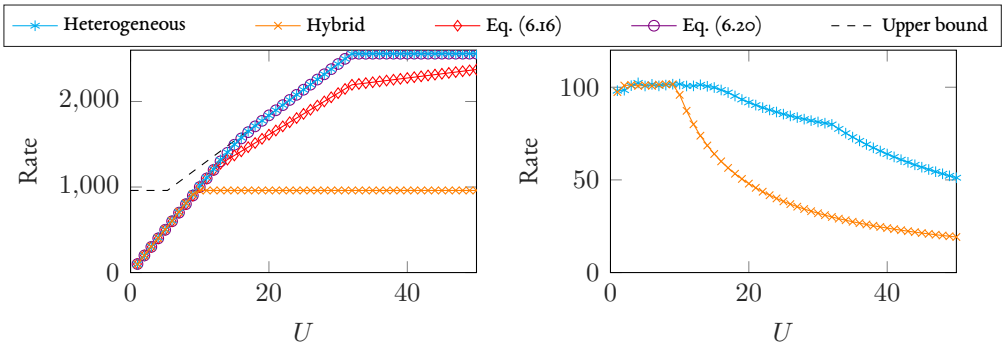

(a) Aggregate rate.

(b) Average user rate.

Figure 6.7: Rate achieved by the user and system for $\Lambda = 100$.

Next, Fig. 6.7 shows the results for an application rate of $\Lambda = 100$bps. In Fig. 6.7a we can see that, in *hybrid mode*, for $U \leq 9$ the rate is limited by the application generation rate. In *heterogeneous mode* instead, this happens for $U \leq 17$, meaning that the proposed scheme is able to support almost twice the number of users at the full rate. In Fig. 6.7b we can also observe that the average rate observed by each user drops more rapidly for the hybrid beamforming scheme. Thus, the hybrid beamforming system can support only 10 UEs with 90% of the required rate, whereas the proposed scheme can support up to 21 UEs for the same required rate. Here we can observe that the empty buffer approximation slightly underestimates the throughput, as in this case the assumption of empty buffer at the beginning of the slot is unrealistic, whereas the equal buffer probability approximation correctly predicts the performance.

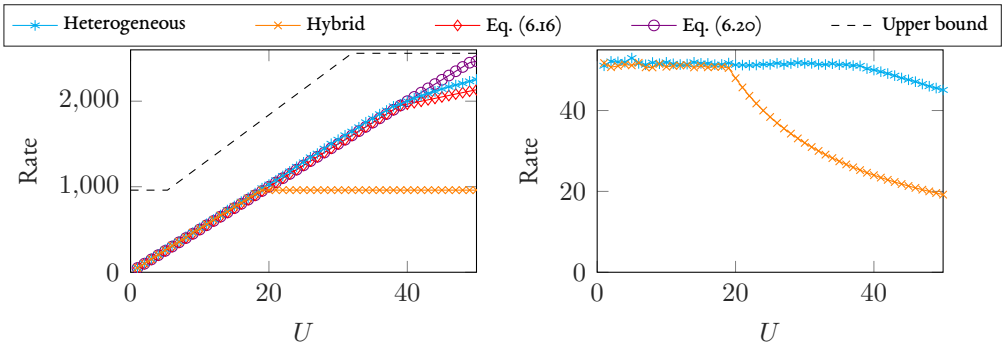

(a) Aggregate rate.

(b) Average user rate.

Figure 6.8: Rate achieved by the user and system for $\Lambda = 50$.

Fig. 6.8 we can observe the results for an application rate of $\Lambda = 50$bps. From Fig. 6.8a it

can be observed that the maximum capacity C_{max} achievable with *heterogeneous mode* is not saturated even at 50 UEs, whereas the hybrid beamforming capacity is saturated at $U = 19$. Despite not saturating C_{max}, in Fig. 6.8b we can observe that for $U \geq 38$ the system is unable to support the aggregate generation rate rate of the UEs. This suggests that in this case, the scheduler is unable to fully exploit the digital beamforming, and end up allocating some RBs to analog beamforming. This is due to the fact that with a large number of users that have a low generation rate, thus the situation where some UEs are allocated to use analog beamforming because there are no digital beamforming UEs with data in their buffer (condition C2) becomes more common. In this situation the empty buffer model is again close to the simulated value, as the empty buffer assumption is more realistic due to the low traffic generated by the individual UEs. The equal buffer probability approximation, instead, overestimates the throughput. This is due to the fact that the empty buffer probability is higher for analog beamforming users when allocating the last RBs, as they are likely to have flushed their buffer earlier, in their assigned digital beamforming RBs.

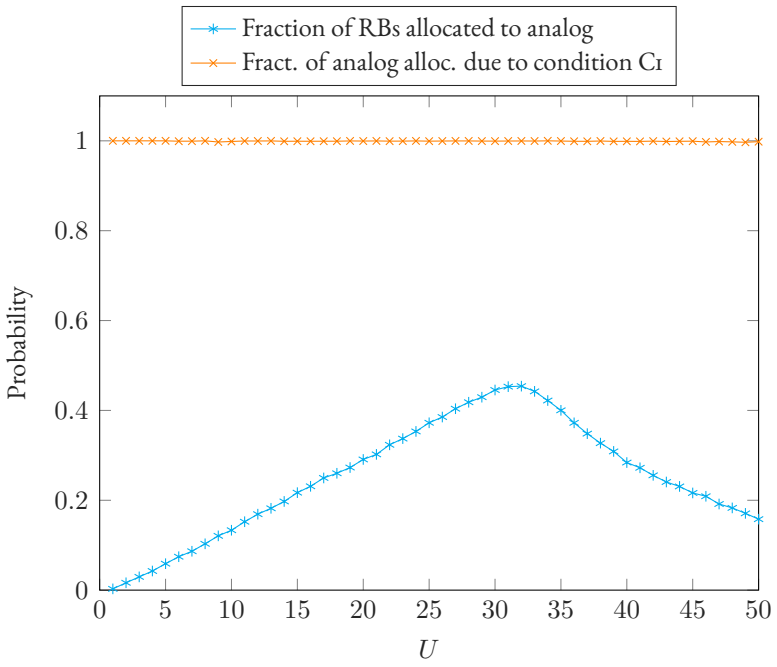

Figure 6.9: Fraction of RBs allocated to analog beamforming and reason of the allocation for $\Lambda = 50$.

Fig. 6.9 shows the fraction of RBs allocated to users performing analog beamforming in cyan. It also shows in orange the percentage of such allocations that are done because there is no digital beamforming UE with data in the buffer (condition C1), rather than because the

PF weight of the analog beamforming UE is higher (condition C2). We recall that, to develop both proposed model, we assumed that all analog allocations where caused by condition C1. Thus, the orange curve being very close to 1 validate such assumption.

Fig. 6.10 shows the average fraction of unused RBs as a function of U for $\Lambda = 50$. Here we can observe that for $U \geq 19$ the hybrid beamforming system needs to use all the available resource elements. This is consistent with the fact that we observe an average rate drop for the UEs after that point. In contrast, at $U = 19$ the proposed method uses only 59% of the RBs, thus saving 41% of the transmission power.

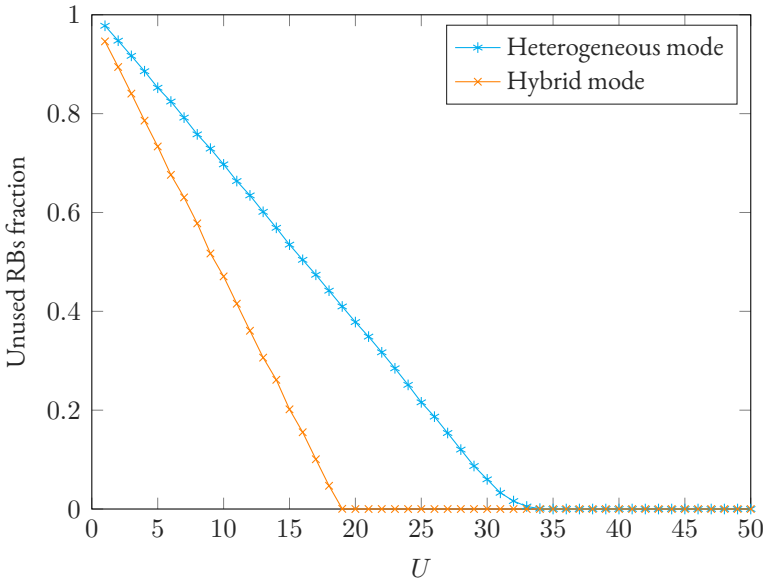

Figure 6.10: Fraction of unused RBs for $\Lambda = 50$.

Finally, Fig. 6.11 shows the values of the achievable rate for approximation's bound $R\tilde{C}_2^{\star}(U, P_b^{max})$ for different values of P_b^{max}, as well as the maximum achievable rate RC_{max} and the hybrid beamforming rate RC_H.

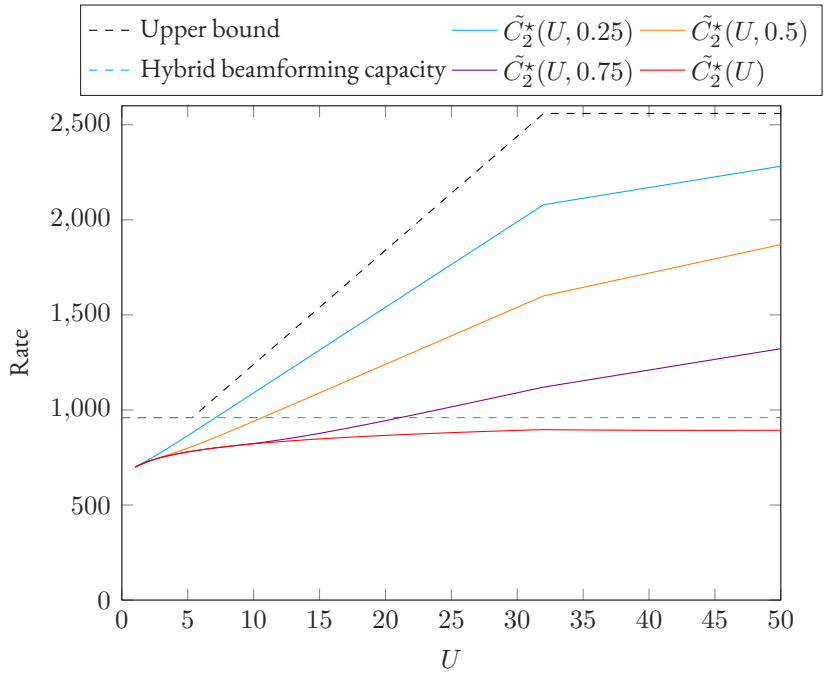

Figure 6.11: Rate bounds for different values of P_b^{max}.

Here we can see that for high values of P_b^{max} the bound is quite loose, as was also shown in Fig. 6.5. In contrast, for low values of P_B^{max}, which are more realistic in a heavily loaded system, the lower bound gets very close to the upper bound. This guarantees that, in the cases where this approximation is accurate, the digital beamforming potential of the system can be exploited through the band. For example, considering a system with $P_B^{max} = 0.5$, the proposed system is guaranteed to outperform the classical hybrid beamforming with as few as $U = 12$ users.

6.2 Robust analog beamforming

In this section, we investigate how the *hybrid mode* enables a more robust beam design for the analog beamforming part of the architecture. In particular, we study the use of MRC, a well-known technique to combine signals received by a multi-antenna system dating back to 1954 [42]. The classical derivation of MRC comes from the SNR maximization problem in narrowband scenarios [43]. Modern communication systems, however, are typically wideband and, and are thus not capable of fully exploiting the linear gain of MRC. Nevertheless, MRC turns out to be robust and effective also in such systems, and understanding the reason for this unexpectedly good performance is not straightforward.

In this section, we investigate this aspect by analyzing the geometric features of the Array Factor (AF) of the beam with MRC coefficients. Moreover, we analyze the performance of MRC outside its design coherence bandwidth, evaluating the SNR that can be obtained by an analog beamforming wideband system with such a beam. Although over the years many analysis [44, 45, 46] and variants [47, 48] of MRC have been proposed, to the best of our knowledge, these characteristics of the method have never beed investigated. The main contributions of this section can be hence summarized as follows:

- We show that, when the channel is a linear combination of plane waves, the beam with the MRC coefficients can be decomposed in a linear combination of beams, each pointed towards one of the plane waves;
- We provide a statistical characterization of the number of beam components that are actually active (i.e., are weighted with a relevant coefficient in the linear combination);
- We compute the average SNR achieved by the beam in a wideband setting, and compare it with that achieved by a single-direction beam pointed in the best direction;
- We provide a numerical evaluation of the distribution of the achieved SNR when one component of the channel is blocked, and compare it to the single-direction beam solution, to demonstrate the robustness of MRC.
- We provide a numerical evaluation of the Signal to Interference Ratio (SIR) experienced observed with classical pencil beams and with MRC, as well as its distribution.
- We provide a numerical evaluation of the impact of noisy channel estimation on the MRC beam.

We note that the design of the MRC beam is made possible by the digital beamforming part of the hardware architecture, which can provide per-antenna channel estimates. It also has negligible computational complexity, as it only involves the computation of the complex conjugate of the channel coefficients, and it can be performed without any beam training procedure. Given its low-complexity implementation, its use in modern wideband analog beamforming systems could therefore be considered as an alternative to the standard single-direction beam.

More in detail, we assume the following beamforming strategy. From the signals $Y_j(f)$ received by the digital beamforming RF chain we estimate for each antenna the channel coefficient $H_n(0)$ for the carrier frequency. For the sake of analysis, we will now assume that the estimate is perfect, while the impact of a noisy estimate will be evaluated numerically in the following. With this knowledge, analog beamforming is performed according to MRC for the center of the frequency band, i.e., the beamforming coefficient for antenna n is*

$$\beta_n = \frac{1}{N} H_n^*(0) = \frac{1}{N} \sum_{m=1}^{K} \alpha_m^* e^{-j\phi_{n,\vec{r}_m}} . \tag{6.30}$$

With these assumptions, we study the beam geometry and performance in the following sections.

*This could be normalized to have a unitary beamforming vector, however, this normalization does not impact the conclusion of this work and is therefore unnecessarily cumbersome.

6.2.1 Beam Geometry

The array factor in direction $\vec{r}$, with $|\vec{r}| = 1$, is

$$F(\vec{r}) = \sum_{n=1}^{N} \beta_n e^{j\phi_{n,\vec{r}}} \tag{6.31}$$

$$= \frac{1}{N} \sum_{n=1}^{N} \left(\sum_{k=1}^{K} \alpha_k^* e^{-j\phi_{n,\vec{r}_k}} \right) e^{j\phi_{n,\vec{r}}}. \tag{6.32}$$

By rearranging the sums, we can highlight the contribution of each multipath component to the array factor, obtaining the expression:

$$F(\vec{r}) = \sum_{k=1}^{K} \alpha_k^* \frac{1}{N} \left(\sum_{n=1}^{N} e^{-j\phi_{n,\vec{r}_k}} e^{j\phi_{n,\vec{r}}} \right) = \sum_{k=1}^{K} \alpha_k^* F_k(\vec{r}) \tag{6.33}$$

where

$$F_k(\vec{r}) = \frac{1}{N} \sum_{n=1}^{N} e^{-j\phi_{n,\vec{r}_k}} e^{j\phi_{n,\vec{r}}} \tag{6.34}$$

denotes the array factor component associated to the multipath component k. Clearly, it holds $F_k(\vec{r}) \leq 1$ and

$$F_k(\vec{r}_k) = \frac{1}{N} \sum_{n=1}^{N} e^{-j\phi_{n,\vec{r}_k}} e^{j\phi_{n,\vec{r}_k}} = \frac{1}{N} \sum_{n=1}^{N} 1 = 1. \tag{6.35}$$

Therefore, we can conclude that each array factor component has a global maximum in the direction of the plane it is associated with. Let us now determine the gain observed by a generic component. For the generic direction $\vec{r}_h$, we obtain a total gain:

$$F(\vec{r}_h) = \alpha_h^* + \frac{1}{N} \sum_{\substack{k=1 \\ k \neq h}}^{K} \alpha_k^* \left(\sum_{n=1}^{N} e^{-j\phi_{n,\vec{r}_k}} e^{j\phi_{n,\vec{r}_h}} \right). \tag{6.36}$$

If the multipath components are few and spread apart compared to the beam component's beamwidth (i.e., the gain of the beam components rapidly decreases moving away from the maximum, and is already much smaller than the peak at the direction of the next component), and $|\alpha_h|$ is comparable to the amplitude of the other components, we have that the second

term of the sum is negligible, therefore $F(\vec{r}_h) \approx \alpha_h^*$. In other words, the MRC between the antennas is equivalent to the MRC between the components. This is exemplified in Fig. 6.12, where we can observe the 3D radiation pattern of an 8×8 Uniform Rectangular antenna Array (URA) with a channel that has 3 multipath components with the properties listed in Tab. 6.1.

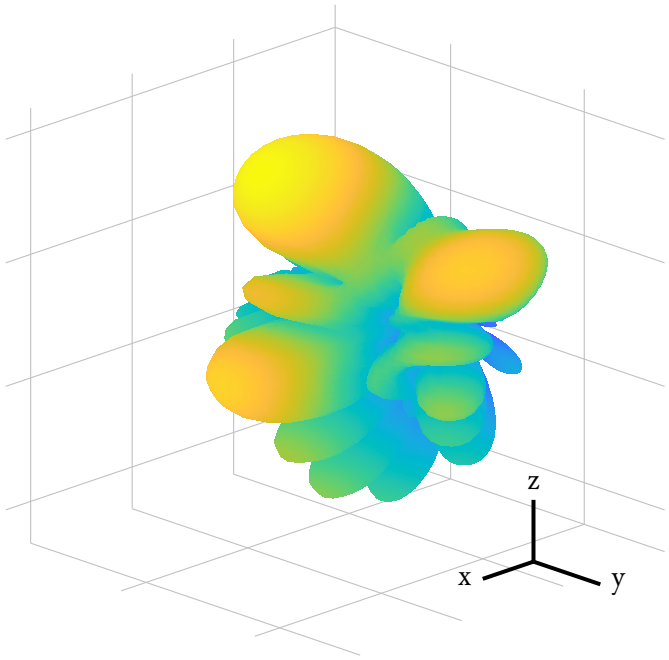

Figure 6.12: Example MRC radiation pattern.

Table 6.1: Example channel parameters

k	$\vec{r}_k$	α_k
1	$(-1, 0, 0)$	0.5
2	$\left(\frac{1}{\sqrt{3}}, -\frac{1}{\sqrt{3}}, -\frac{1}{\sqrt{3}}\right)$	1
3	$\left(-\frac{1}{\sqrt{2}}, 0, \frac{1}{\sqrt{2}}\right)$	1.5

We can clearly see how the pattern has multiple main lobes in the directions of the multipath components, as predicted by the theory.

On the other hand, if the amplitude of the h-th component is small, the second term in (6.36) becomes relevant. In this case, the h-th component might bring a negligible contribu-

tion to the total received power. For this reason, we define a condition of effectiveness for the component according to which component h is effective if

$$|\alpha_h^*| \geq |X_h|, \tag{6.37}$$

where

$$X_h = \sum_{\substack{k=1 \\ k \neq h}}^{K} \frac{1}{N} \alpha_k^* \left(\sum_{n=1}^{N} e^{-j\phi_{n,\vec{r}_k}} e^{j\phi_{n,\vec{r}_1}} \right). \tag{6.38}$$

To understand this definition, let us consider the impact of amplitude variations of the h-th multipath component on the overall channel. In case the component is effective, we have that

$$\frac{\partial H(f)}{\partial \alpha_h} = \frac{\partial F(\vec{k}_h)\alpha_h}{\partial \alpha_h} \approx \frac{\partial |\alpha_h|^2}{\partial \alpha_h}. \tag{6.39}$$

In contrast, in the ineffective case we have

$$\frac{\partial H(f)}{\partial \alpha_h} = \frac{\partial F(\vec{k}_h)\alpha_h}{\partial \alpha_h} \approx \frac{\partial X_h \alpha_h}{\partial \alpha_h}. \tag{6.40}$$

Clearly, this shows how changing the amplitude of an effective component has a quadratic effect on the channel, whereas an ineffective component will have only a linear impact. Moreover, the impact of an ineffective component is scaled by X_h, that, when the component is ineffective, is by definition smaller than the amplitude of the effective components. Therefore, a disruption of an ineffective component, such as a blockage, will affect the channel negligibly. The rationale behind this definition is also exemplified in Fig. 6.13. Here we can see the radiation pattern shown before in Fig. 6.12 with the addition of one multipath component in the direction $\vec{r}_4 = \left(-\frac{1}{\sqrt{3}}, -\sqrt{\frac{2}{3}}, 0\right)$. We note that the value of the right-hand side term in (6.37) in this case is $X_4 = 0.32$. In Fig. 6.13a shows the new pattern for $\alpha_4 = 0.15$, i.e. with the new component being ineffective. Clearly, we cannot observe any change in the main lobes in this case. In contrast, Fig. 6.13b shows the pattern for $\alpha_4 = 0.6$. In this case the component is effective, and we can clearly see a new main lobe in that direction.

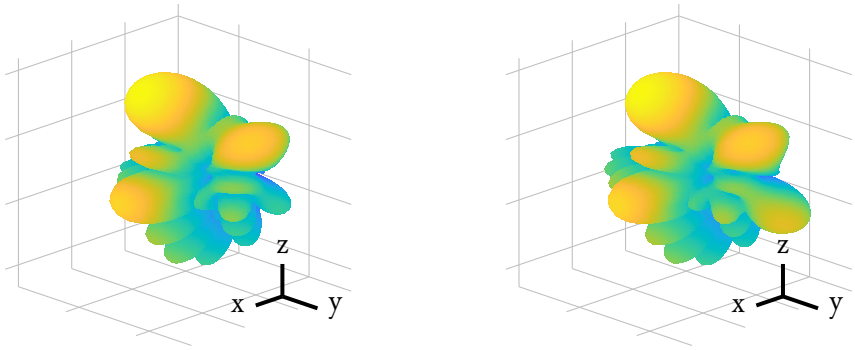

(a) Ineffective component.

(b) Effective component.

Figure 6.13: Change in radiation pattern induced by an effective and an ineffective component.

To characterize the probability of effectiveness of the components, we consider the following assumptions:

1. The values of α_k are distributed according to a complex normal Random Variable (r.v.) $\mathcal{CN}(0,1)$. This assumption is justified by the channel properties observed in Chap. 3;

2. $\vec{r}_k$ can have an arbitrary distribution. However, considering the results observed in Chap. 3, we can assume the directions to be uniformly distributed within the antenna elements aperture;

3. all α_k and $\vec{r}_k$ are mutually uncorrelated, i.e. the amplitude and direction of each component do not depend on the amplitude and direction of the other components, and the amplitude of a component does not depend on its own direction.

With these assumptions, we study the random variable

$$X = X_1 = \sum_{k=2}^{K} \frac{1}{N} \alpha_k^* \left(\sum_{n=1}^{N} e^{-j\phi_{n,\vec{r}_k}} e^{j\phi_{n,\vec{r}_1}} \right) \tag{6.41}$$

where, without loss of generality, we consider $h = 1$. Clearly, as each term of the sum is multiplied by α_k^*, which is zero mean, each term of the sum is itself zero mean, therefore we have

$$\mathbb{E}[X] = 0. \tag{6.42}$$

Since $\{\alpha_k\}$ has unitary variance by assumption, and amplitudes and angles are independent, by defining $\bar{K} = K - 1$ we have:

$$Var\left[X\right] = \mathbb{E}\left[\left|\sum_{k=2}^{K} \alpha_k^* \left(\frac{1}{N}\sum_{n=1}^{N} e^{-j\phi_{n,\vec{r}_k}} e^{j\phi_{n,\vec{r}}}\right)\right|^2\right] \tag{6.43}$$

$$= \mathbb{E}\left[\sum_{k=2}^{K} \left|\alpha_k \left(\frac{1}{N}\sum_{n=1}^{N} e^{-j\phi_{n,\vec{r}_k}} e^{j\phi_{n,\vec{r}_1}}\right)\right|^2\right] \tag{6.44}$$

$$= \bar{K}\mathbb{E}\left[\left|\left(\frac{1}{N}\sum_{n=1}^{N} e^{-j\phi_{n,\vec{r}_k}} e^{j\phi_{n,\vec{r}_1}}\right)\right|^2\right] \tag{6.45}$$

$$= \bar{K}a^2; \tag{6.46}$$

where

$$a = \mathbb{E}\left[\left|\left(\frac{1}{N}\sum_{n=1}^{N} e^{-j\phi_{n,\vec{r}_k}} e^{j\phi_{n,\vec{r}_1}}\right)\right|^2\right] \tag{6.47}$$

is the only parameter that depends on the array geometry, and therefore we call it the *array parameter*. This value can be computed numerically for the array of interest through, e.g., Monte Carlo simulation. We can then approximate X by a zero mean complex Gaussian r.v. with variance $\bar{K}a^2$. Such approximation is suggested by the law of large numbers,but it is not necessarily verified in practice. Nonetheless, this approximation is mathematically convenient, and it determines a relatively small gap with physically-accurate simulations, as we will show in the results section. With this approximation, the conditional probability of ineffectiveness given α_1 is the probability that $|\alpha_1|$ is smaller than $|X|$, which is a Rayleigh r.v. of parameter $\sqrt{\frac{\bar{K}}{2}}a$. Therefore we have

$$P_{ineff}(z) \triangleq P\left[|X| \geq |\alpha_1| \,\middle|\, |\alpha_1| = z\right] = e^{-\frac{z^2}{\bar{K}a^2}}. \tag{6.48}$$

The overall P_{ineff} can be obtained by integrating $P_{ineff}(z)$ over the distribution of $|\alpha_1|$,

which is Rayleigh with parameter $\frac{1}{\sqrt{2}}$. This can be expressed as

$$P_{ineff} = \int_0^\infty P\left[|\alpha_1| = z\right] P_{ineff}(z) dz \tag{6.49}$$

$$= \int_0^\infty 2ze^{-z^2} e^{-\frac{z^2}{\bar{K}a^2}} dz \tag{6.50}$$

$$= \frac{\bar{K}a^2}{1+\bar{K}a^2}. \tag{6.51}$$

From this expression, we can also compute the median number of effective components as

$$E = K\left(1 - P_{ineff}\right) = K\left(1 - \frac{\bar{K}a^2}{1+\bar{K}a^2}\right) = \frac{K}{1+\bar{K}a^2} = \frac{K}{1+Ka^2-a^2}. \tag{6.52}$$

Its derivative with respect to K is

$$\frac{\partial E}{\partial K} = \frac{1-a^2}{(a^2\bar{K}+1)^2}. \tag{6.53}$$

For $a^2 < 1$, which is a usual condition, we note that the median number of effective components is monotonically increasing, therefore we can compute the maximum E as:

$$E_\infty = \lim_{K\to\infty} K\left(1 - \frac{\bar{K}a^2}{1+\bar{K}a^2}\right) = \frac{1}{a^2}. \tag{6.54}$$

Thus, the arrays with smaller array factors can exploit more multipath components.

6.2.2 Wideband behaviour

When the MRC beam is used in an analog beamforming wideband system, the phases of the channel coefficients are frequency dependent, therefore the classical SNR formulation does not apply outside one coherence bandwidth from the carrier frequency. Instead, the CFR outside of the coherence bandwidth can be expressed as

$$H(f) = \sum_{k=1}^{K} |\alpha_k|^2 e^{j2\pi f\tau_k} + \sum_{k=1}^{K} \alpha_k \sum_{k'\neq k} e^{j2\pi f(\tau_k-\tau_{k'})} \frac{1}{N} \alpha_{k'}^* \left(\sum_{n=1}^{N} e^{-j\phi_{n,\vec{r}_{k'}}} e^{j\phi_{n,\vec{r}_k}}\right), \tag{6.55}$$

Where the first summation accounts for the contribution of the K multipath components received by the corresponding beam components, while the other term is the aggregate contribution of the multipath components not aligned with the beam components. More in detail, in the first term we see that each of the multipath components contribute with an amplitude $|\alpha_k|^2$, as it has an amplitude α_k multiplied by a gain α_k^*, and a phase that linearly scales with frequency. In the second term instead, the amplitude depends linearly on $|\alpha_k|$, but the gain, summarized in the inner summation, only depends on the other components. We note that such gain is similar to X_k, with the addition of the term $e^{j2\pi f(\tau_k - \tau_{k'})}$ to account for the frequency selectivity introduced by the delay difference between the components. Considering a frequency well outside the coherence bandwidth of the channel, we can assume that the phases $2\pi f(\tau_k - \tau_{k'})$ are uniformly distributed and independent. With this assumption, the expected channel power gain is

$$\mathbb{E}\left[|H(f)|^2\right] = \sum_{k=1}^{K} \mathbb{E}\left[|\alpha_k|^4\right] + \sum_{k=1}^{K} \mathbb{E}\left[|\alpha_k|^2 \left| \sum_{k' \neq k} \frac{1}{N} \alpha_{k'}^* \left(\sum_{n=1}^{N} e^{-j\phi_{n,\vec{r}_{k'}}} e^{j\phi_{n,\vec{r}_k}} \right) \right|^2 \right]. \tag{6.56}$$

Recalling the independence between paths and the definition of the *array parameter* a in (6.47), we can rewrite (6.56) as

$$\mathbb{E}\left[|H(f)|^2\right] = K\left(\mathbb{E}\left[|\alpha_k|^4\right] + \mathbb{E}\left[|\alpha_k|^2\right] \bar{K} a^2\right). \tag{6.57}$$

Using the assumption that $\alpha_k \sim \mathcal{CN}(0,1)$, the expectations $\mathbb{E}\left[|\alpha_k|^4\right]$ and $\mathbb{E}\left[|\alpha_k|^2\right]$ are the 4^{th} and 2^{nd} moment of a Rayleigh r.v. with parameter $\frac{1}{\sqrt{2}}$, which are 2 and 1, respectively. Thus, the final expression for the gain is

$$\mathbb{E}\left[|H(f)|^2\right] = K\left(2 + \bar{K} a^2\right). \tag{6.58}$$

The noise is a linear combination of Gaussian r.v.s with coefficients β_n, therefore the variance is

$$\sigma_n^2 = \sigma_{n_0}^2 \sum_{n=1}^{N} |\beta_n|^2, \tag{6.59}$$

with expected value

$$\mathbb{E}\left[\sigma_n^2\right] = N \sigma_{n_0}^2 \mathbb{E}\left[|\beta_n^2|\right]. \tag{6.60}$$

The right-most expectation in (6.60) can be computed as

$$\mathbb{E}\left[|\beta_n|^2\right] = \mathbb{E}\left[\left|\frac{1}{N}\sum_{k=1}^{K}\alpha_k^* e^{-j\phi_{n,\vec{r}_k}}\right|^2\right] = \frac{1}{N^2}\sum_{k=1}^{K}\mathbb{E}\left[|\alpha_k|^2\right] = \frac{K}{N^2}, \tag{6.61}$$

so that the expected noise variance is

$$\mathbb{E}\left[\sigma_n^2\right] = N\sigma_{n_0}^2\frac{K}{N^2} = \frac{K}{N}\sigma_{n_0}^2. \tag{6.62}$$

Based on these results, we can compute the average-signal-to-average-noise-ratio as

$$\Gamma = \frac{\mathbb{E}\left[|H(f)|^2\right]}{\mathbb{E}\left[\sigma_n^2\right]} = K\left(2+\bar{K}a^2\right)\frac{N}{K\sigma_{n_0}^2} \tag{6.63}$$

$$= \frac{N}{\sigma_{n_0}^2}\left(2+\bar{K}a^2\right). \tag{6.64}$$

Note that, despite the function looks linear in N, this is not guaranteed. In fact, the *array parameter* a also depends in a complicated manner on the array size and geometry. Moreover, for $K = 1$, (6.64) gives a $2N$ gain compared to the SNR observed by a single element. This is actually an artifact of approximating the SNR using the average-signal-to-average-noise-ratio. In this case in fact, the MRC corresponds to the classical beamforming, which is known to have an SNR gain of N. We therefore note that the proposed approximation has a 3dB error for $K = 1$. As a comparison, we compute the gain obtained with a single beam pointed towards the largest component that, without loss of generality, we assume to be the first. Therefore, we set the beam coefficients to

$$\beta_n^{(Sing)} = \frac{1}{N}e^{-j\phi_{n,\vec{r}_1}}. \tag{6.65}$$

We call the channel observed after beamforming with these coefficients $H^{(Sing)}(f)$.

With this assumption, and again using the definition of *array parameter*, the channel power gain can be written as

$$\mathbb{E}\left[|H^{(Sing)}(f)|^2\right] = \mathbb{E}\left[|\alpha_1|^2\right] + \sum_{k=2}^{K}a^2\mathbb{E}\left[|\alpha_k|^2\right]. \tag{6.66}$$

Note that, under the assumption that α_1 is the largest component, its statistical distribution

changes. In fact, if we assume that a generic α_k has exponentially distributed power with parameter 1 (which is a direct consequence of the Gaussian distribution of α_k), the CDF of $|\alpha_1|^2$ is given by

$$P\left[|\alpha_1|^2 < x\right] = \left(1 - e^{-x}\right)^K, \tag{6.67}$$

and its PDF is hence

$$\frac{\partial}{\partial x}\left(1 - e^{-x}\right)^K = Ke^{-x}\left(1 - e^{-x}\right)^{K-1}. \tag{6.68}$$

Finally, its expected value is

$$\int_0^\infty Kxe^{-x}\left(1 - e^{-x}\right)^{K-1} dx = H_K \approx \log(K) + \gamma, \tag{6.69}$$

where H_K is the K-th harmonic number and γ is the Euler's constant. The statistics of α_k for $k \neq 1$ would also change, but we neglect this aspect, thus obtaining

$$\mathbb{E}\left[|H^{(Sing)}(f)|^2\right] \approx \log(K) + \gamma + \bar{K}a^2. \tag{6.70}$$

The expected noise power will be simply

$$\mathbb{E}\left[\sigma_n^2\right] = \frac{\sigma_{n_0}^2}{N}, \tag{6.71}$$

and the SNR is

$$\Gamma^{(Sing)} = \frac{\mathbb{E}\left[|H(f)|^2\right]}{\mathbb{E}\left[\sigma_n^2\right]} = \frac{N(\log(K) + \gamma + \bar{K}a^2)}{\sigma_{n_0}^2}. \tag{6.72}$$

The ratio between the SNR with a single-direction and with MRC is hence

$$\frac{\Gamma^{(Sing)}}{\Gamma} = \frac{N(\log(K) + \gamma + \bar{K}a^2)}{\sigma_{n_0}^2}\frac{\sigma_{n_0}^2}{N\left(2 + \bar{K}a^2\right)} \tag{6.73}$$

$$= \frac{(\log(K) + \gamma + \bar{K}a^2)}{\left(2 + \bar{K}a^2\right)}. \tag{6.74}$$

Recalling the channel characteristics discussed in Chap. 3, we are interested in the case

where K is large. We therefore consider

$$\lim_{K\to\infty} \frac{(\log(K) + \gamma + \bar{K}a^2)}{\left(2 + \bar{K}a^2\right)} = 1. \tag{6.75}$$

Thus, for a channel with rich multipath like the one observed in industrial environments, the two methods show the same gain.

6.2.3 Performance evaluation

In Tab. 6.2 are listed the values of the *array parameter* a for various Uniform Linear antenna Arrays (ULAs) and uniformly distributed angle of arrival within a fixed Field of View (FoV). As expected, the value decreases with the number of antennas, since the probability of the array having a large gain in a random direction decreases. It also decreases with the FoV, as with a smaller FoV there is less space covered by the sidelobes. Tab. 6.3 shows the corresponding maximum number of effective components $\frac{1}{a^2}$. Here we can see that even with a modest size array we can achieve a remarkable spatial diversity. Clearly the results provided in Tab. 6.3 are limit values, and are not achievable in practical context. Therefore, we further study the number of components and ineffectiveness probability for practical values of K.

Table 6.2: *Array parameters* for some ULAs

FoV	180°	120°	60°
ULA Elements	a		
2	0.55	0.50	0.69
4	0.30	0.26	0.40
8	0.17	0.14	0.22
16	0.09	0.07	0.12
32	0.05	0.04	0.06
64	0.03	0.02	0.03

Table 6.3: *Array parameters* for some ULAs

FoV	180°	120°	60°
ULA Elements	E_∞		
2	3.3	4	2.1
4	11.1	14.8	6.3
8	34.6	51	20.6
16	123.5	204	69.4
32	400	625	277.8
64	1111	2500	1111

Fig. 6.14a shows the probability of ineffectiveness of a component for different ULAs as a function of the total number of multipath components. The lines represent the theoretical value according to (6.51), whereas the marks represent the value estimated numerically over 1000 realizations. Similarly, Fig. 6.14b shows the median number of effective components E. The lines represent the theoretical value and the marks represent the numerical estimations. As we can see, in both cases the theory follows the numerical estimation quite closely, with a small gap caused by the Gaussian approximation of X. We also notice that even with a modest array of only 8 antennas we can exploit as many as 4 components in a channel that has a total of only 6.

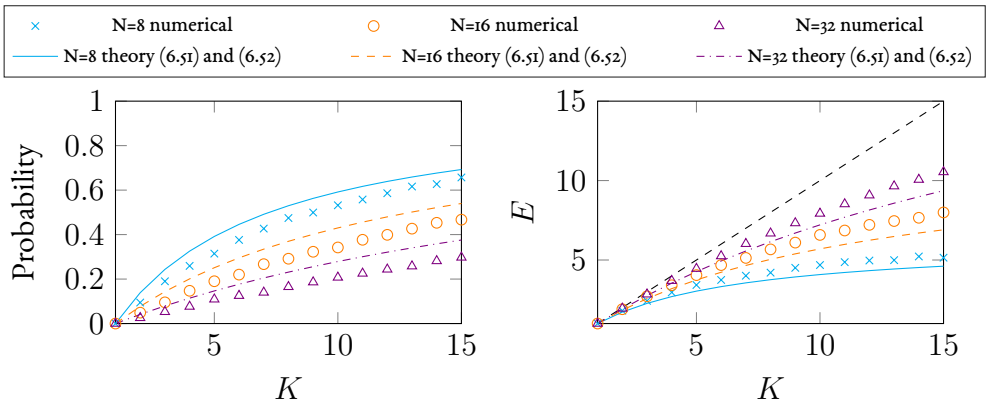

(a) Ineffectiveness probability. **(b)** effective components.

Figure 6.14: Ineffectiveness probability and number of components utilized obtained by MRC for different ULAs (FoV 180°). The lines represent the theoretical values, whereas the marks are given by numerical evaluation.

Fig. 6.15 shows how the SNR changes as a function of K for both the single-direction beam and the MRC methods. In particular, the lines are calculated with equations (6.64) and (6.72) respectively, whereas the marks are the simulated average SNRs

$$\bar{\Gamma} = \frac{1}{\sigma_{n_0}^2 \sum_{n=1}^{N} |\beta_n|^2 B_A} \int_{-\frac{B_A}{2}}^{\frac{B_A}{2}} |H(f)|^2 df \tag{6.76}$$

and

$$\bar{\Gamma}^{sing} = \frac{N}{\sigma_{n_0}^2 B_A} \int_{-\frac{B_A}{2}}^{\frac{B_A}{2}} |H^{sing}(f)|^2 df. \tag{6.77}$$

For this numerical evaluation we used a bandwidth of $B_A = 1$GHz and the path delays were randomly selected from a uniform distribution between 0 and 100ns. Here, it can be clearly seen that the accuracy of the approximation average-signal-to-average-noise-ratio in place of the SNR improves as K increases. As noted in Sec. 6.2.2, this approximation leads to an error of 3dB for $K = 1$, therefore we expect the error to always be lower than this value. For the proposed configurations, we can observe that the approximation error drops below 1dB for $K > 4$. We also notice that the gap between the two methods is relatively small, in the order of a few dB. Moreover, despite K is not large enough to show the convergence expected from (6.75), such result a suggests that the gap will not increase in more complex channels.

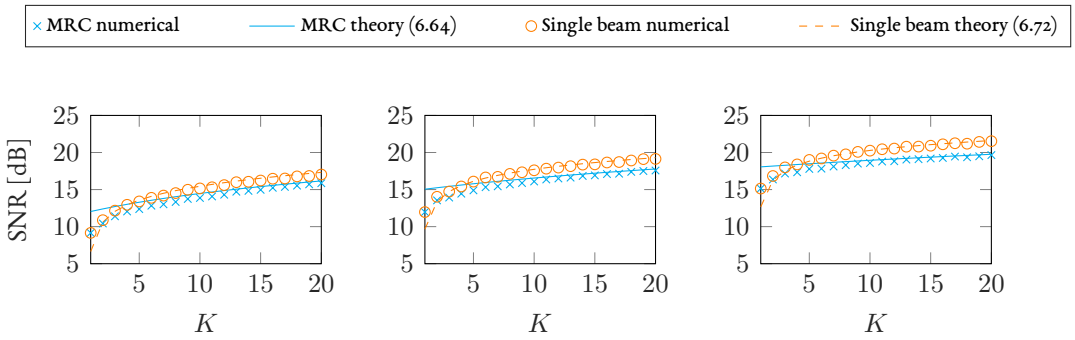

(a) $N = 8$. **(b)** $N = 16$. **(c)** $N = 32$.

Figure 6.15: SNR obtained by MRC and the single-direction beam for different ULAs, for a FoV of $180°$ and $\sigma_{n_0} = 1$, and for different values of the number N of antennas.

To evaluate the impact of the additional diversity generated introduced by MRC, we generated the beam for a given channel $H(f)$, then simulated a blockage by removing compo-

nent k', where k' is randomly selected between 1 and K, generating the new channel

$$H'(f) = H(f) - \alpha_{k'} e^{j\phi_{n,\vec{r}_{k'}}} e^{-j2\pi f \tau_{k'}}. \tag{6.78}$$

We then applied the beam designed for $H(f)$ to the new channel $H'(f)$ and evaluated the SNR obtained by the two methods.

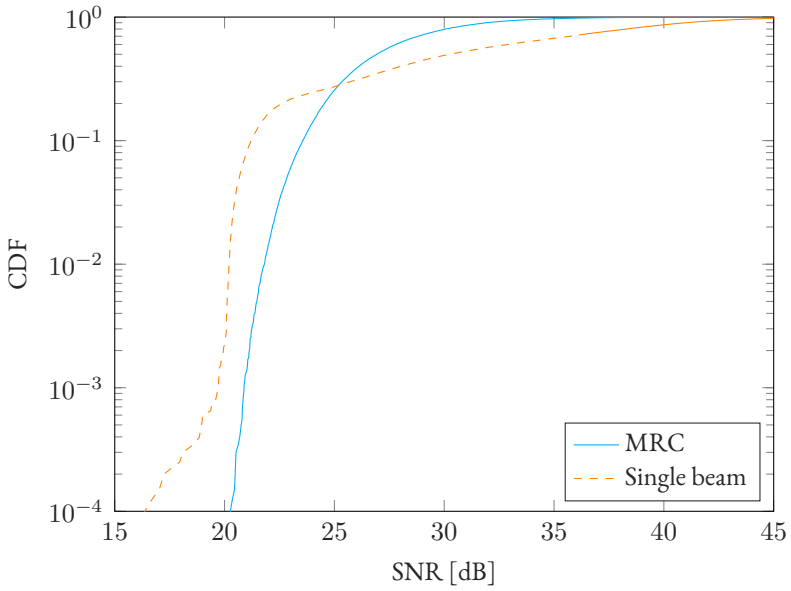

Figure 6.16: SNR distribution for an 8 element ULA with a FoV of $180°$, $K = 20$ and $\sigma_{n_0} = 1$.

In Fig. 6.16 we can observe the resulting SNR distribution. As expected, we can observe that the tail of the SNR obtained with a single beam extends much further than that of MRC, because the single beam approach is much more sensitive to the loss of the component used by the beam, since the remaining energy only comes from sidelobes.

Finally, we recall that the proposed theory has been developed assuming a noiseless channel estimation. In practice however, the channel estimate will be noisy. To investigate the performance impact of the channel estimate's noise computed the channel gain with the noisy beamforming coefficients

$$\beta'_n = \beta_n + w(\sigma) \tag{6.79}$$

where w is a Gaussian random variable with zero mean and standard deviation σ. With those

beamforming coefficients we compute a new CFR

$$H'(f) = \sum_{n=1}^{N} \beta'_n H_n(f) \tag{6.80}$$

Figure 6.17 shows the degradation of the beamforming gain

$$\Delta^{dB} = 20 \log_{10} \left(\frac{\int_{-\frac{B_A}{2}}^{\frac{B_A}{2}} H(f) df}{\int_{-\frac{B_A}{2}}^{\frac{B_A}{2}} H'(f) df} \right) \tag{6.81}$$

as a function of the SNR of the channel estimate.

$$\Gamma_{est} = \frac{\sum_{n=1}^{N} \beta_n^2}{N\sigma^2} \tag{6.82}$$

Here we can observe that, even with very low SNR of the order of 0dB, the degradation is limited to a few dB. This shows how MRC is not only robust to blockages, but also to noise in the estimate.

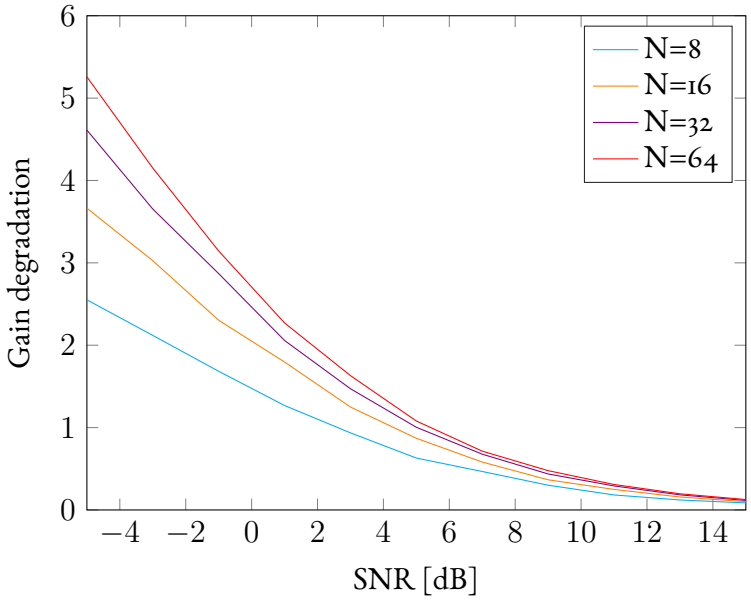

Figure 6.17: Channel estimate SNR impact on the beamforming gain.

Overall, these results show that the MRC beam is more suited than the classical single

direction beam for high-reliability applications. Such applications, as discussed in Sec. 2.1, are common in industrial settings.

6.2.4 Interference

With this theory, it is also possible to evaluate the average-signal-to-average-interference ratio. Assume an interferer channel composed of I multipath components, which have coefficients $\tilde{\alpha}_i$ with statistical power of σ_I, delay $\tilde{\tau}_i$ and direction $\tilde{r}_i$. With these assumptions, the CFR between the interferer and antenna n is

$$\tilde{H}_n(f) = \sum_{i=1}^{I} \tilde{\alpha}_i e^{j\phi_{n,\tilde{r}_i}} e^{j2\pi f \tilde{\tau}_i}. \tag{6.83}$$

By observing the calculation performed in (6.43) to (6.46), we notice that if the distribution of the directions of arrival of the interferer is the same as the intended channel, the power gain observed by each interferer path is Ka^2. In this case, the total received interference gain is simply $P_I = IKa^2$, and the average-signal-to-average-interference-ratio is

$$\Gamma_I = \frac{\mathbb{E}\left[|H(f)|^2\right]}{P_I} = \frac{2 + \bar{K}a^2}{I\sigma_I^2 a^2} \tag{6.84}$$

Whereas for the case of a beam pointed in a single direction we have $P_I^{(sing)} = Ia^2$ and the average signal to average interference ratio is

$$\Gamma_I^{sing} = \frac{\mathbb{E}\left[|H^{(sing)}(f)|^2\right]}{P_I^{(sing)}} = \frac{\log(K) + \gamma + \bar{K}a^2}{I\sigma_I^2 a^2} \tag{6.85}$$

We notice that their ratio is the same as the ratio in (6.74), therefore, it might be tempting to claim that the MRC beam is not much worse than the single beam in terms of average signal to average interference ratio. In this case however, the average-signal-to-average-interference-ratio is not a good approximation of the SIR.

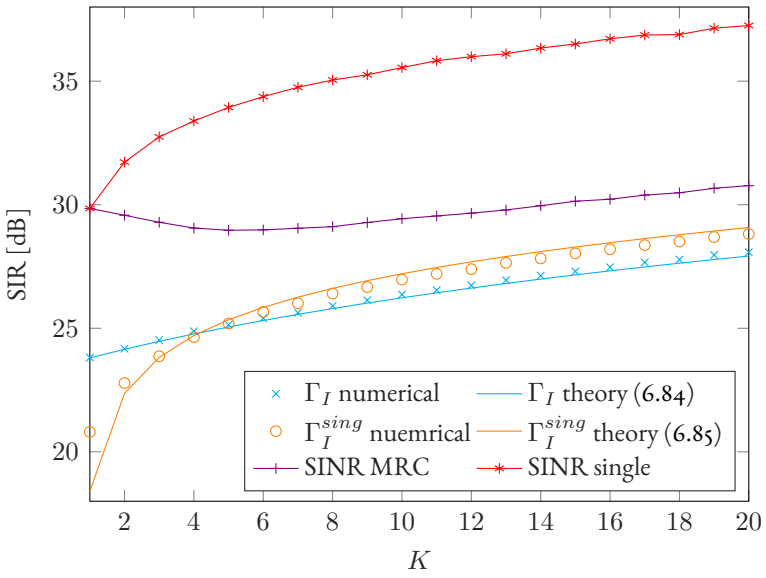

Figure 6.18: SIR for an 8 element ULA with a FoV of $180°$, $\sigma_I = 0.1$ and $I = 5$.

In figure 6.18 we can observe the values of Γ_I and Γ_I^{sing} for a compared with the numerical evaluation. In particular, the lines are the values of equations 6.84 and 6.85. The corresponding marks are the simulated average-signal-to-average-interference-ratios, whereas the marked lines are the simulated average SIR. Here we can observe how the model correctly captures the average-signal-to-average-interference-ratio, which however, in this case, is not a good approximation of the SIR. Most importantly, we note that in this case the MRC method seems to be more sensitive to interference than predicted, compared to the single beam. This suggests that MRC might underperform in terms of average throughput in scenarios with heavy interference. This, however, can be mitigated with other techniques which reduce the power of the interferer observed at the receiver, such as using zero forcing beamforming at the BS. Moreover, the average SIR is not the only relevant metric. In figure 6.19 we can observe the distribution of SIR or an 8 element ULA with a FoV of $120°$, $\sigma_I = 0.1$, $I = 5$ and $K = 20$. Here we can observe how the average SIR is indeed higher for the single beam, however, the MRC beam shows a shorter tail. Indeed, the probability of the SIR being above 20dB is around 0.17% for the single beam and 0.83% for MRC. In a high-reliability context, where the tail of the distribution is the key contributor, MRC will therefore perform significantly better.

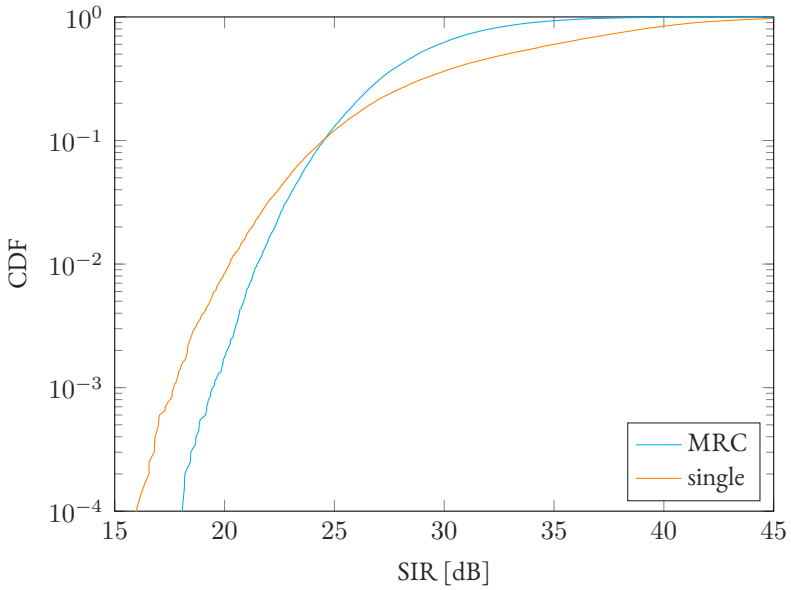

Figure 6.19: SIR distribution for an 8 element ULA with a FoV of $120°$, $\sigma_I = 0.1$, $I = 5$ and $K = 20$.

As we have discussed in Secs. 6.1 and 6.2, the digital RF chain can be exploited to both perform MIMO communication on a narrow sub-band and design a robust analog beam for the rest of the band. In this section, we discuss the advantage of jointly using these two features when dealing with the specific traffic requirements of an industrial application. First of all, let us note that in industrial environments we expect a large number of users with a limited throughput. Therefore, the allocation discussed in Sec. 6.1 is likely to fully exploit the MIMO capabilities through the band. This guarantees that the data can be transferred efficiently and reliably.

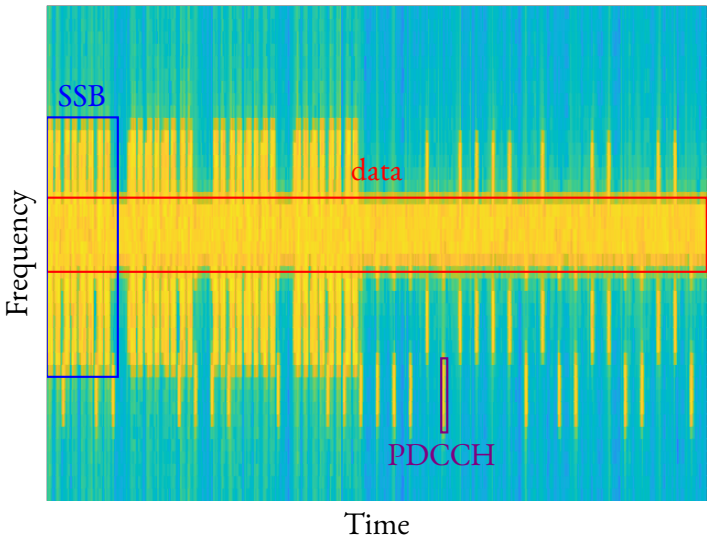

Figure 6.20: Example of 5G downlink spectrogram.

In most communication standards, however, there are common control signals which might span outside the part of the bandwidth assigned for digital beamforming for each user. For example, Fig. 6.20 shows the spectrogram of a 5G signal with some data allocation for a single user at the center of the bandwidth. Here we can observe that, on top of the user's allocation, there are other parts of the spectrum on which the BS transmits. These include, e.g., the System Information Blocks (SIBs) [49], Synchronization Signal Block (SSB), Master Information Block (MIB) and Physical Downlink Control Channel (PDCCH) [50]. We note that these signals are typically modulated with a very low Modulation and Coding Scheme (MCS), therefore their demodulation can only fail if the SNR is extremely low. Let us now summarize the impact of the proposed techniques on the reliability of the system. In partic-

ular, let us consider the issues that can lead to a missed or late delivery of a packet. The main reasons this can happen are:

1. There is an error in the demodulation of the packet itself.
2. There is an error in the demodulation of some control signals, such as Downlink Control Information (DCI), which leads to not demodulating the packet at all or even disconnecting from the network.
3. There is not enough throughput to serve all users, therefore the packets experience excess queuing delays.

These effects are all mitigated by the proposed solution, in particular:

- Issue number 1 is mitigated by the robustness of MIMO. It is well known that fully digital beamforming can better exploit the diversity provided by the channel, and therefore will be more robust to fast fading and other channel impairments [51, 52, 53]. Thanks to the results of Sec. 6.1 we can assume that most packets will be allocated to use digital beamforming, therefore the reliability of the connection will improve.
- Issue number 2 might not be mitigated by the use of fully digital beamforming, as the control signals are often spread in the whole bandwidth. However, this issue is mitigated by the robustness of the analog beam. We recall that, as stated above, the control signals are typically transmitted with a very robust MCS, and therefore it is not critical to have a high average SNR. It is instead necessary to have a short tail of the SNR distribution. This has been shown to happen for MRC in Sec. 6.2.
- Issue number 3 is again mitigated by the presence of fully digital MIMO. As shown in section 6.1 in fact, this allows for a higher overall throughput within the BS, thus reducing the likelihood of experiencing large queuing delays.

7

Sensing

In this section we propose a novel JCAS method that exploits the wideband analog beamformer of the architecture, to accurately estimate the Time of Arrival (ToA) of the multipath components. Then, applying MRC between multiple non-coherent frames the path component associated with each estimated ToA is amplified in the digital beamforming domain. Finally, Angle of Arrival (AoA) estimation is performed by exploiting the digital beamforming part of the architecture. This method has several advantages: First of all, it supports the acquisition of the analog and digital beamforming signal with different bandwidths, thus allowing the usage of the proposed architecture. Secondly, the use of analog beamforming for the ToA estimate provides enhanced SNR, thus helping to prevent the SNR collapse [54] of the MUltiple SIgnal Classification (MUSIC) algorithm, i.e. the situation where a noise eigenvector is selected over a signal one due to random fluctuations of the eigenvalues. Finally, the method relies on subsequent 1D parameter estimation, rather than joint 2D estimations. This greatly improves its computational complexity. We evaluate the performance of the proposed method, both in terms of parameter estimation error and close target resolution capabilities, and compare its performance with the performance of 2D MUltiple SIgnal Classification (2D-MUSIC) [55]. We show that, despite the dramatically lower hardware and software complexity and the reduced power consumption, the proposed system has comparable performance to state-of-the-art solutions.

In this chapter, we assume a ULA array and a system operating with an OFDM modulation with S subcarriers and a subcarrier spacing of Δ_f, thus the bandwidth is $B_A = S\Delta_f$. We assume that either the UE or the environment are not static, and therefore the channel parameters are not constant over time. We assume to collect the signal of F frames such that the phase of the coefficients α_k changes due to the Doppler shift, but the geometric parameters of the system τ_k and θ_k stay constant. For example, if we collect a frame every 0.1ms, a car moving at 15m/s (54 kmh) speed is displaced by 1.5mm. Although negligible in terms of range, at 60GHz carrier frequency, this displacement introduces a phase shift larger than $90°$. With these assumptions, and recalling (5.6) and (5.7), we write the frame-dependent CIR for the i-th frame as

$$h_n(i,t) = \sum_{k=1}^{K} \alpha_{(k,i)} e^{jn\pi\cos(\theta_k)} \delta(t-\tau_k), \tag{7.1}$$

and its Fourier transform

$$H_n(i,f) = \sum_{k=1}^{K} \alpha_{(k,i)} e^{jn\pi\cos(\theta_k)} e^{-j2\pi f\tau_k}. \tag{7.2}$$

Since we are operating with OFDM, we assume to obtain a noisy channel estimate for the analog beamforming chain, which can be expressed as:

$$\hat{H}_A(i, s\Delta_f) = \sum_{n=0}^{N-1} \beta_{n,i} H_n(i, s\Delta_f) + w, \tag{7.3}$$

$$s \in \left\{ -\left\lceil \frac{S}{2} \right\rceil, ..., \left\lfloor \frac{S}{2} \right\rfloor \right\}, \tag{7.4}$$

where $\beta_{n,i}$ is the complex beamforming coefficient for antenna n and $w \sim \mathcal{N}(0, \sigma_{est})$ is a white Gaussian noise. Similarly, for the digital beamforming we have the channel estimate for each antenna, but with a limited bandwidth, which is:

$$\hat{H}_m(i, s\Delta_f) = H_m(i, s\Delta_f) + w, \tag{7.5}$$

$$s \in \left\{ -\left\lceil \frac{S}{2M} \right\rceil, ..., \left\lfloor \frac{S}{2M} \right\rfloor \right\}, m \in \mathcal{M}. \tag{7.6}$$

Note that the relation of σ_{est} with the noise standard deviation at the antenna σ_{n_0} depends on a large set of factors, including the channel estimation technique, power of the pilots and potential filtering of the result, therefore we will consider the result only as a function of the channel estimate noise σ_{est}. For the sake of a fair comparison with classical methods, we define an *equivalent MIMO system*, that uses fully digital beamforming with the same aggregate sample rate of the proposed architecture on N' antennas. In other words, such system has a bandwidth $B'_A = \frac{2B_A}{N'}$. This system is not exactly equivalent in terms of cost and power consumption, however, considering the observations in Sec. 4.3, where we note that the ADCs have the most impact on the system cost and consumption, we consider this a reasonable comparison. Furthermore, Since it is using a different bandwidth, the noise observed by such system is also different. We therefore assume it has a noise standard deviation of $\sigma'_{est} = \frac{B'_A}{B_A}\sigma_{est}$.

7.2 Sensing method

Fig. 7.1 illustrates the proposed approach for accurate ToA and AoA estimation. First, we estimate the ToA of the multipath components by applying a super-resolution algorithm (in our case MUSIC [56], but other techniques might be used) on the CSI obtained from the wideband analog beamforming. Given the large bandwidth, the resulting ToA estimation is highly accurate. In the second step, for each estimated ToA, we process the channel estimates from the narrowband digital beamforming to amplify the component related to the ToA of interest. In particular, we use coherently combine the signal over frequency and frame to enhance the component of interest and suppress the other components and the noise. Finally, using the matrix pencil algorithm, the AoA of each path is estimated from the amplified CSI.

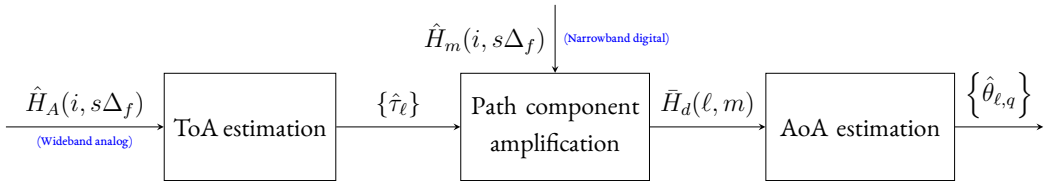

Figure 7.1: Block diagram of the proposed method

Without loss of generality, let us assume that we use a set of F consecutive frames starting from frame 0. We recall that the frames must be non-coherent, i.e. the phase of each component changes between frames, so the time between frames should be at least a good fraction of the Doppler frequency. Moreover, F should be chosen such that the targets do not move significantly between the first and last frame (i.e. its position change is much smaller than $\frac{c}{B_A}$).

7.2.1 Time domain decomposition

As mentioned in the brief description of the method, we first estimate the ToA of the multipath components using the MUSIC algorithm [56].

MUSIC is a subspace-based super-resolution algorithm that relies on the eigenvalue decomposition of the sample covariance matrix of the received signal as follows:

$$\boldsymbol{R}_y = \boldsymbol{Y}\boldsymbol{Y}^H \tag{7.7}$$

where $\boldsymbol{Y}$ is computed as:

$$\boldsymbol{Y} = \begin{bmatrix} \hat{H}_A\left(0, -\left\lceil \frac{S}{2} \right\rceil\right) & \cdots & \hat{H}_A\left(F-1, -\left\lceil \frac{S}{2} \right\rceil\right) \\ \vdots & & \vdots \\ \hat{H}_A\left(0, \left\lfloor \frac{S}{2} \right\rfloor\right) & \cdots & \hat{H}_A\left(F-1, \left\lfloor \frac{S}{2} \right\rfloor\right) \end{bmatrix}. \tag{7.8}$$

The covariance matrix $\boldsymbol{R}_y$ can be re-written as

$$\boldsymbol{R}_y = \boldsymbol{A}\boldsymbol{R}_s\boldsymbol{A}^H + \sigma_{est}^2\boldsymbol{I} \tag{7.9}$$

where

$$\boldsymbol{A} = \begin{bmatrix} e^{-j2\pi\left(-\left\lceil \frac{S}{2} \right\rceil\right)\Delta_f\tau_1} & \cdots & e^{-j2\pi\left(-\left\lceil \frac{S}{2} \right\rceil\right)\Delta_f\tau_K} \\ \vdots & & \vdots \\ e^{-j2\pi\left\lceil \frac{S}{2} \right\rceil\Delta_f\tau_1} & \cdots & e^{-j2\pi\left\lceil \frac{S}{2} \right\rceil\Delta_f\tau_K} \end{bmatrix}, \tag{7.10}$$

$$R_s = \boldsymbol{\chi}\boldsymbol{\chi}^H, \boldsymbol{\chi} = \begin{bmatrix} \sum_{n=0}^{N-1} \beta_{n,i}\alpha_{(1,0)}e^{jn\pi\cos(\theta_1)} & \cdots & \sum_{n=0}^{N-1} \beta_{n,i}\alpha_{(1,F-1)}e^{jn\pi\cos(\theta_1)} \\ \vdots & & \vdots \\ \sum_{n=0}^{N-1} \beta_{n,i}\alpha_{(K,0)}e^{jn\pi\cos(\theta_K)} & \cdots & \sum_{n=0}^{N-1} \beta_{n,i}\alpha_{(K,F-1)}e^{jn\pi\cos(\theta_K)} \end{bmatrix}, \tag{7.11}$$

and $\boldsymbol{I}$ is the identity matrix. The intuition behind the method comes from this decomposition: we can notice that the image of R_y can be decomposed into two subspaces:

- The signal space, associated with the first term of Eq. (7.9), which is the subspace generated by the columns of $\boldsymbol{A}$.
- The noise subspace, associated with the second term of Eq. (7.9), which is the subspace orthogonal to the signal subspace.

We can also infer that, given a sufficient SNR, the eigenvalues associated with the signal subspace will be significantly larger than the ones associated with the noise subspace. MUSIC extracts the noise subspace by removing the eigenvectors corresponding to the largest eigenvalues of $\boldsymbol{R}_y$ as the vectors that span the signal subspace. The remaining eigenvectors, which correspond to the near-zero eigenvalues, constitute the noise matrix $\boldsymbol{U}_n$. Finally, we can compute the MUSIC spectrum, $P_{\text{MUSIC}}(\tau) = \frac{1}{\boldsymbol{a}^H(\tau)\boldsymbol{U}_n\boldsymbol{U}_n^H\boldsymbol{a}(\tau)}$, where $\boldsymbol{a}(\tau) = [1, e^{-j2\pi\Delta_f\tau}, ..., e^{-j2\pi(S-1)\Delta_f\tau}]^T$ is the steering vector associated with the delay τ.
By definition of the noise subspace, if $\tau \to \tau_k$ for some k, due to the subspace orthogonality, $\boldsymbol{a}^H(\tau)\boldsymbol{U}_n\boldsymbol{U}_n^H\boldsymbol{a}(\tau) \to 0$, and therefore the MUSIC spectrum has a large value. We detect

this condition by performing a peak detection on $P_{\text{MUSIC}}(\tau)$ and report the list of peak times $\mathcal{T} = \{\hat{\tau}_1, ..., \hat{\tau}_L\}$. We note that, in general, there is no guarantee that this method will detect all components. This is due to the choice of the beamforming coefficients $\beta_{n,i}$, which could cause some of the components to have a low gain. Nevertheless, as we have proven in Sec. 6.2, when using the MRC beam we can expect the channel estimate $\hat{H}_A(i, s\Delta f)$ to contain information about most of the multipath component received. This is critical for a successful multipath decomposition. If a single directional beam was used, the information about other multipath components would be lost, and therefore the method would fail to identify other components. Moreover, to improve the SNR of low amplitude components, we can add a perturbation to the beam. For example, we can define the new beamforming coefficients as

$$\beta'_n(\xi, \varphi) = \xi e^{jn\pi \cos(\varphi)} + (1 - \xi)\beta_n \tag{7.12}$$

where $\xi \in (0, 1)$ and β_n are normalized coefficients. This perturbation adds an artificial lobe in the direction φ with an amplitude ξ, which could potentially illuminate better some far or low reflective objects. An example of the resulting array factor farfield pattern with and without the additional lobe can be seen in Fig. 7.2, where we show in blue the original pattern, and in dashed black we can see 4 examples with an additional side lobe at $-60°$, $-50°$, $-40°$ and $-30°$ respectively. The sidelobe has been added with a relative amplitude of $\xi = 0.2$. As it can be clearly seen, the addition of the side lobe has a negligible impact on the gain of the main pattern. The direction φ can then be swept to make sure that every possible object is illuminated. Moreover, since we use only a fraction of the energy equal to $(1 - \xi)^2$ in that beam, the communication should receive a penalty in SNR of roughly $-20\log(1 - \xi)$, which for small ξ values should be negligible (e.g., $\xi = 0.2$ will cause a loss of roughly 2dB).

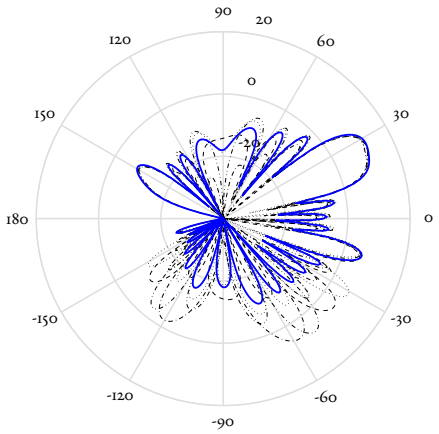

Figure 7.2: Beamformed farfield pattern [dBi] without the additional lobe (blue) and with an additional lobe in different directions (black)

7.2.2 Component amplification

After we separate the components in the time domain, for each $\hat{\tau}_\ell \in \mathcal{T}$ we estimate the corresponding complex amplitude at each frames as

$$\hat{\alpha}_{(\ell,i)} = \sum_{s=-\left\lceil \frac{S}{2} \right\rceil}^{\left\lfloor \frac{S}{2} \right\rfloor} e^{j2\pi\hat{\tau}_\ell s} H_A(i, s\Delta_f). \tag{7.13}$$

We can now compute the digitally combined channel response for time $\hat{\tau}_\ell$ and antenna $m \in \mathcal{M}$ as:

$$\bar{H}_d(\ell, m) = \sum_{i=0}^{F-1} \sum_{s=-\left\lceil \frac{S}{2M} \right\rceil}^{\left\lfloor \frac{S}{2M} \right\rfloor} \hat{\alpha}^*_{(\ell,i)} e^{j2\pi\hat{\tau}_\ell \tau s\Delta_f} \hat{H}_m(i, s\Delta_f). \tag{7.14}$$

This is the channel that will be used later for the AoA estimation. To show that it does indeed amplify the component associated with the given ToA, we replace the channel model in the expression. Assuming a correct ToA and channel coefficient estimation, i.e. $\hat{\tau}_\ell = \tau_{\hat{k}}$ and

$\hat{\alpha}_{(\ell,i)} = \alpha_{(\hat{k},i)}$ for some $\hat{k}$, and a constant beam $\beta_{n,i} = \beta_n$, we obtain *

$$\bar{H}_d(\hat{\tau}_\ell, m) = \sum_{i,s} \Bigg[\left(\sum_{n=0}^{N-1} \beta_n \sum_{k=1}^{K} \alpha_{(\hat{k},i)} e^{jn\pi\cos(\theta_k)} \delta(\tau_{\hat{k}} - \tau_k) \right)^* \cdot$$
$$e^{j2\pi\tau_{\hat{k}} s\Delta_f} \left(\sum_{k=1}^{K} \alpha_{(k,i)} e^{jn\pi\cos(\theta_k)} e^{-j2\pi s\Delta_f \tau_k} + w \right) \Bigg]. \tag{7.15}$$

We now define $\Xi_n = \sum_{n=0}^{N-1} \beta_n e^{jn\pi\cos(\theta_{\hat{k}})}$ for compactness. We also note that the noise statistic is unaffected by a rotation in the complex plane, hence we can rewrite the expression as

$$\bar{H}_d(\hat{\tau}_\ell, m) = \Xi_n \sum_{i,s} \alpha^*_{(\hat{k},i)} \sum_{k=1}^{K} \alpha_{(k,i)} e^{jn\pi\cos(\theta_k)} e^{j2\pi s\Delta_f(\tau_{\hat{k}} - \tau_k)} + w. \tag{7.16}$$

Without loss of generality, we assume $\hat{k} = 1$ and $\Xi_n = 1$. Then Eq. (7.16) can expressed as:

$$\bar{H}_d(\hat{\tau}_\ell, m) = \sum_{i,s} |\alpha_{(1,i)}|^2 e^{jn\pi\cos(\theta_1)} \tag{7.17}$$
$$+ \sum_{k=2}^{K} \sum_{i,s} \alpha^*_{(\hat{k},i)} \alpha_{(k,i)} e^{jn\pi\cos(\theta_k)} e^{j2\pi s\Delta_f(\tau_{\hat{k}} - \tau_k)} \tag{7.18}$$
$$+ \sum_{i,s} \alpha^*_{(\hat{k},i)} w. \tag{7.19}$$

Here we can see that the component with $k = 1$ is combined coherently, whereas the other components, as well as the noise, are combined incoherently. This ensures that the component of interest is amplified. This operation is the core novelty of the proposed method, as it allows the ToA and AoA association that would be otherwise impossible because the narrowband part does not have enough bandwidth. The key observation here is that, while the wideband analog and narrowband digital domains do not share a common AoA or ToA information that can be reliably used for the association, they do share the doppler domain, so the phase change over multiple frames is the only possible mean to associate the ToA and AoA results.

*We omit the limits of s and i for compactness

7.2.3 Angle of arrival extraction

We then apply the Matrix Pencil method [57, 58, 59, 60] to the vector of combined channels $\bar{\mathbf{H}}_d(\hat{\tau}_\ell) = \left(\bar{H}_d(\hat{\tau}_\ell, 1), ..., \bar{H}_d(\hat{\tau}_\ell, M)\right)$ with a pencil parameter P to obtain the estimated spatial frequencies and amplitude of the components. The Matrix Pencil method works as follows. From the vector $\bar{\mathbf{H}}_d(\hat{\tau}_\ell)$, we generate a Hankel matrix:

$$\mathcal{H}_{\ell,P} = \begin{bmatrix} \bar{H}_d(\hat{\tau}_\ell, 1) & ... & \bar{H}_d(\hat{\tau}_\ell, P) \\ \bar{H}_d(\hat{\tau}_\ell, 2) & ... & \bar{H}_d(\hat{\tau}_\ell, P+1) \\ \vdots & \vdots & \vdots \\ \bar{H}_d(\hat{\tau}_\ell, M-P) & ... & \bar{H}_d(\hat{\tau}_\ell, M) \end{bmatrix}. \tag{7.20}$$

From this matrix, we generate the two matrices $\mathcal{H}^{(1)}_{\ell,P}$ and $\mathcal{H}^{(2)}_{\ell,P}$ removing the last and first column of $\mathcal{H}_{\ell,P}$ respectively. It can be shown that the generalized eigenvalues of the pair $\left\{\mathcal{H}^{(1)}_{\ell,P}, \mathcal{H}^{(2)}_{\ell,P}\right\}$ are of the form $e^{j\frac{2\pi}{M}\omega_{\ell,q}}$, where $\omega_{\ell,q}$ is the spatial frequency associated with the i-th component [57, 58, 59, 60]. Therefore, for the generic ℓ^{th} component, we obtain a set of spatial frequencies $\Omega_\ell = \{\omega_{\ell,1}, ..., \omega_{\ell,M-P}\}$. For each spatial frequency, thus obtaining the set of amplitudes $\mathcal{A}_\ell = \{\hat{\alpha}_{\ell,1}, ..., \hat{\alpha}_{\ell,M-P}\}$, where:

$$\hat{\alpha}_{\ell,q} = \sum_{d=1}^{M} \bar{H}_d(\hat{\tau}_\ell, q) e^{-j\frac{2\pi d}{M}\omega_{\ell,q}}. \tag{7.21}$$

If the number of components associated with the time domain sample $\hat{\tau}_\ell$ are less than $M-P$, some of the components reported will be a result of noise. Therefore, we apply a threshold to the amplitudes $\mathcal{A}$ to remove potential noisy components. In particular, the threshold is defined as:

$$\text{Thr} = \rho\sqrt{\frac{1}{M}\sum_{m=1}^{M} |\bar{H}_d(\hat{\tau}_\ell, m)|^2}, \tag{7.22}$$

where ρ is a parameter that regulates the tradeoff between false positives and false negatives. The components $\{q : |\hat{\alpha}_q| > \text{Thr}\}$ are considered as real components, and their angle is estimated as $\hat{\theta}_{\ell,q} = cos^{-1}\left(\frac{2\omega_{\ell,q}}{M}\right)$. We finally generate the result set $\mathcal{Z} = \{Z_1, ..., Z_O\}$ of output range-angle pairs of the form $Z_o = \left(\hat{\tau}_\ell, \hat{\theta}_{\ell,q}\right)$. For the sake of a lighter notation, we define $\tau(Z_o) = \hat{\tau}_\ell$ and $\theta(Z_o) = \hat{\theta}_{\ell,q}$. The complete procedure is summarized in algorithm 7.1.

Algorithm 7.1 Sensing algorithm

$\mathcal{Z} \leftarrow \{\}$
$\mathcal{T} \leftarrow MUSIC(\hat{H}_A(i,s))$
for each $\ell \in \{1, ..., L\}$
    $\hat{\alpha}_{\ell,i} \leftarrow \sum_{s=-\lceil \frac{S}{2} \rceil}^{\lfloor \frac{S}{2} \rfloor} e^{j2\pi\hat{\tau}_\ell s} H_A(i, s\Delta_f)$
    $\bar{H}_d(\ell, m) \leftarrow \sum_{i=0}^{F-1} \sum_{s=-\lceil \frac{S}{2M} \rceil}^{\lfloor \frac{S}{2M} \rfloor} \hat{\alpha}^*_{(\ell,i)} e^{j2\pi\hat{\tau}_\ell s\Delta_f} \hat{H}_m(i, s\Delta_f)$
    Thr $\leftarrow \rho\sqrt{\frac{1}{M}\sum_{m=1}^{M} |\bar{H}_d(\hat{\tau}_\ell, m)|^2}$
    $\mathbf{\Omega}_\ell \leftarrow MatrixPencil(\bar{\mathbf{H}}_d(\hat{\tau}_\ell))$
    for each $\omega_{\ell,q} \in \mathbf{\Omega}_\ell$
        $\hat{a}_{\ell,q} \leftarrow \sum_{d=1}^{M} \bar{H}_d(\hat{\tau}_\ell, q) e^{-j\frac{2\pi d}{M}\omega_{\ell,q}}$
        if $|\hat{a}_{\ell,q}| \geq$ Thr
            $\mathcal{Z} \leftarrow \mathcal{Z} \cup \left\{\tau_\ell, cos^{-1}\left(\frac{2\omega_{\ell,q}}{M}\right)\right\}$

7.3 Results

Considering the large number of multipath components observed in industrial environments, we first investigate the ability of the system to isolate close targets. For this analysis, we consider an 8 antenna system with a bandwidth B_A = 400MHz, $S = 128$ subcarriers, $F = 10$ frames and an SNR of 10dB on each antenna. We generate a channel according to the model described (7.2) with 2 paths at $\theta_1 = 15°$, $\tau_1 = \frac{10\,\text{m}}{c}$, and $\theta_2 = 15° + \Delta\theta$ $\tau_2 = \frac{10\,\text{m}+\Delta L}{c}$, respectively. The complex amplitudes $\alpha_{1,i}$ and $\alpha_{2,i}$ have the same statistics, corresponding to a complex normal distribution of zero mean and the identity as covariance matrix. Moreover, we use $\rho = 0.3$ for the threshold in (7.22). We run the algorithm for $(\Delta\theta, \Delta L) \in \{0\,\text{m}, 0.0125\,\text{m}, \ldots, 0.5\,\text{m}\} \times \{0°, 0.25°, \ldots, 10°\}$. For each $(\Delta\theta, \Delta L)$ pair, we generate 100 realizations of the complex channel coefficients, as well as the noise. For each realization, we compare the output $\{Z_1, \ldots, Z_O\}$ with the real channel parameters as followings. For each estimated component Z_o, we find the closest real component according to the distance function

$$d\left(Z_o, (\tau_k, \theta_k)\right) = \sqrt{\frac{1}{\sigma_\tau^2}(\tau(Z_o) - \tau_k)^2 + \frac{1}{\sigma_\theta^2}(\theta(Z_o) - \theta_k)^2}. \tag{7.23}$$

Without loss of generality, let us assume that the closest component is the first one. In case $d\left(Z_o, (\tau_1, \theta_1)\right) < 1$, we associate the estimated component Z_o with the first component,

otherwise it is considered a spurious component. If both real components have an associated estimated component, we say that the components have been resolved. For this evaluation, we use $\sigma_\tau = \frac{30\,\text{cm}}{c}$ and $\sigma_\Theta = 3°$.

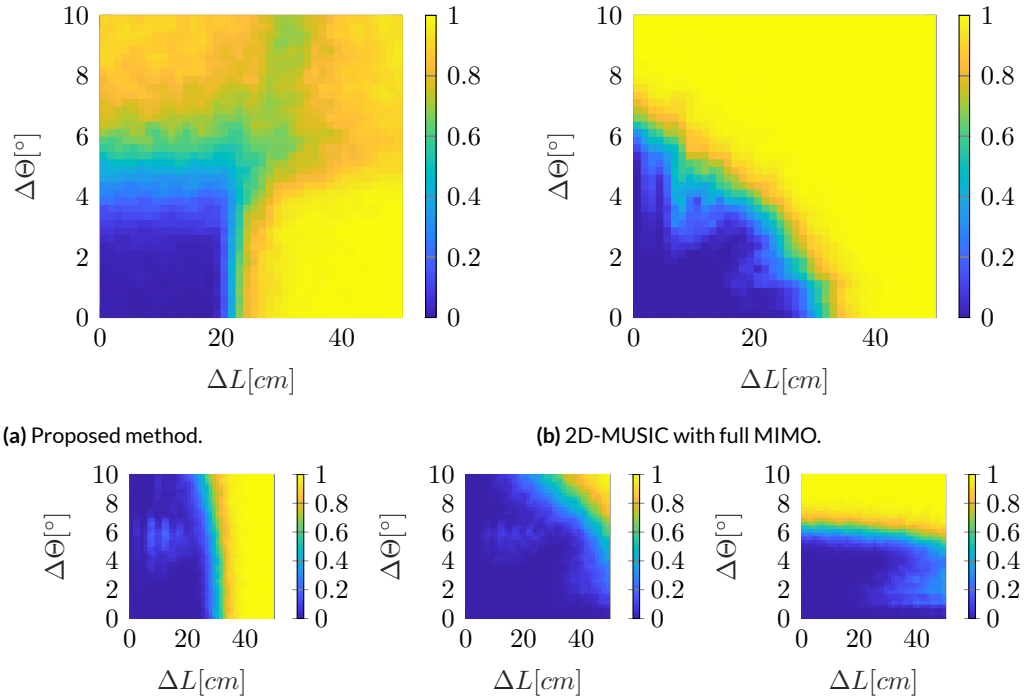

(a) Proposed method.

(b) 2D-MUSIC with full MIMO.

(c) 2D-MUSIC with 2 antennas.

(d) 2D-MUSIC with 4 antennas.

(e) 2D-MUSIC with 8 antennas.

Figure 7.3: Resolution probability comparison.

The resulting resolution probability is shown, for the proposed method as well as 2D-MUSIC on the full MIMO system, in Figs. 7.3a and 7.3b respectively. It should be noted that for 2D-MUSIC the correct number of components, and thus the size of the noise subspace, is provided as an input of the algorithm. In a real deployment, this parameter would need to be estimated as well, potentially further reducing the resolution capabilities of the method. We can see that the proposed method, despite using only 25% the total sample rate and having much lower complexity, performs comparably to the classical 2D-MUSIC in terms of resolution. In Figs. 7.3c, 7.3d and 7.3e we can observe the resolution for 2D-MUSIC for the *equivalent MIMO system* with $N' = \{2, 4, 8\}$. Here the sample rate is spent for either digitalizing multiple antennas or a larger bandwidth, therefore we can see that the systems have a good resolution in only one of the domains, but perform badly in the other. We therefore may easily notice that the proposed method exhibits a far superior resolution either

in range, angle or both, based on the allocation of the sample rate. Finally, In Fig. 7.4, we can see the resolution achieved by the proposed method when provided with digital beamforming for the full bandwidth. The result is very close to the one shown in Fig. 7.3a. This clearly shows that, at least from a resolution standpoint, fully digital MIMO on the whole bandwidth is not providing a huge advantage, and surely does not justify the huge increase in cost and power consumption.

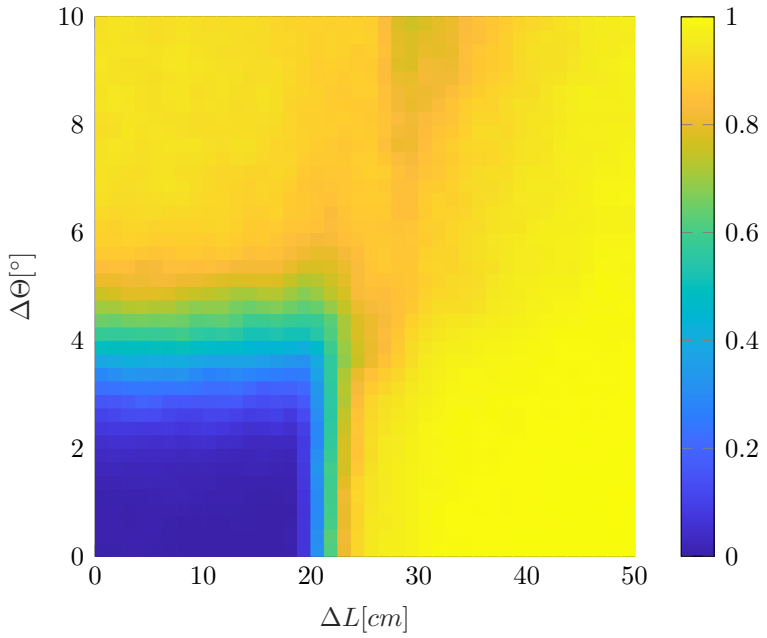

Figure 7.4: Resolution probability of the proposed method with a fully digital MIMO architecture.

In Fig. 7.5 we show the accuracy of the parameters estimated by the proposed method, as well as the one estimated by 2D-MUSIC for the full MIMO system and for the *equivalent MIMO systems* with $N' = \{2, 4, 8\}$ antennas. We generated a channel with a single component with a random angle and range, and ran the algorithm on a such channel to evaluate the error. We repeated the process for 1000 channel realizations to obtain an estimate of the RMSE, plotted as a function of the full band SNR, i.e., the SNR observed by a receiver that operates over the full bandwidth B_A. We recall that the SNR observed by the *equivalent MIMO architectures* can be lower due to the lower bandwidth.

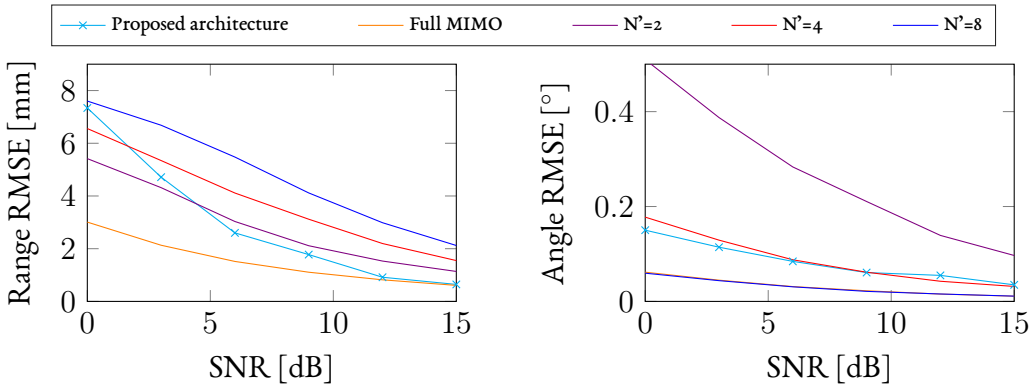

(a) Range RMSE.

(b) Angle RMSE.

Figure 7.5: Accuracy of the proposed method compared to 2D-MUSIC.

As it can be seen in the figure, at high SNR the performance of the proposed method is comparable with the full MIMO system, while they slightly degrade towards the low SNR regime. This degradation is likely due to the fact that in the simulation we used the noisy channel estimate for only one frame to design the beamforming coefficients, thus, the beam is itself affected by noise and provides a reduced gain. In practice, this could be mitigated by averaging the beamforming coefficients over time, to obtain a better beamforming gain.

In terms of angle, the system with $N' = 8$ antennas largely outperforms the proposed method. It should be noted however that this advantage is caused by the higher SNR due to the lower total bandwidth, which also implies a large degradation in terms of communication due to the low bandwidth.

7.4 Leakage issue

Due to imperfections in the coefficient estimation, when two targets are very close we often observe that some of the components are also visible at different times. An example is shown in Fig. 7.6, where we may notice the algorithm estimation result in the case where the channel has two components (depicted in orange) at $(10\text{ m}, 30°)$ and $(10.25\text{ m}, 35°)$. As we can see, the two components are correctly identified, but the algorithm also detects two leaked components at $(10\text{ m}, 35°)$ and $(10.25\text{ m}, 30°)$. When the distances get closer, these components may have a significant amplitude, and sometimes they are not filtered out with a simple threshold. Moreover, if the amplitude of one component is significantly larger than the others, we may even observe that at a specific time, the real component has a lower amplitude than the leaked one. This unfortunately means that it is possible to misidentify some

components when using the simple threshold strategy proposed in (7.22). For example, over the whole resolution experiment, we recorded an overall probability of observing at least a leaked component of 25%, i.e., we reported at least one spurious component over at least one-quarter of the channel realizations. On average, we observed 0.41 leaked components per realization. This suggests that the leakage problem is significant, at least for close targets. It should be noted though, that for more spread targets the issue is a lot less relevant. For example, repeating the expertiment with $(\Delta\theta, \Delta L) \in \{0\text{ m}, 1\text{ m}, \dots, 5\text{ m}\} \times \{0^\circ, 1^\circ, \dots, 10^\circ\}$, the average fraction of observations showing leakage reduces to 0.98%, with an average number of leaked component of 0.017. Moreover, it is always true that a real component is larger than the leaked component with the same angle, so it is possible to replace the threshold a better classification algorithm to identify the real components after the estimation. However, we will address this solution in future work.

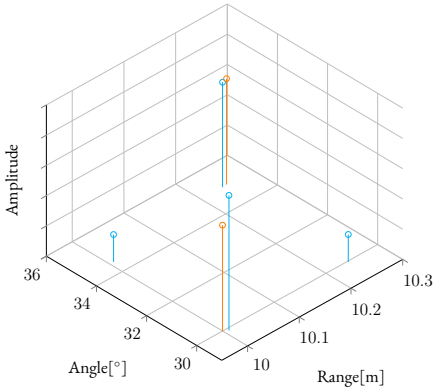

Figure 7.6: Example of leakage.

8

3GPP signaling for heterogeneous rank beamforming

Let us now analyze the signaling requirements for the proposed algorithms, and potential modification of the current 3GPP standard (Rel. 17) that are needed to utilize this technology. Firstly, we note that for the analog beamforming and sensing methods we do not need any signaling at all, as the methods merely rely on observing channel estimates obtained by the digital beamforming chains. In contrast, the resource allocation technique presented in Sec. 6.1 does require some signaling. In particular, we need to be able to perform the following tasks:

1. Notify the BS of the UEs capabilities of trading some analog chains for digital beamforming, as well as the number of antennas it can use in the digital beamforming chain.

2. Notify the UEs of which configuration should be used based on the status of the network (e.g. number of users and traffic pattern).

3. Update the UEs configurations as the network conditions change.

4. Notify a resource allocation that uses different capabilities in different parts of the band.

Let us now consider requirement number 1. In 3GPP, UE capabilities are reported in the Radio Resource Control (RRC) [61], and in particular in a specific Information Element (IE) called *UE-NR-Capability*. The Abstract Syntax Notation One (ASN.1) specification of such message can be found in Appendix A Msg. A.1. In particular, the information about the RF capabilities of the UE is contained in the the *rf-Parameters* IE, which is described in Msg. A.2. More specifically the fields related to the MIMO and beamforming capabilities are located in the *mimo-ParametersPerBand* IE inside the *BandNR* IE, which are described in Appendix A Msgs. A.3 and A.4 respectively.

To advertise the UE capability of performing the rank-bandwidth tradeoff for some RF chains we introduce a new IE called *analogdigitalbfcap* in the *mimo-ParametersPerBand* IE, as described in Msg. 8.1. The newly added IE is described in Msg. 8.2.

Message 8.1: Proposed change to the MIMO-ParametersPerBand IE.

```
MIMO-ParametersPerBand ::= SEQUENCE {
        ...,
        analogdigitalbfcap          SEQUENCE OF ABCap          OPTIONAL
}
```

Message 8.2: Proposed structure of the new ABCap IE.

```
ABCap :: = SEQUENCE {
        numfixanalogchains      ENUMERATED,
        numtradablechains ENUMERATED,
        tradcapab     BIT STRING (Size(8))
}
```

The fields in the ABCap IE have the following meaning

- *numfixanalogchains* is the number of RF chains that are exclusively capable of performing analog beamforming
- *numtradablechains* is the number of tradable RF chains, which are those RF chains that are capable of performing analog beamforming on the full bandwidth or digital beamforming on a part of the bandwidth

- *tradcapab* contains the information on the rank-bandwidth tradeoff that such RF chains can perform. In particular. In particular, if the b-th bit is set to 1 the UE can use the tradable RF chains to acquire the signal from 2^{b+1} antennas with bandwidth $\frac{B_A}{2^{b+1}}$.

8.2 UE configuration

We now investigate the signaling to perform tasks 2 and 3. These tasks are again implemented in the RRC [49], specifically in an IE named *ServingCellConfig*, described in Appendix A Msg. A.5 . This message contains the list *downlinkBWP-ToAddModList* which contains a set ofBandWidth Part (BWP) configurations, of the format *BWP-Downlink* described in A Msg. A.6, to be used by the UE. To configure the UE to perform digital beamforming in a specific part of the band, we propose to change this message as described in 8.3. In particular, we add the IE *bwp-Tradchain*, which is described in 8.4.

Message 8.3: Proposed change to the BWP-Downlink IE.

```
BWP-Downlink ::=      SEQUENCE {
    bwp-Id                BWP-Id ,
    bwp-Common            BWP-DownlinkCommon
    bwp-Dedicated         BWP-DownlinkDedicated
    bwp-Tradchain                 BWP-Tradchain
    ...
}
```

Message 8.4: Proposed structure of the BWP-Tradchain IE.

```
BWP-Tradchain ::=         SEQUENCE {
    genericParameters     BWP,
    tradcapuse    Bitstring(8)
    numtradechains  Integer(1-maxTradechains)
}
```

The new fields added in the *BWP-Tradchain* format are the following

- *genericParameters* is the field describing the location and bandwidth on which digital beamforming should be performed. It is of the standard format *BWP*, described in A

Msg. A.7.

- *tradcapuse* informs the UE of what tradeoff should be used, and is in the same format of the *tradcapab* field in the newly proposed *ABCap* IE.
- *numtradechains* informs the UE of how many of the tradable RF chains need to be configured to perform digital beamforming.

8.3 Resource allocation

The resource allocation is specified in the DCI message [62]. In particular, the downlink data allocation is specified in the DCI format1_1. The structure of such message is specified in table A.1. The *Frequency domain resource assignment* and *Time domain resource assignment* specify where the data is located in the resource grid. These parameters do not need to be updated, and allocation can be done as usual. The decision of whether to use the analog or digital beamforming chain will be implicit: The assigned resource blocks that fall within the digital beamforming BWP will be decoded with digital beamforming. However, there is still the need to add some parameters to the DCI, as we need to specify a different number of layers and MCS for the digital beamforming part. We therefore propose to add the following fields, listed in table 8.1 to the DCI format1_1.

Table 8.1: Additional parameters to DCI format1_1

Field	bits	Specification
Modulation and coding scheme for digital beamforming	5	Defined in [63] tables 5.1.3.1-1 and 5.1.3.1-2
Antenna port(s) and number of layers for digital beamforming	4,5,6	Determined by DMRS Configuration Specified in [62] tables 7.3.1.2.2-1 to 7.3.1.2.2-4

9 Conclusion

In this thesis, we discussed the applications, challenges and characteristics of industrial communication and sensing systems. We provided a comprehensive analysis of the channel properties observed in such environment, also providing an extensive set of measurements from a commercial port case study. Based on the channel characteristics, we proposed a novel beamforming architecture capable of dynamically trading bandwidth for beamforming rank on some RF chains, thus operating with a combination of a wideband analog beamforming and a narrowband digital beamforming system. Thanks to its lower number of ADCs, this architecture has a complexity, cost, and power consumption that sits in between the classical hybrid beamforming architecture and the fully digital beamforming. We have shown that, using such architecture in a multi-user system with a large number of users, fully digital beamforming rate on the whole bandwidth can be achieved with classical PF scheduling. Moreover, we proved that by setting the analog beamforming weight of the wideband RF chain to the MRC weights for the center frequency, we obtain a robust beam that exploits most of the multipath components provided by the environment. We also propose a multipath decomposition method that makes use of the proposed architecture, which can be used for localization and sensing tasks. The results of the method are close to the one obtained with fully digital beamforming in terms of both accuracy and resolution, despite using significantly less data and having much lower complexity. Finally, we briefly discussed how such architecture can be implemented in the current 3GPP standard. We have shown that this requires adding a handful of parameters to the RRC and DCI messages.

A

3GPP messages structure

This appendix contains a list of 3GPP messages relevant to this work. The content has been sourced from [64, 65, 61, 49, 62].

Message A.1: UE-NR-Capability

```
UE-NR-Capability ::= SEQUENCE {
    accessStratumRelease                AccessStratumRelease,
    pdcp-Parameters                     PDCP-Parameters,
    rlc-Parameters                      RLC-Parameters OPTIONAL,
    mac-Parameters                      MAC-Parameters OPTIONAL,
    phy-Parameters                      Phy-Parameters,
    rf-Parameters                       RF-Parameters,
    measAndMobParameters                MeasAndMobParameters OPTIONAL
        ,
    fdd-Add-UE-NR-Capabilities          UE-NR-CapabilityAddXDD-Mode
        OPTIONAL,
    tdd-Add-UE-NR-Capabilities          UE-NR-CapabilityAddXDD-Mode
        OPTIONAL,
    fr1-Add-UE-NR-Capabilities          UE-NR-CapabilityAddFRX-Mode
        OPTIONAL,
    fr2-Add-UE-NR-Capabilities          UE-NR-CapabilityAddFRX-Mode
        OPTIONAL,
    featureSets                         FeatureSets OPTIONAL,
    featureSetCombinations              SEQUENCE (SIZE (1..
```

```
        maxFeatureSetCombinations))
                                                    OF
                                                        FeatureSetCombination
                                                        OPTIONAL,
    lateNonCriticalExtension                OCTET STRING OPTIONAL,
    nonCriticalExtension                    UE-NR-Capability-v1530
        OPTIONAL
}
```

Message A.2: RF-Parameters

```
RF-Parameters ::= SEQUENCE {
    supportedBandListNR                     SEQUENCE (SIZE (1..maxBands)
        ) OF BandNR,
    supportedBandCombinationList            BandCombinationList
                        OPTIONAL,
    appliedFreqBandListFilter               FreqBandList
                                OPTIONAL

}
```

Message A.3: BandNR

```
BandNR ::=  SEQUENCE {
    bandNR                                  FreqBandIndicatorNR,
    modifiedMPR-Behaviour                   BIT STRING (SIZE (8))
                                OPTIONAL,
    mimo-ParametersPerBand                  MIMO-ParametersPerBand
                                OPTIONAL,
    extendedCP                              ENUMERATED {supported}
                                OPTIONAL,
    multipleTCI                             ENUMERATED {supported}
                                OPTIONAL,
    bwp-WithoutRestriction                  ENUMERATED {supported}
                                OPTIONAL,
    bwp-SameNumerology                      ENUMERATED {upto2, upto4}
                        OPTIONAL,
    bwp-DiffNumerology                      ENUMERATED {upto4}
```

```
                                    OPTIONAL,
    crossCarrierSchedulingDL-SameSCS          ENUMERATED {supported}
                                    OPTIONAL,
    crossCarrierSchedulingUL-SameSCS          ENUMERATED {supported}
                                    OPTIONAL,
    pdsch-256QAM-FR2                    ENUMERATED {supported}
                                    OPTIONAL,
    pusch-256QAM                        ENUMERATED {supported}
                                    OPTIONAL,
    ue-PowerClass                       ENUMERATED {pc2, pc3}
                                     OPTIONAL,
    rateMatchingLTE-CRS                 ENUMERATED {supported}
                                    OPTIONAL,
    ...
}
```

Message A.4: MIMO-ParametersPerBand

```
MIMO-ParametersPerBand ::= SEQUENCE {
    tci-StatePDSCH                          SEQUENCE {
        maxNumberConfiguredTCIstatesPerCC   ENUMERATED {n4, n8, n16,
            n32, n64}   OPTIONAL,
        maxNumberActiveTCI-PerBWP           ENUMERATED {n1, n2, n4,
            n8}         OPTIONAL
    }

      OPTIONAL,
    additionalActiveTCI-StatePDCCH      ENUMERATED {supported}
                                OPTIONAL,
    pusch-TransCoherence                ENUMERATED {nonCoherent,
                                                    partialNonCoherent
                                                        ,
                                                    fullCoherent}

                                                        OPTIONAL,
    beamCorrespondence                  ENUMERATED {supported}
                                OPTIONAL,
    periodicBeamReport                  ENUMERATED {supported}
                                OPTIONAL,
    aperiodicBeamReport                 ENUMERATED {supported}
```

```
                                OPTIONAL,
sp-BeamReportPUCCH                  ENUMERATED {supported}
                                OPTIONAL,
sp-BeamReportPUSCH                  ENUMERATED {supported}
                                OPTIONAL,
beamManagementSSB-CSI-RS            BeamManagementSSB-CSI-RS
                              OPTIONAL,
maxNumberRxBeam                     INTEGER (2..8)
                                 OPTIONAL,
maxNumberRxTxBeamSwitchDL           SEQUENCE {
    scs-15kHz                           ENUMERATED {n4, n7, n14}
                                OPTIONAL,
    scs-30kHz                           ENUMERATED {n4, n7, n14}
                                OPTIONAL,
    scs-60kHz                           ENUMERATED {n4, n7, n14}
                                OPTIONAL,
    scs-120kHz                          ENUMERATED {n4, n7, n14}
                                OPTIONAL,
    scs-240kHz                          ENUMERATED {n4, n7, n14}
                                OPTIONAL
}

  OPTIONAL,
maxNumberNonGroupBeamReporting      ENUMERATED {n1, n2, n4}
                                OPTIONAL,
groupBeamReporting                  ENUMERATED {supported}
                                OPTIONAL,
uplinkBeamManagement                SEQUENCE {
    maxNumberSRS-ResourcePerSet         ENUMERATED {n2, n4, n8,
        n16, n32},
    maxNumberSRS-ResourceSet            INTEGER (1..8)
}

  OPTIONAL,
maxNumberCSI-RS-BFR                 INTEGER (1..64)
                                 OPTIONAL,
maxNumberSSB-BFR                    INTEGER (1..64)
                                 OPTIONAL,
maxNumberCSI-RS-SSB-BFR             INTEGER (1..256)
                                OPTIONAL,
twoPortsPTRS-DL                     ENUMERATED {supported}
```

```
                                OPTIONAL,
twoPortsPTRS-UL                 ENUMERATED {supported}
                                OPTIONAL,
supportedSRS-Resources          SRS-Resources
                                OPTIONAL,
srs-TxSwitch                    SRS-TxSwitch
                                OPTIONAL,
maxNumberSimultaneousSRS-PerCC  INTEGER (1..4)
                                OPTIONAL,
beamReportTiming                SEQUENCE {
    scs-15kHz                       ENUMERATED {sym2, sym4,
        sym8}           OPTIONAL,
    scs-30kHz                       ENUMERATED {sym4, sym8,
        sym14}          OPTIONAL,
    scs-60kHz                       ENUMERATED {sym8, sym14,
         sym28}         OPTIONAL,
    scs-120kHz                      ENUMERATED {sym14, sym28
        , sym56}        OPTIONAL
}

    OPTIONAL,
ptrs-DensityRecommendationSetDL SEQUENCE {
    scs-15kHz                       PTRS-
        DensityRecommendationDL     OPTIONAL,
    scs-30kHz                       PTRS-
        DensityRecommendationDL     OPTIONAL,
    scs-60kHz                       PTRS-
        DensityRecommendationDL     OPTIONAL,
    scs-120kHz                      PTRS-
        DensityRecommendationDL     OPTIONAL
}

    OPTIONAL,
ptrs-DensityRecommendationSetUL SEQUENCE {
    scs-15kHz                       PTRS-
        DensityRecommendationUL     OPTIONAL,
    scs-30kHz                       PTRS-
        DensityRecommendationUL     OPTIONAL,
    scs-60kHz                       PTRS-
        DensityRecommendationUL     OPTIONAL,
    scs-120kHz                      PTRS-
```

```
        DensityRecommendationUL                 OPTIONAL
    }

    OPTIONAL,
    csi-RS-ForTracking                          CSI-RS-ForTracking
                                OPTIONAL,
    aperiodicTRS                                ENUMERATED {supported}
                            OPTIONAL,
    ...
}
```

Message A.5: ServingCellConfig

```
ServingCellConfig ::=           SEQUENCE {
    tdd-UL-DL-ConfigurationDedicated    TDD-UL-DL-ConfigDedicated
        OPTIONAL,-- Cond TDD
    initialDownlinkBWP                  BWP-DownlinkDedicated
        OPTIONAL,   -- Cond ServCellAdd
    downlinkBWP-ToReleaseList           SEQUENCE (SIZE (1..
        maxNrofBWPs)) OF BWP-Id   OPTIONAL,
    downlinkBWP-ToAddModList        SEQUENCE (SIZE (1..maxNrofBWPs))
         OF BWP-Downlink OPTIONAL
    firstActiveDownlinkBWP-Id       BWP-Id      OPTIONAL,   -- Need
        R
    bwp-InactivityTimer             ENUMERATED {ms2, ms3, ms4, ms5, ms6,
         ms8, ms10, ms20,
                                                ms30, ms40,ms50, ms60,
                                                    ms80, ms100, ms200,
                                                ms300, ms500, ms750,
                                                    ms1280, ms1920,
                                                    ms2560,
                                                spare10, spare9, spare8,
                                                     spare7, spare6,
                                                spare5, spare4, spare3,
                                                    spare2, spare1 }
                                                OPTIONAL,
    defaultDownlinkBWP-Id           BWP-Id      OPTIONAL,   -- Need M
    uplinkConfig                    UplinkConfig    OPTIONAL, -- Cond
        ServCellAdd-UL
    supplementaryUplink             UplinkConfig    OPTIONAL, -- Cond
```

```
        ServCellAdd-SUL
    pdsch-ServingCellConfig      SetupRelease { PDSCH-
        ServingCellConfig } OPTIONAL, -- Need M
    csi-MeasConfig               SetupRelease { CSI-MeasConfig }
        OPTIONAL,    -- Need M
    carrierSwitching             SetupRelease { SRS-CarrierSwitching}
        OPTIONAL,    -- Need M
    sCellDeactivationTimer       ENUMERATED {ms20, ms40, ms80, ms160,
        ms200, ms240, ms320,
                                        ms400, ms480, ms520,
                                            ms640, ms720, ms840,
                                        ms1280, spare2, spare1}
                                            OPTIONAL,-- Cond
    .....
    }
}
```

Message A.6: BWP-Downlink

```
BWP-Downlink ::=     SEQUENCE {
    bwp-Id               BWP-Id,
    bwp-Common           BWP-DownlinkCommon
    bwp-Dedicated        BWP-DownlinkDedicated
    ...
}
```

Message A.7: BWP

```
BWP ::=         SEQUENCE {
    locationAndBandwidth        INTEGER (0..37949),
    subcarrierSpacing           SubcarrierSpacing,
    cyclicPrefix                ENUMERATED { extended }
}
```

Table A.1: DCI format1_1

Field	bits	Specification
Carrier indicator	0,3	-
Identifier for DCI formats	1	Always 1, indicating DL DCI format
Bandwidth part indicator	0,1,2	-
Frequency domain resource assignment	Variable	Defined in [63] section 5.1.2.2
Time domain resource assignment	4	Defined in [63] section 5.1.2.1
VRB-to-PRB mapping	0,1	-
PRB bundling size indicator	0,1	-
Rate matching indicator	0,1,2	-
ZP CSI-RS Trigger	0,1,2	-
Modulation and coding scheme [TB1]	5	Defined in [63] tables 5.1.3.1-1 and 5.1.3.1-2
New data indicator [TB1]	1	-
Redundancy version [TB1]	2	-
Modulation and coding scheme [TB2]	5	Defined in [63] tables 5.1.3.1-1 and 5.1.3.1-2
New data indicator [TB2]	1	-
Redundancy version [TB2]	2	-
HARQ process number	4	-
HARQ process number	0,2,4	-
TPC command for scheduled PUCCH	2	-
PUCCH resource indicator	3	-
PDSCH-to-HARQ-feedback timing indicator	0,1,2,3	-
Antenna port(s) and number of layers	4,5,6	Determined by DMRS Configuration Specified in [62] tables 7.3.1.2.2-1 to 7.3.1.2.2-4
Transmission configuration indication	0,3	-
SRS request	2	-
CBG transmission information(CBGTI)	0,2,4,6,8	-
CBG flushing out information(CBGFI)	0,1	-
DMRS sequence initialization	1	-

References

[1] L. Fanari, E. Iradier, I. Bilbao, R. Cabrera, J. Montalban, P. Angueira, O. Seijo, and I. Val, "A Survey on FEC Techniques for Industrial Wireless Communications," *IEEE Open Journal of the Industrial Electronics Society*, vol. 3, pp. 674–699, 2022.

[2] A. Ahmadi, M. Moradi, C. Cherifi, V. Cheutet, and Y. Ouzrout, "Wireless Connectivity of CPS for Smart Manufacturing: A Survey," in *2018 12th International Conference on Software, Knowledge, Information Management and Applications (SKIMA)*, 2018, pp. 1–8.

[3] P. Angueira, I. Val, J. Montalbán, Ó. Seijo, E. Iradier, P. S. Fontaneda, L. Fanari, and A. Arriola, "A Survey of Physical Layer Techniques for Secure Wireless Communications in Industry," *IEEE Communications Surveys and Tutorials*, vol. 24, no. 2, pp. 810–838, 2022.

[4] J. Mietzner, R. Schober, L. Lampe, W. H. Gerstacker, and P. A. Hoeher, "Multiple-antenna techniques for wireless communications - a comprehensive literature survey," *IEEE Communications Surveys and Tutorials*, vol. 11, no. 2, pp. 87–105, 2009.

[5] S. Kutty and D. Sen, "Beamforming for Millimeter Wave Communications: An Inclusive Survey," *IEEE Communications Surveys and Tutorials*, vol. 18, no. 2, pp. 949–973, 2016.

[6] I. Ahmed, H. Khammari, A. Shahid, A. Musa, K. S. Kim, E. De Poorter, and I. Moerman, "A Survey on Hybrid Beamforming Techniques in 5G: Architecture and System Model Perspectives," *IEEE Communications Surveys and Tutorials*, vol. 20, no. 4, pp. 3060–3097, 2018.

[7] K. Roth, H. Pirzadeh, A. L. Swindlehurst, and J. A. Nossek, "A Comparison of Hybrid Beamforming and Digital Beamforming With Low-Resolution ADCs for Multiple Users and Imperfect CSI," *IEEE Journal of Selected Topics in Signal Processing*, vol. 12, no. 3, pp. 484–498, 2018.

[8] Q. Spencer, B. Jeffs, M. Jensen, and A. Swindlehurst, "Modeling the statistical time and angle of arrival characteristics of an indoor multipath channel," *IEEE Journal on Selected Areas in Communications*, vol. 18, no. 3, pp. 347–360, 2000.

[9] D. Chizhik, J. Du, R. A. Valenzuela, D. Samardzija, S. Kucera, D. Kozlov, R. Fuchs, J. Otterbach, J. Koppenborg, P. Baracca, M. Doll, I. Rodriguez, R. Feick, and M. Rodriguez, "Directional Measurements and Propagation Models at 28 GHz for Reliable Factory Coverage," *IEEE Transactions on Antennas and Propagation*, vol. 70, no. 10, pp. 9596–9606, 2022.

[10] D. Chizhik, J. Du, R. A. Valenzuela, J. Otterbach, R. Fuchs, and J. Koppenborg, "Path Loss and Directional Gain Measurements at 28 GHz for Factory Automation," in *2019 IEEE International Symposium on Antennas and Propagation and USNC-URSI Radio Science Meeting*, 2019, pp. 2143–2144.

[11] D. Solomitckii, M. Allén, D. Yolchyan, H. Hovsepyan, M. Valkama, and Y. Koucheryavy, "Millimeter-Wave Channel Measurements at 28 GHz in Digital Fabrication Facilities," in *2019 16th International Symposium on Wireless Communication Systems (ISWCS)*, 2019, pp. 548–552.

[12] M. Jankiraman, *FMCW Radar Design*. Artech House, 2018.

[13] V. Giannini, D. Guermandi, Q. Shi, A. Medra, W. Van Thillo, A. Bourdoux, and P. Wambacq, "A 79 GHz phase-modulated 4 GHz-BW CW radar transmitter in 28 nm CMOS," *IEEE Journal of Solid-State Circuits*, vol. 49, no. 12, pp. 2925–2937, 2014.

[14] D. Guermandi, Q. Shi, A. Dewilde, V. Derudder, U. Ahmad, A. Spagnolo, I. Ocket, A. Bourdoux, P. Wambacq, J. Craninckx *et al.*, "A 79-GHz 2×2 MIMO PMCW radar SoC in 28-nm CMOS," *IEEE Journal of Solid-State Circuits*, vol. 52, no. 10, pp. 2613–2626, 2017.

[15] S. H. Dokhanchi, M. B. Shankar, Y. A. Nijsure, T. Stifter, S. Sedighi, and B. Ottersten, "Joint automotive radar-communications waveform design," in *2017 IEEE 28th Annual International Symposium on Personal, Indoor, and Mobile Radio Communications (PIMRC)*. IEEE, 2017, pp. 1–7.

[16] Y. Zhang, Q. Li, L. Huang, K. Dai, and J. Song, "Waveform design for joint radar-communication with nonideal power amplifier and outband interference," in *2017*

IEEE wireless communications and networking conference (WCNC). IEEE, 2017, pp. 1–6.

[17] M. Bocquet, C. Loyez, C. Lethien, N. Deparis, M. Heddebaut, A. Rivenq, and N. Rolland, "A multifunctional 60-GHz system for automotive applications with communication and positioning abilities based on time reversal," in *The 7th European Radar Conference*. IEEE, 2010, pp. 61–64.

[18] C. Sturm and W. Wiesbeck, "Waveform design and signal processing aspects for fusion of wireless communications and radar sensing," *Proceedings of the IEEE*, vol. 99, no. 7, pp. 1236–1259, 2011.

[19] C. R. Berger, B. Demissie, J. Heckenbach, P. Willett, and S. Zhou, "Signal processing for passive radar using OFDM waveforms," *IEEE Journal of Selected Topics in Signal Processing*, vol. 4, no. 1, pp. 226–238, 2010.

[20] L. Reichardt, C. Sturm, F. Grünhaupt, and T. Zwick, "Demonstrating the use of the IEEE 802.11 p car-to-car communication standard for automotive radar," in *2012 6th European Conference on Antennas and Propagation (EUCAP)*. IEEE, 2012, pp. 1576–1580.

[21] S. H. Dokhanchi, B. S. Mysore, K. V. Mishra, and B. Ottersten, "A mmWave automotive joint radar-communications system," *IEEE Transactions on Aerospace and Electronic Systems*, vol. 55, no. 3, pp. 1241–1260, 2019.

[22] B. Donnet and I. Longstaff, "Combining MIMO radar with OFDM communications," in *2006 European radar conference*. IEEE, 2006, pp. 37–40.

[23] D. Garmatyuk, J. Schuerger, K. Kauffman, and S. Spalding, "Wideband OFDM system for radar and communications," in *2009 IEEE radar conference*. IEEE, 2009, pp. 1–6.

[24] S. H. Dokhanchi, M. B. Shankar, T. Stifter, and B. Ottersten, "OFDM-based automotive joint radar-communication system," in *2018 IEEE Radar Conference (RadarConf18)*. IEEE, 2018, pp. 0902–0907.

[25] Y. Liu, G. Liao, J. Xu, Z. Yang, and Y. Zhang, "Adaptive OFDM integrated radar and communications waveform design based on information theory," *IEEE Communications Letters*, vol. 21, no. 10, pp. 2174–2177, 2017.

[26] P. Kumari, S. A. Vorobyov, and R. W. Heath, "Adaptive virtual waveform design for millimeter-wave joint communication-radar," *IEEE Transactions on Signal Processing*, vol. 68, pp. 715–730, 2019.

[27] A. Bedin, D. Chizhik, J. Du, M. Moisio, K. Upadhya, R. Valenzuela, and M. A. Uusitalo, "28 GHz NLOS Channel Measurements Revealing Low Path Loss and High Angular Spread in Container Ports," 2023, submitted to IEEE Transactions on Antennas and Propagation. Available at https://arxiv.org/abs/2309.02810.

[28] A. Bedin, D. Korpi, K. Upadhya, and M. A. Uusitalo, "Receiver apparatus and transmitter apparatus, ep4175191a1," European Patent EP4 175 191A1.

[29] A. Bedin, A. Jain, A. Zanella, and K. Upadhya, "Heterogeneous rank beamforming for industrial communications," 2023, submitted to IEEE Transactions on Communications. Available at https://arxiv.org/abs/2309.12636.

[30] A. Jain and A. Bedin, "Beamforming configuration," Finnish Patent PCT/FI2023/050 514.

[31] A. Bedin and A. Zanella, "Geometry and Wideband Performance of a Maximal Ratio Combining Beam," 2023, submitted to IEEE Wireless Communications and Networking Conference 2024. Available at https://arxiv.org/abs/2309.02824.

[32] A. Bedin, S. Shahcheraghi, T. E. Abrudan, and A. Asadi, "Low-complexity hardware and algorithm for joint communication and sensing," 2023, available at https://arxiv.org/abs/2309.06850.

[33] Hexa-X, "Gap analysis and technical work plan for specialpurpose functionality," June 2021. [Online]. Available: https://hexa-x.eu/wp-content/uploads/2021/06/Hexa-X_D7.1.pdf

[34] ——, "Localisation and sensing use cases and gap analysis," December 2021. [Online]. Available: https://hexa-x.eu/wp-content/uploads/2022/02/Hexa-X_D3.1_v1.4.pdf

[35] D. Chizhik, J. Du, R. Feick, M. Rodriguez, G. Castro, and R. A. Valenzuela, "Path Loss and Directional Gain Measurements at 28 GHz for Non-Line-of-Sight Coverage of Indoors With Corridors," *IEEE Transactions on Antennas and Propagation*, vol. 68, no. 6, pp. 4820–4830, 2020.

[36] R. Kovalchukov, D. Moltchanov, Y. Gaidamaka, and E. Bobrikova, "An Accurate Approximation of Resource Request Distributions in Millimeter Wave 3GPP New Radio Systems," 08 2019.

[37] Y. Wang, Z. Wei, and Z. Feng, "Beam training and tracking in mmwave communication: A survey," 2022.

[38] Mini-Circuits, "MMIC Surface mount wideband doubled balanced mixer MDB-54H+ datasheet," Tech. Rep. [Online]. Available: https://www.minicircuits.com/pdfs/MDB-54H+.pdf

[39] T. Instruments, "Single Channel 12-Bit 500Msps Analog to Digital Converter ADS5403 datasheet." [Online]. Available: https://www.ti.com/lit/ds/symlink/ads5403.pdf

[40] Mini-Circuits, "Monolithic Amplifier PMA3-313GLN+." [Online]. Available: https://www.minicircuits.com/pdfs/PMA3-313GLN+.pdf

[41] A. Devices, "ADF4371 Microwave Wideband Synthesizer with Integrated VCO." [Online]. Available: https://www.analog.com/media/en/technical-documentation/data-sheets/adf4371.pdf

[42] L. Kahn, "Ratio Squarer," *Proceedings of the IRE*, vol. 42, no. 11, p. 1704, 1954.

[43] A. Goldsmith, *Wireless Communications*. Cambridge University Press, 2005.

[44] G. Karagiannidis, D. Zogas, N. Sagias, S. Kotsopoulos, and G. Tombras, "Equal-gain and maximal-ratio combining over nonidentical Weibull fading channels," *IEEE Transactions on Wireless Communications*, vol. 4, no. 3, pp. 841–846, 2005.

[45] R. Annavajjala, "A simple approach to error probability with binary signaling over generalized fading channels with maximal ratio combining and noisy channel estimates," *IEEE Transactions on Wireless Communications*, vol. 4, no. 2, pp. 380–383, 2005.

[46] Y. G. Kim and N. C. Beaulieu, "New results on maximal ratio combining in Nakagami-m fading channels," in *2012 IEEE International Conference on Communications (ICC)*, 2012, pp. 4761–4765.

[47] F. du Pin Calmon and M. D. Yacoub, "MRCS - selecting maximal ratio combined signals: a practical hybrid diversity combining scheme," *IEEE Transactions on Wireless Communications*, vol. 8, no. 7, pp. 3425–3429, 2009.

[48] Y. A. Chau and K. Y. Huang, "Spatial diversity with a new sequential maximal ratio combining over wireless fading channels," in *2011 IEEE 12th International Workshop on Signal Processing Advances in Wireless Communications*, 2011, pp. 241–245.

[49] 3GPP, "Radio Resource Control (RRC); Protocol specification," 3rd Generation Partnership Project (3GPP), Technical Specification (TS) 38.331, 03 2023, version 17.4.0. [Online]. Available: https://portal.3gpp.org/desktopmodules/Specifications/SpecificationDetails.aspx?specificationId=3197

[50] ——, "Physical channels and modulation," 3rd Generation Partnership Project (3GPP), Technical Specification (TS) 38.211, 03 2023, version 17.4.0. [Online]. Available: https://portal.3gpp.org/desktopmodules/Specifications/SpecificationDetails.aspx?specificationId=3213

[51] J. Zheng, Q. Zhang, and J. Qin, "Average Achievable Rate and Average BLER Analyses for MIMO Short-Packet Communication Systems," *IEEE Transactions on Vehicular Technology*, vol. 70, no. 11, pp. 12 238–12 242, 2021.

[52] J. Xue, T. Ratnarajah, C. Zhong, and C.-K. Wen, "Reliability Analysis for Large MIMO Systems," *IEEE Wireless Communications Letters*, vol. 3, no. 6, pp. 553–556, 2014.

[53] M. Zwingelstein-Colin and M. Debbah, "Physical layer reliability vs ARQ in MIMO block-fading channels," in *2012 IEEE Wireless Communications and Networking Conference (WCNC)*, 2012, pp. 1670–1674.

[54] B. A. Johnson, Y. I. Abramovich, and X. Mestre, "MUSIC, G-MUSIC, and Maximum-Likelihood Performance Breakdown," *IEEE Transactions on Signal Processing*, vol. 56, no. 8, pp. 3944–3958, 2008.

[55] M. Kotaru, K. Joshi, D. Bharadia, and S. Katti, "Spotfi: Decimeter level localization using wifi," *SIGCOMM Comput. Commun. Rev.*, vol. 45, no. 4, p. 269–282, aug 2015. [Online]. Available: https://doi.org/10.1145/2829988.2787487

[56] R. Schmidt, "Multiple emitter location and signal parameter estimation," *IEEE Transactions on Antennas and Propagation*, vol. 34, no. 3, pp. 276–280, 1986.

[57] N. Dharamdial, R. S. Adve, and R. M. Farha, "Multipath delay estimations using matrix pencil," *2003 IEEE Wireless Communications and Networking, 2003. WCNC 2003.*, vol. 1, pp. 632–635 vol.1, 2003.

[58] Y. Hua and T. Sarkar, "Matrix pencil method for estimating parameters of exponentially damped/undamped sinusoids in noise," *IEEE Transactions on Acoustics, Speech, and Signal Processing*, vol. 38, no. 5, pp. 814–824, 1990.

[59] L. Song, R. Adve, and D. Hatzinakos, "Matrix Pencil for Positioning in Wireless ad hoc Sensor Network," vol. 2920, 01 2004, pp. 18–27.

[60] A. Ali and A. Omar, "Time of Arrival estimation for WLAN indoor positioning systems using Matrix Pencil Super Resolution Algorithm," *Proceedings of the 2nd Workshop on Positioning, Navigation and Communication, WPNC*, vol. 5, 01 2005.

[61] 3GPP, "User Equipment (UE) radio access capabilities," 3rd Generation Partnership Project (3GPP), Technical Specification (TS) 38.306, 03 2023, version 17.4.0. [Online]. Available: https://portal.3gpp.org/desktopmodules/Specifications/SpecificationDetails.aspx?specificationId=3193

[62] ——, "Multiplexing and channel coding," 3rd Generation Partnership Project (3GPP), Technical Specification (TS) 38.212, 03 2023, version 17.5.0. [Online]. Available: https://portal.3gpp.org/desktopmodules/Specifications/SpecificationDetails.aspx?specificationId=3214

[63] ——, "Physical layer procedures for data," 3rd Generation Partnership Project (3GPP), Technical Specification (TS) 38.214, 03 2023, version 17.5.0. [Online]. Available: https://portal.3gpp.org/desktopmodules/Specifications/SpecificationDetails.aspx?specificationId=3216

[64] Sharetechnote, Accessed on June 2023. [Online]. Available: https://www.sharetechnote.com/html/5G/5G_RRC_Overview.html

[65] ——, Accessed on June 2023. [Online]. Available: https://www.sharetechnote.com/html/5G/5G_DCI.html

Publications

Some of the results here presented were collected in technical papers and patents. At this time, the following have been published or submitted:

Journals

[27] A. Bedin, D. Chizhik, J. Du, M. Moisio, K. Upadhya, R. Valenzuela, and M. A. Uusitalo, "28 GHz NLOS Channel Measurements Revealing Low Path Loss and High Angular Spread in Container Ports," 2023, submitted to IEEE Transactions on Antennas and Propagation. Available at https://arxiv.org/abs/2309.02810

[29] A. Bedin, A. Jain, A. Zanella, and K. Upadhya, "Heterogeneous rank beamforming for industrial communications," 2023, submitted to IEEE Transactions on Communications. Available at https://arxiv.org/abs/2309.12636

[32] A. Bedin, S. Shahcheraghi, T. E. Abrudan, and A. Asadi, "Low-complexity hardware and algorithm for joint communication and sensing," 2023, available at https://arxiv.org/abs/2309.06850

Conferences

[31] A. Bedin and A. Zanella, "Geometry and Wideband Performance of a Maximal Ratio Combining Beam," 2023, submitted to IEEE Wireless Communications and Networking Conference 2024. Available at https://arxiv.org/abs/2309.02824

Patent applications

[28] A. Bedin, D. Korpi, K. Upadhya, and M. A. Uusitalo, "Receiver apparatus and transmitter apparatus, ep4175191a1," European Patent EP4 175 191A1

[30] A. Jain and A. Bedin, "Beamforming configuration," Finnish Patent PCT/FI2023/050 514

Acknowledgments

This project has received funding from the European Union's Horizon 2020 research and innovation program under the Marie Skłodowska-Curie Grant agreement No. 861222 (MINTS). I would like to thank the team of the Nokia Bell Labs Radio System Research lab in Espoo Finland for the significant contributions to this work and to my PhD experience. Particular contributions to this thesis has been brought by (in alphabetical order) Akshay Jain, Karthik Upadhya, Martti Moisio, Mikko Uusitalo and Traian E. Abrudan From the Bell Labs Espoo Team, as well as Dmitry Chizhik, Jinfeng Du and Reinaldo Valenzuela from Bell Labs US in Murray Hill. I would also like to Thank prof. Arash Asadi and Shaghaeygh Shahcheraghi from TU Darmstadt, for hosting my secondment and cooperating in the development of the sensing algorithm.